Direct and Large-Eddy Simulation of the Spatial Turbulent Mixing Layer

Irene de Bruin

2001

Ph.D. thesis
University of Twente

Twente University **Press**

Direct and Large-Eddy Simulation of the Spatial Turbulent Mixing Layer

Cover picture: spanwise vorticity for isovalues *-0.1* (blue) and *0.1* (red)
at *Re* = 2000 (see Chapter 6)

Twente University **Press**

DIRECT AND LARGE-EDDY SIMULATION
OF THE
SPATIAL TURBULENT MIXING LAYER

PROEFSCHRIFT

ter verkrijging van
de graad van doctor aan de Universiteit Twente,
op gezag van de rector magnificus,
prof.dr. F.A. van Vught,
volgens besluit van het College voor Promoties
in het openbaar te verdedigen
op vrijdag 14 september 2001 te 13.15 uur

door

Irene Caroline Carmen de Bruin

geboren op 3 april 1972
te Hengelo

Dit proefschrift is goedgekeurd door de promotor

Prof.dr.ir. P.J. Zandbergen

en de assistent-promotor

Dr. J.G.M. Kuerten

to Peter

Preface

Completing this work would not have been possible without the support of and inspiration from a large number of people. First of all I would like to thank professor Zandbergen for enabling me to carry out this research. I admire the vigorous way you got the project officially going. Furthermore, I appreciated your encouragements during the project. Bernard Geurts and Hans Kuerten took care of the daily supervision. Hans, your cheerful attitude and patience have been very valuable to me and happily this did not change when you moved to Eindhoven. Bernard, I will for long remember our lively conversations on both technical issues and subjects far from that. Sometimes even confronting, but always with a relativity and modesty towards our daily work and world. The two of you managed to create a pleasant and inspiring atmosphere in the group. I very much enjoyed the mixture of personalities that crowded together at the square outside my room at specific times. Even when the research was not going as I wished, this 'coffee group' made me always entering the office with a positive feeling. I also appreciated very much that so many of the applied analysis group attended my examination concerts at the conservatory of music.

Furthermore, I would like to thank Bono Wasistho for going through the computer code together. Also Bert Vreman was very helpful by giving instantaneous support either by phone or in person. Your advise and experience in 'our' mixing layer were very valuable. Also Jaap van der Vegt inspired me with stimulating discussions. Several (foreign) guests visited the group and enlarged my enthousiasm for (turbulence) research. In particular I would like to thank Neil Sandham for sharing some of his profound, overall knowledge of the mixing layer with me.

A major part of my research involved the numerical simulation on supercomputers. I would like to express my gratitude to the people at SARA in Amsterdam, some of which I only know by voice. They were always very helpful in dealing with complicated situations or requests. Also the people from computer support in Twente were always very willing regarding the postprocessing of large data files and other matters of crucial importance. The matlab script written by Wilbert IJzerman was very useful to transport data

files between different computers. Furthermore, I would like to thank Piet Moeleker for his help from overseas with Tecplot. In the final phase of writing this thesis, Timco Visser has been very helpful with his knowledge of LaTeX and file conversion. Also, I would like to thank my roommates Paulien, Ljuba, Andonowati and Yvonne for our cosy and sometimes more serious conversations.

Finally, I would like to mention my mum and dad who always supported and encouraged me in everything I did. I thank both of you and Marleen for the relaxing moments we spend together and for being there when needed. Last but not least, a lot of understanding and sweet words have been coming from Peter. Without you, life would have been very boring.

Irene de Bruin   *Enschede, June 2001*

Contents

Chapter 1

Introduction

Fluid flow is present everywhere around and inside us. We can think of the blood running through our vessels and the air flowing into our lungs. Fluid also flows around the vehicles we use. In combustion chambers of their engines, fuel is mixed with an oxidizer [63]. Fluid flow also exists at much larger dimensions, for example the flow of air in our atmosphere, *i.e.*, the weather. As a final example, we show the flow of water in the Dutch Deltaworks in Figure 1.1. This photo displays the wakes that emerge downstream of the piers.
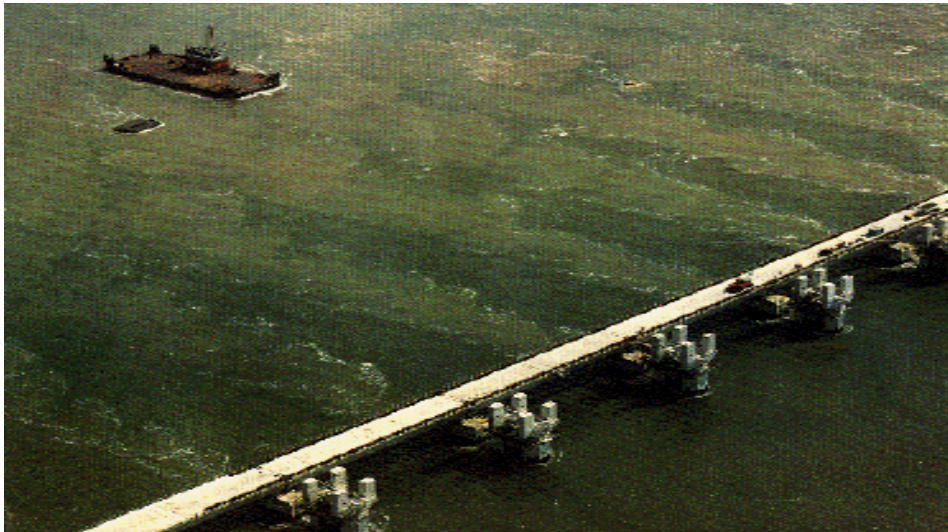

Figure 1.1: This dam is part of the defenses against the sea erected in the Netherlands; province of Zeeland [84]. The wakes behind the piers are clearly visible. The water flows from the lower right side to the upper left side.

A detailed knowledge of the flow characteristics is of crucial importance in order to understand all these systems and subsequently, *e.g.*, optimize some of their specific properties. A better understanding can for example reduce the aerodynamic drag of an airplane or improve the efficiency of an engine. Even a small improvement may save enormous amounts of fuel. Another example is the suit employed by some professional swimmers. Its surface has a carefully designed roughness pattern and some people think this improves the efficiency of moving through the water. However, the understanding and prediction of flow phenomena is often complicated because turbulence plays a key role in many of these flows. Turbulence involves the presence of many interacting flow features which occur at a variety of lengthscales. The research is complicated by the presence of a large range of scales that all should be taken into account. This is poetically paraphrased in the following 'Sonnet to Turbulence', written by Corrsin (see ref. [35]):

Shall we compare you to a laminar flow?
You are more lovely and more sinuous.
Rough winter winds shake branches free of snow,
And summer's plumes churn up in cumulus.

How do we perceive you? Let me count the ways.
A random vortex field with strain entwined.
Fractal? Big and small swirls in the maze
May give us paradigms of flows to find.

Orthonormal forms nonlinearly renew
Intricate flows with many free degrees
Or, in the latest fashion, merely few –
As strange attractor. In fact, we need Cray 3's.

Experiment and theory, unforgiving;
For serious searcher, fun ... and it's a living!

Turbulence is present in almost all flows of practical engineering interest. Therefore it is useful to describe turbulence in a more quantitative way, but we first give examples in which a state of turbulent flow is readily attained. When we open a tap a little bit, we have laminar flow: water pours out in a smooth jet [63]. Fully opening the tap, however, results in a more vivid and sinuous pattern which is called turbulent flow. In spite of its bad reputation in daily life, only the specific application determines whether the presence of turbulence is beneficial or not. The occurrence of turbulence in flow around an airfoil should be minimized because it increases the drag of the airplane. In contrast, we take advantage of turbulence to reach an efficient mixing of two fluids. In that case the interface between two regions of unmixed fluids is increased rapidly as a result of the turbulent flow state. So, turbulence is not

always an unfortunate phenomenon that should be avoided.

A quantitative way to characterize the state of a fluid requires the dimensionless Reynolds number defined as:

$$Re = \frac{\rho_R \, u_R \, l_R}{\mu_R},\qquad(1.1)$$

with ρ_R, u_R, l_R and μ_R a reference density, velocity, length and viscosity, respectively [75]. It is a measure of the ratio between convective, *i.e.*, destabilizing, and viscous, *i.e.*, stabilizing forces. Flows in which the inertia forces are sufficiently small compared to viscous forces are laminar flows. The small flow features are dissipated by the viscous forces. Flows with relatively large Reynolds numbers are generally turbulent. They exhibit a large range of length and time scales. In fact, turbulence frequently develops as an instability of laminar flow [107].

Turbulence involves the presence of many different scales in the flow. One of the first theories of turbulence was proposed by Kolmogorov who introduced the idea of the energy-cascade [49]. This theory states that energy which is injected into the large scales of a system statistically is transported to smaller and smaller scales and finally dissipates at sufficiently small scales. Another characteristic feature of turbulence is the fact that the exact state of a turbulent flow is unpredictable. Small destabilizing perturbations, which are always present, can soon become larger because of the strong nonlinear behaviour of the system at high Reynolds number. Small scales influence the large-scale and long-term behaviour of the flow. Hence, the small scales should be taken into account when the large scale behaviour of the system is described. Because of the highly unstable character of turbulence, typical flow quantities usually are considered and compared only in a statistical sense. We are interested to know, *e.g.*, the chance to have rainshowers. However, the exact times and locations where it will rain is not relevant at this stage.

Physical experiments and numerical simulations are two main directions of research of fluid flow. Physical experiments have a long history in research. In the past decades, numerical simulation has become another way to tackle fluid flow problems. Computational fluid dynamics (CFD) and wind-tunnels are both used, *e.g.*, for aircraft development in which turbulence is one of the main issues [63]. Especially in the early design stages of wind-tunnel testing, several key dimensions and other basic parameters of the aircraft are not yet established. This pioneering research can now be supported by numerical simulations. Another advantage of using simulations is that one has an exact knowledge of boundary conditions. Besides, all properties can be computed throughout the whole domain and the resulting databases permit access to quantities, such as pressure fluctuations, which are difficult to measure. However, even today the limits of the most powerful supercomputers make wind-

tunnel experiments necessary to verify the design of a new airplane at several stages in the development process [63, 92].

In this thesis we focus on numerical simulations. The numerical simulation of turbulence is based on the Navier-Stokes equations. These represent the conservation of mass, momentum and energy. In the last decades, supercomputers have become large and powerful enough to tackle these equations for a number of flows. The simulations that can be performed become larger and more complex. Important techniques used in the numerical simulation of turbulence are direct and large-eddy simulations (abbreviated as DNS and LES respectively). The main purpose of this thesis is to perform DNSs of the three-dimensional subsonic mixing layer and to subsequently use these results to test, *e.g.*, features of Reynolds-averaged Navier-Stokes (RaNS) and subgrid-models in LES. The first section of this chapter is used to introduce the mixing layer. Typical physical processes that take place are described. An introduction to the numerical simulation of turbulence and in particular the turbulent mixing layer is given in section two. Finally we formulate our aims in more detail in the third section.

1.1   The mixing layer

Turbulent shear flows are characterized by the presence of a shear stress. Three important examples of turbulent shear flows are the jet, wake and mixing layer. We start with the jet which arises, *e.g.*, in the flow of water when a tap is opened and a liquid is injected into the air. A second type of turbulent shear flow is the wake. It is a flow which emerges downstream of an object. Several wakes parallel to each other were already shown in Figure 1.1. The outer velocities in a wake are equal to each other. This is no longer the case for the mixing layer that forms when two streams of different velocity meet, for example when two, initially separated, rivers flow together at different velocities and start to mix. Mixing layers also occur in many other practical applications, *e.g.*, combustion devices where oxygen and fuel are mixed [63]. Enhancement of the mixing of two fluids can be very beneficial in these applications. It may, for example, result in a cleaner, more efficient combustion.

Before we focus on the mixing layer in particular, we first investigate the presence of self-similarity. In turbulent shear flows, it is assumed that sufficiently far from inflow boundaries, and for times long after the initial conditions were established, the statistics of the flow can be characterized by the steady flow features at one downstream location [7]. These so-called self-similar quantities can be described quite accurately with only one profile and the evolution of a similarity variable in the self-similar turbulent region. This implies a considerable collapse of the data. For the DNS results presented in

this thesis, we study time-averaged quantities to numerically establish, *e.g.*, the presence of self-similarity in a mixing layer. Self-similarity is a physical property that is typical for all turbulent shear flows. We next focus on the mixing layer in particular. We start with an extensive description of the mixing layer. A dimensionless number which mainly accounts for the amount of compressibility is introduced. Finally we mention some features that are based on empirical knowledge from experiments and simulations.

Because of the difference in velocity of the two merging streams in a mixing layer, a large shear is present which results in vortices that roll-up and merge while moving downstream. During the pairing process large strain rates occur and the interface between the two streams increases. A greater interfacial area provides a more efficient mixing. An instability that results in a turbulent mixing layer is illustrated with an atmospheric example. Figure 1.2 displays a mixing layer in a cloud formation. A shear layer forms between two parallel atmospheric streams that travel with different velocities. Small perturbations grow since the layer is unstable. This instability is a typical feature in the initial stages of mixing layers and is known as the Kelvin-Helmholtz instability [8].

It is important that the present results can be compared with those from other experimental and numerical mixing layer studies. In order to have an equal setting, next to the Reynolds number mentioned above, also the amount of compressibility should be equal. In the past decades, compressibility has been subject of many experimental mixing layer studies [18, 68, 71]. A new dimensionless number became a popular quantity to account for the com-

Figure 1.2: Kelvin-Helmholtz roll-ups as seen in a cloud formation [84].

pressibility of mixing layers. Next to the well-known Mach number, denoted by M_∞, the related convective Mach number M_c was introduced [14]. These two dimensionless numbers are defined as follows:

$$M_\infty = \frac{U_1}{c_1},$$
$$M_c = \frac{U_1 - U_2}{c_1 + c_2},$$

where $U_1(U_2)$ is the velocity of the upper (lower) free-stream and $c_1(c_2)$ the corresponding speed of sound. In this definition, the ratio between specific heats $(\gamma = C_P/C_V)$ of both streams is assumed equal. The normalized growth rates in first order collapse onto a single curve when plotted against the convective Mach number [53].

In the nineties, compressibility effects of the mixing layer could also be considered in numerical studies. This was done for the temporal setting in refs. [79, 103]. Throughout this thesis the dimensionless lower stream velocity U_2 is set to 0.5 U_1. The Mach number is set to 0.8, which corresponds to a convective Mach number of 0.2. The effect of compressibility is negligible at these parameter values [97]. This convective Mach number is equal to that from the temporal study in [104] where direct and large-eddy simulations are performed. As a result, it seems reasonable to compare the present spatial mixing layer results with temporal mixing layer results at the same convective Mach number as well as results from incompressible mixing layer experiments.

A characteristic property of the mixing layer is that the most unstable mode for the present convective Mach number is expected to be two-dimensional. This does not imply that the whole transition process is two-dimensional [78]. The most amplified instability wave from linear stability theory (LST) is two-dimensional for the present case. Further downstream, where LST does not apply anymore, also three-dimensional features evolve, triggered by small three-dimensional inflow perturbations.

The convective Mach number has been used to quantify the effects of compressibility in mixing layers [14, 68]. One of the first studies on density effects in mixing layers was the experiment performed by Brown and Roshko [18]. Also the presence of large structures was studied. So-called spark shadow pictures showed that, for all ratios of densities in the two streams, the mixing layer is dominated by large coherent structures. This is clearly illustrated in Figure 1.3. The sequence of similar structures becoming larger further downstream, clearly illustrates the growth of the mixing layer. Next to the presence of large structures, a typical mixing layer phenomenon is the growth rate reduction when the convective Mach number increases [18, 78, 103]. As a result, the growth rate is coupled with only the velocity and density ratios (as long as the pressure and specific heat ratios equal one).
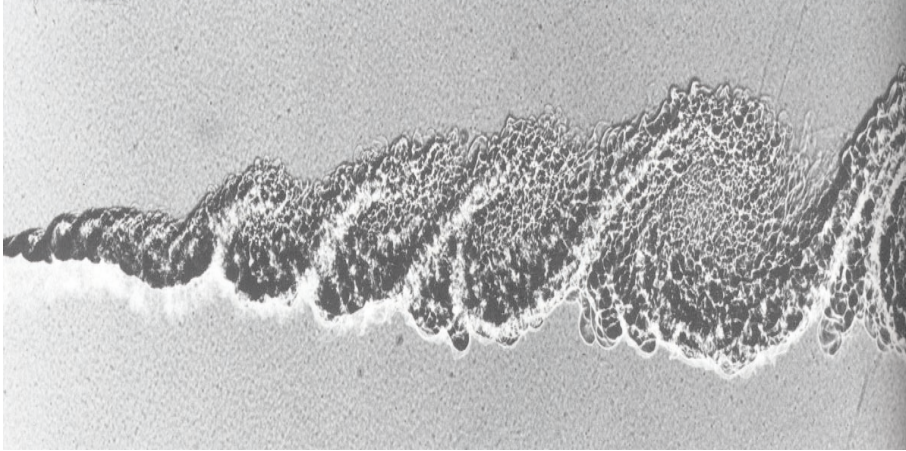
Figure 1.3: Spark shadow photograph of a mixing layer from the experiments performed by Brown and Roshko [96]. The upper flow of nitrogen mixes at 1000 cm/s with the lower flow (same density) of a helium argon mixture that flows at 380 cm/s.

Finally we mention the asymmetric entrainment of the mixing layer. As a result, the point where the averaged streamwise velocity equals the convective velocity deflects into the low-speed stream. This is observed in experiments [28, 67] and numerical simulations [78] and was also found in the present simulations. In this section we have mentioned several aspects that generally are considered as typical features of the mixing layer. Next we continue with a description of the numerical simulation of the mixing layer.

1.2   Numerical simulation of the turbulent mixing layer

The traditional approach to the Navier-Stokes equations was to reduce them to the so-called Reynolds-averaged Navier-Stokes (RaNS) equations. In this strategy only averaged quantities which describe the mean flow are solved. The averaging of nonlinear terms introduces new unknowns in the equations for which a turbulence model is adopted. Another technique in the simulation of turbulence is direct numerical simulation (DNS) which became popular in the eighties. The full, time-dependent Navier-Stokes equations are solved numerically, essentially without any approximations other than numerical.

It was realized early on that DNS is too expensive to be used in most cases of industrial interest because of the relatively high Reynolds numbers and

complex flows. On the other hand, the models used in RaNS are too dependent on the characteristics of particular flows and hence RaNS cannot be used as a method of general applicability. Therefore an intermediate approximation was developed: large-eddy simulation (LES). Here, the large scales of the flow are computed explicitly, similarly as in DNS, while the effect of the small scales on the large scales is modeled.

Simple flows, *i.e.*, flows with a relatively low Reynolds number and a relatively simple and small flow domain, can be simulated by a DNS. For more complicated flows, LES (or RaNS) should be used. The data obtained from a DNS of a simple flow can be used to validate the LES subgrid (or RaNS) model. In principle, the most appropriate model can be selected in this way. The 'best' model can subsequently be incorporated into LES (or RaNS) of a more complicated flow for which DNS is no longer feasible.

Previously, the temporal mixing layer has been investigated with DNS and the results were used, *e.g.*, for the assessment of the quality of subgrid-models in LES [104]. The issue of self-similarity in numerical studies of the mixing layer has mainly been studied in the temporal setting [3, 77, 104, 110]. However, the temporal simulation is only a crude approximation of physical reality since periodic conditions are applied in the streamwise direction. Therefore, we extend this approach to enable spatial simulations by including suitable inflow and outflow boundaries. This allows direct comparison with results of physical experiments.

The difference between the temporal and spatial setting is illustrated in Figure 1.4 where mixing layer results are shown for both frameworks. In the temporal domain a computational box is considered which is relatively small in the streamwise direction and has periodic boundary conditions. It is an approximation of the situation that would arise when moving along with the centerplane velocity over the spatial mixing layer in downstream direction. As a result, the thickness of the mixing layer grows in time in the temporal framework whereas it grows in the streamwise direction in the spatial framework. In the temporal setting the Mach number M_∞ and the convective Mach number M_c, as introduced in the previous section, are equal. This is no longer the case for the spatial framework in which M_c usually is considered as the relevant dimensionless number [14, 68]. It is based on the velocity difference between the two free-streams of the merging layers, *i.e.*, the mixing layer as seen from the convective frame.

In this thesis, we focus on DNS and LES of a three-dimensional subsonic mixing layer. The extensive database from the DNS is also used for RaNS modeling purposes. We focus on the eddy viscosity and gradient-diffusion hypotheses. We stress that the comparison with RaNS is done in an *a priori* sense. It only involves a post-processing of the DNS data and no actual RaNS simulation is performed. On the contrary, the LES results are only used for
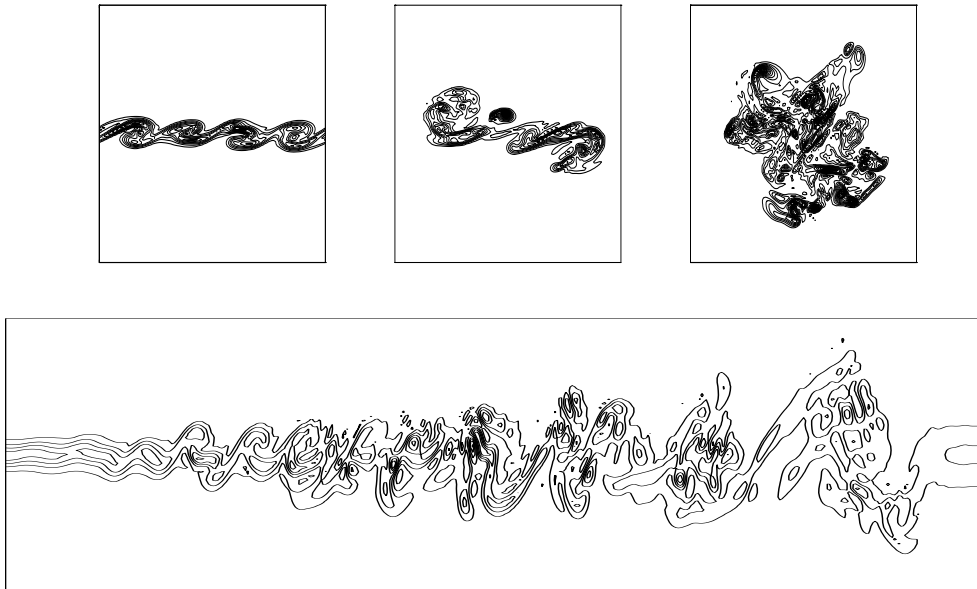
Figure 1.4: Contours of spanwise vorticity for a temporal mixing layer at three subsequent times (upper figures, courtesy of Bert Vreman [104]) and a spatial mixing layer (lower figure, present results). All plots are at characteristic spanwise locations with horizontal streamwise domain and vertical normal domain.

a posteriori testing. In this type of comparison, actual LES simulations are compared with filtered DNS data.

In the present study we thoroughly investigate the minimal set of items that is necessary to come to a numerical spatial simulation that displays several properties that are typical for a realistic mixing layer. These, among others, involve a transition to turbulence by means of vorticity rollers that pair. We also investigate the presence of self-similarity in the turbulent regime. Furthermore we consider the specific values for the growth rate of the mixing layer thickness and the peak values for the components of the Reynolds stress tensor.

Next we give a more detailed description of the present configuration. We consider subsonic, spatially developing mixing layers that reach a transitional state which is followed by turbulent flow. For many flows of theoretical interest, the domain is infinite in all directions. For practical reasons, it is necessary to artificially truncate the domain. The procedure of truncation should be performed in such a way that the solution inside the domain remains approximately unchanged. The spatially evolving mixing layer is studied in a computational domain which has the form of a rectangular box as shown
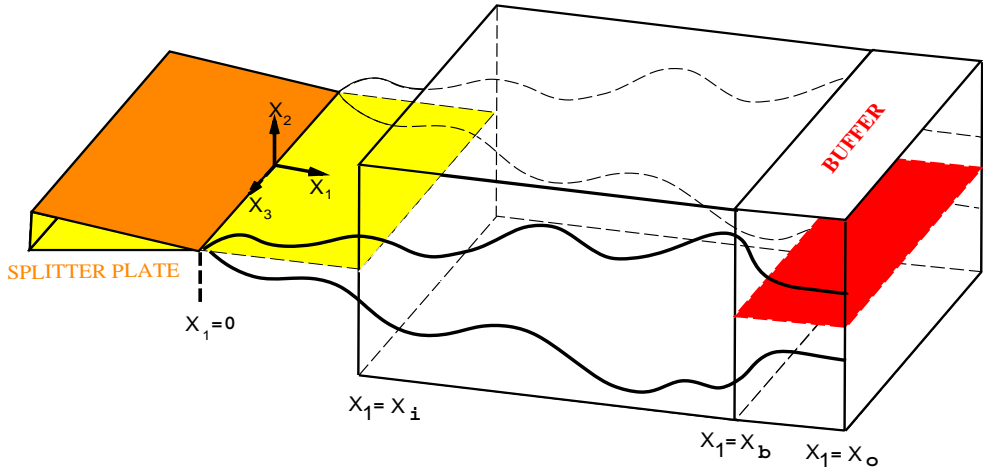
Figure 1.5: Specification of the computational domain, consisting of stream-wise (x_1), normal (x_2) and spanwise (x_3) direction. The streamwise domain is from x_i to x_o and the buffer starts at x_b.

in Figure 1.5. Periodic boundary conditions are used in the spanwise direction. Beyond the trailing edge of a splitter plate a mixing layer is formed. The inflow boundary of the computational domain is situated downstream of this trailing edge. When the mixing layer is described, globally three typical areas can be distinguished. The turbulence, that we are mainly interested in, arises around the centerline. The free-streams of the mixing layer refer to both outer sides of the normal domain which are characterized by steady flow. The areas in between these two are called the edges of the mixing layer.

During the simulations, the mixing layer is forced at the inflow boundary by imposing perturbations that travel downstream and grow. The laminar flow just behind the inflow boundary is followed by a transitional region containing typical structures such as lambda-vortices [21, 78]. These interact and develop further downstream into a turbulent state. At the outflow a buffer domain is introduced which is typically about 10% of the total domain and has the purpose of decreasing the perturbations to zero [105]. In order to be able to compare the spatial mixing layer DNS and LES with the temporal mixing layer study done in [104] we use the same grid distance and other relevant parameters.

The simulations suggested here can only be performed for a simple configuration. This implies that not only the computational domain but also the Reynolds number should be small enough. Another turbulent shear flow set-

ting that is minimal is the channel study described in ref. [45]. Despite its simplicity, this setting is useful since several typical flow features are retained. The study describes results of direct numerical simulations of unsteady channel flow at low to moderate Reynolds numbers. The objective is to identify the minimal dimensions of the computational problem required to sustain a turbulent boundary layer. This simplified situation cannot accurately predict some of the higher-order turbulence statistical quantities. The computations represent a basic building block from which a self-sustained turbulent flow can be constructed. Near the wall, the low-order statistics behaved in much the same manner as the experimental results. The minimal channel represents a system that exhibits many of the characteristics of near-wall turbulence in fully developed turbulent channels and it does so at strongly reduced computational cost.

Most of the simulations in the present study are performed for simple configurations. Despite this simple setting, several mixing layer properties mentioned above are retained. The findings can also be compared with those from other numerical studies as well as physical experiments. As a result, the simulations contribute to the numerical simulation of more complex flows. This is illustrated in the present work as well by means of an LES performed for a higher Reynolds number and a larger flow domain. Finally we mention that, although the latter two sections have been devoted to the mixing layer in particular, some of the issues can be applied to the whole range of turbulent shear flows.

1.3 Purpose and outline of this thesis

The purpose of the research described in this thesis is first recalled from a very broad and long-term point of view. Next, the stages towards the present research are further specified. The goal on the long term can be described as follows:

1. To be able to predict and understand the behaviour of complex turbulent shear flows

More specifically, this involves exploring the underlying principles of turbulent shear flows. We mainly consider statistical quantities and properties of evolving coherent structures. The instantaneous behaviour observed in specific simulations is important as well, since it allows a detailed comparison between two different numerical simulations which is relevant for validation purposes. We also focus on properties which are typical for a certain configuration, like the mixing layer growth rate.

The method we use is numerical simulation. Because we are interested in the behaviour of complex turbulent shear flows, we in particular consider the

LES technique. The mixing layer has favorable properties in this respect. A subsequent level of research can therefore be formulated as follows:

2. Exploration of the use of LES for the numerical simulation of turbulent mixing layers

Whether LES can be used depends, *e.g.*, on the available computer power and the resolution at which LES gives reliable results. Furthermore, we consider the feasibility of simulations for a computational domain that could replace the laboratory experiment. The computational setting should be as small and simple as possible. Moreover, it should not affect typical mixing layer properties such as the transition to turbulence by means of vorticity rollers that pair and approximate self-similarity in the turbulent regime. Therefore the present study starts with a 'minimal setting' which only allows a single structure in spanwise direction. This configuration is used to verify various aspects of the numerical computation. After this, the domain is extended in spanwise and in streamwise direction. Finally the Reynolds number is increased (Chapter 6).

Another way to deal with the feasibility of LES of the mixing layer is to consider subgrid-modeling for more complex flows. This will also be done in the present work. The disadvantage of so-called dynamic subgrid-models is that a dynamic coefficient is employed which needs artificial adaptations for stability purposes. The coefficient is averaged in the homogeneous direction. Therefore, these models are less suitable for complex flow configurations. In an adapted formulation, the coefficient is based on its time-averaged value instead. Moreover, the CPU time of the LES is reduced compared to standard dynamic subgrid-models (Chapter 6).

The accuracy of the specific subgrid-models that are employed should be sufficiently high. This implies that the LES should correctly model the effects of small scales that are no longer resolved. It can only be verified by comparison with DNS results of the same setting (Chapter 5). This prescribes the following item:

3. Employing databases from DNS of the turbulent mixing layer to test subgrid-models

We have to determine which properties are appropriate for comparison. For example, the mixing layer thickness may not be appropriate while its slope is very suitable. The comparison may be restricted to statistical quantities and does not include instantaneous properties.

On its turn, the DNS results should be compared against results of physical experiments. This favours the use of a spatial setting in the numerical simulations. The extensive database that arises from the DNS may also be used for

modeling purposes in Reynolds-averaged Navier-Stokes (RaNS; Chapter 4). Therefore we should carry out the following:

4. A thorough investigation of the DNS results

This implies a sensitivity analysis of the DNS. We report on DNSs performed at different resolutions and evaluate statistical properties based on several time intervals. In addition we study the response of the mixing layer to different inflow conditions, consisting of either perturbations based on Linear Stability Theory (LST) or a random signal containing a wide variety of frequencies. Furthermore, we vary the dimensions of the computational domain. These studies are intended to validate the numerical approach (Chapter 2). Based on this thorough analysis, the resulting database is used for comparison with other DNS studies of the mixing layer as well as LES and RaNS (Chapter 3).

Summarizing, the outline of this thesis is as follows. In Chapter 2 the configuration for the DNS will be given including the steps that accomplish a DNS containing a laminar region just after inflow followed by stages of transition and turbulence. The resulting database is extensively described. In Chapter 3 the presence of self-similarity and the budgets of turbulence kinetic energy are investigated. Subsequently the results are evaluated from the RaNS point of view in Chapter 4 where several model assumptions are confronted with statistical DNS predictions. In Chapter 5 the LES is described and the results of several models are compared with the DNS results. Finally Chapter 6 is used to discuss results of LESs of complex mixing layers. Conclusions and recommendations for future research are presented in each chapter separately.

Chapter 2

DNS of a spatially developing turbulent mixing layer

In Chapter 1 we already mentioned the Navier-Stokes equations that describe the behaviour of fluid flow. One of the techniques in the simulation of turbulence is direct numerical simulation (DNS). This 'brute force' approach attempts to solve all spatial and temporal fluctuations in the fluid. A sufficiently fine computational grid is required to cover the wide range of scales that are present in the flow. The development of both RaNS and LES benefits from accurate data of a turbulent flow as a point of reference. Databases from DNS are very useful for modeling purposes. Also data is required for the analysis of physical features like self-similarity. The issue of self-similarity requires the accurate and thorough knowledge of statistical data throughout the whole computational domain. In the next chapter, the DNS results of the present work are explored for the presence of self-similarity.

In this chapter the three-dimensional mixing layer is simulated. We recall from Chapter 1 that throughout the present chapter we restrict to the 'minimal mixing layer setting'. This configuration is computationally affordable on the current supercomputers. It therefore allows a thorough investigation of the sensitivity of the reference DNS regarding resolution, time-averaging intervals, locations of the boundaries and variations in the inflow perturbations. Subsequently, the resulting database is employed to support some model approximations in Chapters 3 and 4. It should be emphasized however that the mixing layer that is simulated numerically cannot be realized in the laboratory. Instead, it represents a basic building block from which a self-sustained turbulent mixing layer arises.

The chapter is organized as follows. In Section 2.1 we introduce the numerical method used to solve the three-dimensional compressible Navier-Stokes equations. A validation of the DNS in two dimensions using Linear Stability

Theory is presented. Section 2.2 gives a specification of the reference DNS. Instantaneous results are shown to illustrate the small scales that are present in the turbulent mixing layer as well as the process of helical pairing. The time-averaging process and a measure for its convergence is introduced in Section 2.3. This is followed by the analysis of the response of several quantities to changes in the numerical setting. We summarize our findings in Section 2.4.

2.1   Numerical method and validation

In this section we first formulate the $3D$ compressible Navier-Stokes equations. Subsequently, we describe the numerical method and present validation results through comparison with Linear Stability Theory (LST).

2.1.1   Governing equations

The Navier-Stokes equations represent conservation of mass, momentum and energy and can be written in Cartesian coordinates as

$$\partial_t \rho + \partial_j(\rho u_j) = 0, \tag{2.1}$$

$$\partial_t(\rho u_i) + \partial_j(\rho u_i u_j) + \partial_i p - \partial_j \sigma_{ij} = 0 \quad (i = 1, 2, 3), \tag{2.2}$$

$$\partial_t e + \partial_j((e + p)u_j) - \partial_j(\sigma_{ij} u_i) + \partial_j q_j = 0. \tag{2.3}$$

We use the summation convention which employs summation of a repeated index over all its values. The symbols ∂_t and ∂_j denote the partial differential operators $\partial/\partial t$ and $\partial/\partial x_j$ with respect to time (t) and spatial coordinate (x_j) respectively. Furthermore, ρ denotes the density, u_j the j-th component of the velocity vector, p the pressure and e the total energy density which is given by:

$$e = \frac{p}{\gamma - 1} + \frac{1}{2}\rho u_i u_i, \tag{2.4}$$

where γ is the adiabatic gas constant. Moreover, σ_{ij} is the stress tensor which is a function of the velocity vector $\mathbf{u}$ only since we assume constant viscosity:

$$\sigma_{ij} = \frac{1}{Re}S_{ij}(\mathbf{u}) = \frac{1}{Re}(\partial_j u_i + \partial_i u_j - \frac{2}{3}\delta_{ij}\partial_k u_k), \tag{2.5}$$

with Re the Reynolds number, S_{ij} the rate of strain tensor[1] and δ_{ij} the Kronecker delta. Furthermore, $\mathbf{q}$ is the heat flux vector, given by

$$q_j = -\frac{1}{(\gamma - 1)RePrM_\infty^2}\partial_j T, \tag{2.6}$$

---

[1]Note that the strain rate tensor is sometimes defined as $S'_{ij} = \partial_j u_i + \partial_i u_j$. For the incompressible setting, the difference between S_{ij} and S'_{ij} vanishes since $\partial_k u_k = 0$.

where Pr is the Prandtl number and M_∞ the Mach number of the upper free-stream. The temperature T is related to the density ρ and the pressure p by the ideal gas law:

$$T = \gamma M_\infty^2 \frac{p}{\rho}. \tag{2.7}$$

Throughout we use $\gamma = 1.4$ and $Pr = 1$. The Reynolds number is based on the upper free-stream velocity, density and viscosity and half the vorticity thickness at the inflow. Both the upper and lower stream dimensionless temperatures are equal to one.

Among the various approaches in modern turbulence simulations direct numerical simulation (DNS), Reynolds-averaged Navier-Stokes (RaNS) modeling and large-eddy simulation (LES) are important classes. In DNS, the full, time-dependent Navier-Stokes equations are solved numerically, essentially without approximations other than of numerical origin. However, DNS is much too expensive to be used in most cases of practical interest and is limited to relatively modest Reynolds numbers and quite simple geometries. In the RaNS approach, only steady solutions or time scales much longer than those of the small-scale turbulent motion are computed. The effect of the unsteady turbulent velocity fluctuations is modeled according to a variety of physical approximations requiring the modeling of the Reynolds stress tensor to which we turn later. In contrast with the statistical filter used in RaNS, the data reduction in LES is based on the introduction of a spatial filter. Computational time and memory can significantly be reduced in RaNS and LES. This allows for simulations in more complex cases than possible with DNS, at the expense of having to introduce models representing the effects of the small and rapid phenomena. DNS results at low Reynolds numbers can be used to support the model approximations.

We consider turbulent flows which are two-dimensional and steady after statistical averaging. A filter is introduced, that implies averaging over the homogeneous spanwise direction and over time. In particular, for any flow property ϕ we define

$$\bar{\phi}(x_1, x_2) \equiv \lim_{T \to \infty} \frac{1}{(T - T_0)} \int_{T_0}^{T} dt \left[\frac{1}{L_3} \int_0^{L_3} dx_3 \ \phi(x_1, x_2, x_3, t) \right] \tag{2.8}$$

with L_3 the spanwise extent (see Figure 1.5). In actual simulations T_0 is taken large enough for transients to have disappeared, whereas its value is not relevant if the limit in (2.8) is sufficiently well determined. For simplicity of notation, the so-called Favre-averaging is introduced in compressible flows [31]:

$$\widetilde{\phi} \equiv \overline{\rho\phi}/\bar{\rho}. \tag{2.9}$$

When the bar-filter is applied to the Navier-Stokes equations (2.1)-(2.3), the nonlinear terms give rise to expressions which cannot be expressed in terms of the filtered variables $\bar{\rho}$, $\widetilde{u}_j$ and $\bar{p}$. Therefore, modeling is required in order to close the system of equations. The most important term is the Reynolds stress tensor, R_{ij}, with

$$\bar{\rho} R_{ij} = \overline{\rho u_i u_j} - \overline{\rho u_i}\ \overline{\rho u_j}/\bar{\rho} = \bar{\rho}(\widetilde{u_i u_j} - \widetilde{u}_i \widetilde{u}_j). \tag{2.10}$$

In literature, R_{ij} is often expressed as[2] $\overline{\rho u_i'' u_j''}/\bar{\rho}$ [64], with $u_i'' = u_i - \widetilde{u}_i$ the velocity fluctuation in the i-th direction. The components of the Reynolds stress tensor are referred to as the streamwise, normal and spanwise turbulence intensities, R_{ii}, with $i = 1, 2, 3$, and the Reynolds stress R_{12}. The components R_{13} and R_{23} are negligible in our application. The remaining terms can be deduced from the former since $R_{ij} = R_{ji}$.

2.1.2   Numerical method

The three-dimensional compressible Navier-Stokes equations (2.1)-(2.3) can concisely be written as

$$\partial_t \mathbf{U} + \partial_j f_j = 0, \tag{2.11}$$

where the state vector $\mathbf{U}$ contains the densities of the conserved variables $(\rho, \rho u_i, e)$ and f_j is the total flux in the x_j direction. The flux consists of two parts: a convective part containing first order spatial derivatives of $\mathbf{U}$ and a viscous part containing second order spatial derivatives. Several numerical schemes for the spatial discretization have been developed and compared for boundary layer flow [105]. For the convective terms on a uniform grid we use a fourth-order accurate scheme of the following form [102]:

$$(\partial_1 f)_{i,j,k} = \frac{1}{\Delta x_1} \sum_{n=-2}^{n=2} w_n^D\, s_{i+n,j,k} \tag{2.12}$$

$$\text{with} \qquad s_{i,j,k} = \sum_{n=-2}^{n=2} w_n^I\, g_{i,j+n,k} \ \text{ and } \ g_{i,j,k} = \sum_{n=-2}^{n=2} w_n^I\, f_{i,j,k+n}. \tag{2.13}$$

Here we introduced weights $w^D = [1, -8, 0, 8, -1]/12$ for differentiation and $w^I = [-1, 4, 10, 4, -1]/16$ for interpolation. These weights were obtained using

---

[2]Note that the Reynolds stress tensor is defined according to the incompressible equivalent, $\overline{u_i' u_j'}$, with $u_i' = u_i - \bar{u}_i$, and therefore prescribing the division over $\bar{\rho}$. In some works, $\bar{\rho} R_{ij}$ is called the Reynolds stress tensor. When comparing the present results directly with incompressible experiments, we employ the notation $\overline{u_i' u_j'}$ for both settings.

the requirement that polynomials up to degree four are differentiated and interpolated exactly. In this spatial discretization method the derivative in, *e.g.*, the x_1-direction is pre-averaged over the other coordinate directions in order to generate a robust scheme which removes specific π-modes. The derivatives in other coordinate directions follow similarly. This method has been used extensively and found to be quite efficient [102, 105]. The viscous flux contains second-order derivatives which are computed in two steps. We first construct the 'inner' derivative $\partial_1^{in} f$ in the cell centers $(i + \frac{1}{2}, j + \frac{1}{2}, k + \frac{1}{2})$ by making use of vertices in the block $[i-1, i+2] \times [j-1, j+2] \times [k-1, k+2]$. Next, $\partial_1^2 f$ is computed in vertices (i, j, k) using the derivatives $\partial_1^{in} f$ in cell centers $[i - \frac{3}{2}, i + \frac{3}{2}] \times [j - \frac{3}{2}, j + \frac{3}{2}] \times [k - \frac{3}{2}, k + \frac{3}{2}]$ with the same method. The weights for the viscous terms are computed according to the same principle as the convective weights and yield a method that is fourth order accurate on uniform grids as is described in more detail in [105].

With the method of lines applied to (2.11), a system of ordinary differential equations of the form

$$\frac{d\mathbf{U}}{dt} = F(\mathbf{U}), \tag{2.14}$$

arises with $\mathbf{U}$ now denoting the vector of all densities of conserved variables in all grid-points and F the total discrete flux vector. This system of differential equations is advanced in time using a second order four-stage compact-storage Runge-Kutta method. Within one time step Δt we perform

$$\mathbf{U}^{(n)} = \mathbf{U}^{(0)} + \alpha_n \, \Delta t \, F(\mathbf{U}^{(n-1)}) \quad (n = 1, 2, 3, 4) \tag{2.15}$$

with $\mathbf{U}^{(0)} = \mathbf{U}(t)$, $\mathbf{U}^{(4)} = \mathbf{U}(t + \Delta t)$ and $\alpha = [\frac{1}{4}, \frac{1}{3}, \frac{1}{2}, 1]$. The time step Δt follows from the so-called CFL condition with a CFL-number that equals 1.8 suggested by other studies [102]; well below the theoretical value of 2.8.

Previously, the above method has successfully been used in boundary layer flows and in temporal mixing layer flows. In the spatial setting considered here, the computational domain is limited through the introduction of artificial boundaries which need to be taken into account separately. Especially the outflow boundary requires careful attention since no physical boundary condition is available in case of turbulent flow. A buffer domain was introduced in order to damp reflections that may occur in the vicinity of the numerical outflow boundary [105]. Two common ways found in literature to achieve this goal involve either a considerable increase of the viscosity in the buffer or a gradual change of the governing equations into a parabolic system [58, 91]. When explicit time stepping is used, the reflections should be damped by a very large increase of the viscosity in order to be effective, which results in a considerable limitation of the allowable time step. On the other hand, applying the parabolizing procedure yields only a gradual effect and requires the use

of quite extended, and hence costly, buffer domains in order to be effective. Instead, we use a direct relaminarization technique in which the turbulent solution that enters the buffer region is forced towards a steady mean flow near the end of the buffer. The damping procedure used here is formulated such that its effect is nearly grid independent and is found to be robust and with minimal upstream influence. This procedure was combined with characteristic wave relations [72] which were also used for the two free-stream boundaries.

The solution is forced at the subsonic inflow using a steady mean state vector $(\mathbf{u}, T)$ onto which unsteady perturbations are added. The remaining fifth variable is the pressure which is extrapolated from inside the flow domain. The numerical method used for the computations appears flexible, computationally efficient and robust and can be used in both laminar and turbulent flows without any flow-dependent adjustments of numerical parameters [23, 105]. A more detailed description of the numerical method, the boundary conditions and the buffer domain technique can be found in ref. [105].

2.1.3   Comparison with LST in two dimensions

In this subsection, the numerical method and boundary conditions are validated by comparing with Linear Stability Theory (LST). To that purpose we superimpose small perturbations at the inflow on a parallel base flow. The perturbations were derived from LST and provide a time-dependent forcing of the flow at the inflow boundary. We use the mixing layer in $2D$ to illustrate the development in the linear regime [23, 106]. Only one perturbation eigenfunction is imposed in order to be able to accurately compare the results with LST.

We start the spatial simulation with a laminar field. For the parallel spatial mixing layer this consists of a tanh profile for the streamwise velocity, uniform pressure and the Busemann-Crocco law [73] for the temperature. The Reynolds number is set to 200 and temperature is scaled by a reference temperature of 276 K. In the normal direction the domain size is 60. The extent of the domain in the streamwise direction is 6 wavelengths λ_F of the fundamental LST mode and a flux forcing term is added to the Navier-Stokes equations in order to maintain an average parallel flow. This method of validation was also used in [105] where a more detailed description is given.

We select the most unstable $2D$ mode from a linear stability analysis and add this to the base flow at the inflow boundary with amplitude 10^{-4}. We use a streamwise wavenumber $\alpha = \alpha_r + i\alpha_i = 0.392 - i\ 0.0532$ and circular frequency $\omega = 0.296$. This results in a phase velocity which is very close to the mean velocity of the two free-streams. In the simulations we employ two different grids. The coarser grid has 160 points in streamwise direction and 64 in normal direction, uniformly distributed in both directions. In the finer grid,

the number of points in normal direction is doubled, resulting in about equal grid sizes in both directions. Grid refinements in the streamwise direction have been considered for boundary layer flow and can be found in [105]. There it was found that about 25 points per fundamental wavelength resulted in a suitable accuracy for the same numerical method as used here and leads to the number of 160 mentioned above.

The correspondence between the numerical solution obtained from DNS and the results of LST can be inferred from the spatial development of the Kelvin-Helmholtz (KH)-waves, the logarithm of their amplitudes and from the corresponding growth rates. The latter quantity is the most precise test for comparison purposes. The Kelvin-Helmholtz waves are plotted in Figure 2.1 for the two resolutions considered here and compared with LST. Results of the logarithm of the spatially developing amplitude and the growth rate can be found in [23]. It is clear from Figure 2.1 that the DNS with the higher resolution compares very well with the results predicted by LST. The coarse-grid DNS displays a phase difference with the LST result. The DNS result displays a smooth damping in the buffer. Variations in the size and location of the buffer were shown not to lead to noticeable changes as was already observed in [105]. Furthermore, the upstream influence of the buffer domain appears very small. Finally, we note the damping of the KH-wave towards the laminar solution in the buffer, consistent with the direct damping procedure
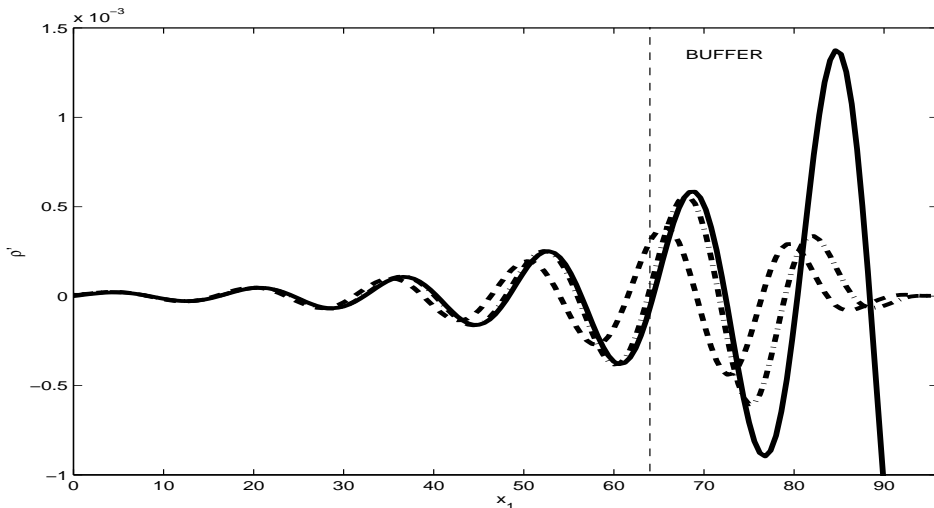

Figure 2.1: Kelvin-Helmholtz waves as a function of the streamwise coordinate, x_1, for the instantaneous density fluctuation in streamwise direction at time 552. The coarse-grid $(--)$ and fine-grid $(-\cdot)$ DNS results as well as the LST prediction $(—)$ are included.

used here. Basically, our findings confirm those of the comparison of results of LST with Tollmien-Schlichting waves in the boundary layer DNS from [105] at the same resolution. So, for a completely different flow, without adjusting numerical parameters, an equally accurate and efficient numerical treatment of the boundaries is obtained. Next, the steps towards a DNS that displays turbulence are described. The reference DNS results are presented. These are followed by a sensitivity analysis in which we consider the response to variations in numerical parameters.

2.2   Reference direct numerical simulation

Many physical experiments involving the mixing layer have been performed in a wind tunnel containing a streamwise splitter plate that separates the flow. We assume the flow on both sides of the splitter plate to be laminar boundary layer flow with different free-stream velocities. At the end of the splitter plate both streams merge and turbulence will develop, emanating from the centerplane at $x_2 = 0$, somewhat further downstream. The goal of this section is to describe the reference DNS. A uniform grid is used in all directions. Guided by previous results [102, 105], we employ a resolution of 25 points per perturbation wavelength of the most unstable mode in the streamwise and 128 points in the normal direction respectively in the reference setting. Furthermore, we take 32 points in the spanwise direction which covers one spanwise wavelength. This is combined with the symmetry as described in [80], which reduces the computer time and storage requirements by a factor of two.

For the mean solution a shooting method is used to solve the boundary layer equations for steady two-dimensional flow of a compressible perfect gas with uniform pressure. This is done at an inflow location of $x_i = 47.5$. The solution is subsequently distributed downstream to different locations $\hat{x}_1$ using the scaling relation $\hat{x}_2 = x_2\sqrt{\hat{x}_1/x_1}$ [90, 105]. More details about the particular mixing layer setting where the shooting is simultaneously performed from the centerline to both free-streams can be found in [78]. From the fact that the mean solution of u_1 equals 0.76 at the numerical centerplane ($x_2 = 0$) it can be deduced that the mixing layer centerplane, defined by $\tilde{u}_1 = 0.75$ bends down slightly towards the low-speed side corresponding to the asymmetric entrainment reported in experiments [28, 67].

On top of this mean solution we impose inflow perturbations that are further specified below. In order to describe some long-time characteristics of the flow we look for a time scale that represents the behaviour of large structures of the turbulent mixing layer. We use the period of the fundamental LST mode, T_F, which is independent of numerical parameters like the resolution and the length of the streamwise computational domain.

2.2.1   Specification of the Reference Simulation

We consider mixing layer flow with Reynolds number and Mach number as in Section 2.1.3. With these parameters we are able to reach turbulent flow in the mixing layer some distance downstream of the splitter plate and we can make comparisons with results of incompressible experiments since the effect of compressibility is small. Besides, the parameters correspond to the ones in [104]. So we can compare a temporal and spatial setting regarding for example the domain size and grid resolution required for turbulence to be captured.

The steps towards simulation of turbulence in a mixing layer are described in the rest of this section and illustrated by contour plots of the spanwise vorticity. In order to maintain simplicity of the inflow conditions we try to minimize the number of modes. On the other hand it is clear that we need several modes in order to realize transition to turbulence in an efficient and computationally affordable way.

We first select the most unstable $2D$ mode from a linear stability analysis as point of departure in the construction of a suitable inflow perturbation. In order to be able to reach a situation of transition and turbulence a sufficiently long computational box in the streamwise direction is required. A first indication of the streamwise length of the box comes from an equivalent temporal mixing layer study with the same convective Mach number [104]. The instant at which the solution exhibits turbulence in the temporal setting is translated in a streamwise location for the current spatial setting using the convective velocity $U_c = (U_1 + U_2)/2$ and the velocity difference ΔU in both settings [77]. This relation can be summarized as follows:

$$t\Delta U\Big|_{temporal} = \frac{x_1 \Delta U}{U_c}\Big|_{spatial}. \tag{2.16}$$

Based on this comparison, we employ a streamwise domain of 16 wavelengths and a buffer that consists of two wavelengths. We next show the effect of the LST modes that are imposed at the inflow boundary.

We start with a DNS where the perturbations consist solely of the most unstable $2D$ mode at amplitude 0.1. In Figure 2.2.a we have shown isolines of the spanwise vorticity in a characteristic x_3-plane and time $t = 552$. At regular distance to each other, vortex rollers are present on the centerline. These regions are characterized by local peaks in the negative spanwise vorticity. The amount of vorticity decreases in downstream direction. It is clear that each of the 18 structures corresponds directly to the LST perturbation. In this laminar flow, only negative spanwise vorticity is present. No transition occurred either when only the most unstable fundamental $2D$ and $3D$ modes were used at the inflow, which shows the importance of the inclusion of subharmonic
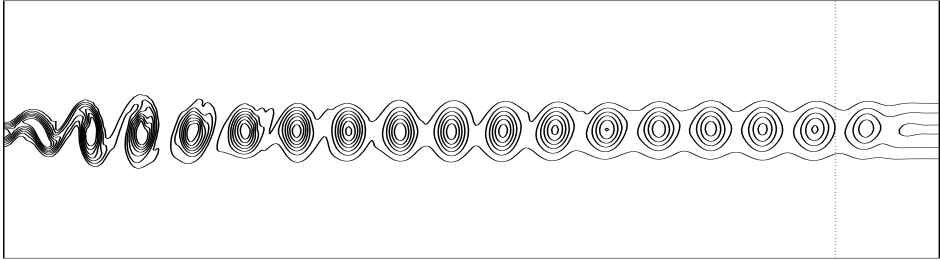
a: low amplitude perturbation: only the fundamental mode
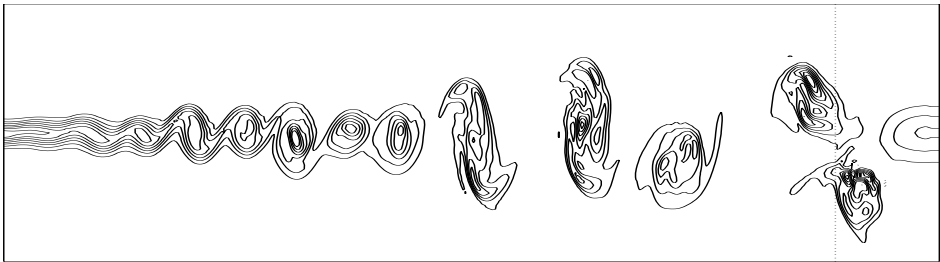
b: low amplitude perturbations: both $2D$ and $3D$ modes

c: high amplitude perturbations: more contribution of the $3D$ modes
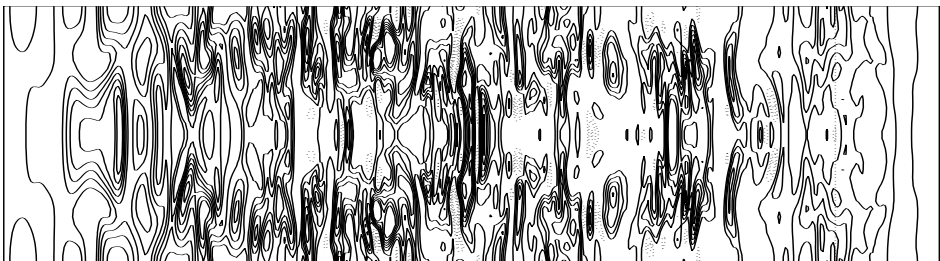
d: centerplane equivalent of Fig. c

Figure 2.2: Spanwise vorticities at time 552, plotted for negative (—) and positive $(\cdots)$ isovalues for $\pm(0.03, 0.06, \ldots, 0.21)$ in the planes $x_3 = L_3/4$ ($x_2 = [-16, 16]$) (a-c) and $x_2 = 0$ (d) with x_1 the horizontal axis. The buffer area is behind the dotted line.

modes. The well-known pairing process was observed with the additional inclusion of the first two subharmonic modes of the fundamental $2D$ mode (with wavelengths two and four times that of the fundamental mode).

For efficient full transition to turbulence additional subharmonic $3D$ modes were needed as well. In total, we incorporated three $2D$ modes (fundamental and the first two subharmonics) and three pairs of the $3D$ equivalents, resulting in the following total perturbation Q at the inflow boundary:

$$Q(x_2, x_3, t) = \epsilon \sum_{j=1}^{N} A_j \left(\Psi_{r_j}(x_2) \cos(\gamma_j) - \Psi_{i_j}(x_2) \sin(\gamma_j) \right). \qquad (2.17)$$

Here, ϵ and A_j denote the total and j-th relative amplitude and Ψ_j the complex eigenfunction (consisting of a r(eal) and i(maginary) part) that is multiplied by a goniometric function of $\gamma_j = \beta_j x_3 - \omega_j t + \phi_j$ with β the spanwise wavenumber, ω the real frequency and ϕ the phase. The number of modes, N, equals 9 for this reference case and this appears the minimal number which leads to a DNS with turbulence within a reasonable distance from the inflow boundary. The values for all the parameters are collected in Table 2.1. The complex streamwise wavenumber, α, is included as well to show the resulting streamwise wavelengths and growth rates predicted by LST. The perturbation period that is used as time scale for the long-time characteristics, T_F, equals $2\pi/\omega = 21.2$. Finally, note that the streamwise perturbation velocity closely corresponds to the centerline streamwise velocity and approximates the convective velocity, *e.g.*, for the fundamental mode: $\omega/\alpha_r = 0.755 \approx U_c = (U_1 + U_2)/2 = 0.75$. We take no phase differences for the $3D$ modes in view of the symmetry condition in the spanwise direction. The phases of the $2D$ subharmonics were chosen differently from the $2D$ fundamental mode in order to minimize the distance between parings [20, 65]. When taking equal relative amplitudes that sum up to 1 ($A_j = 1/9$) and a total amplitude (ϵ) of 0.1, the result from Figure 2.2.b

		$2D$				$3D$		
	α_r	α_i	ϕ	ω	α_r	α_i	β	ω
F	0.392	-0.0532	0.125 π	0.296	0.391	-0.0310	$\pm$ 0.391	0.296
$S1$	0.196	-0.0405	0.375 π	0.151	0.196	-0.0208	$\pm$ 0.391	0.149
$S2$	0.0980	-0.0235	0.5 π	0.0772	0.0978	-0.0093	$\pm$ 0.391	0.0745

Table 2.1: Wavenumbers $\alpha = (\alpha_r, \alpha_i)$, β phases ϕ and frequencies ω of the fundamental mode (F) and its first two subharmonics ($S1$, $S2$) for the $2D$ and $3D$ perturbations. Together this results in three $2D$ modes and three pairs of $3D$ modes.

is obtained where only large scale structures but no turbulent features are present within the domain.

We observed that both the relative amplitudes of the $3D$ modes and the total amplitude of all modes together should be large enough in order to generate turbulence well within the computational domain while retaining a laminar and a transitional region. We therefore took the amplitude (ϵ) equal to 0.2 and the contribution of the $3D$ modes ($A_j =$0.145) was taken approximately three times larger than that of the $2D$ modes ($A_j =$0.0433). These specifications result in an efficient DNS that contains transitional features, *e.g.*, associated with helical pairing, and turbulent structures. Other modes, perturbation amplitudes or domain lengths may finally result in a turbulent solution as well but the present selection is particularly effective and computationally affordable.

2.2.2   Results of the Reference Simulation

In the remaining part of this section results of the DNS specified above are shown. We can distinguish the different stages from laminar through transitional to turbulent flow in Figure 2.2.c. We observe that patches of positive vorticity appear starting around one third of the streamwise domain. Also we note that the peak value of the negative spanwise vorticity normalized with the velocity difference approximately corresponds to that of the temporal mixing layer from [104]. The temporal evolution of the solution is sampled at two streamwise locations on the numerical centerplane ($x_2 = 0, x_3 = L_3/4$) in the laminar and turbulent regime. These locations are denoted by A ($x_1 = 100$) and B ($x_1 = 250$) in the remaining part of this chapter and indicated in Figure 2.2.c. These signals will be compared with the corresponding time evolution at different resolutions and sizes of the computational domain later on. We have plotted the spanwise vorticity in the centerplane ($x_2 = 0$) in Figure 2.2.d. The development of so-called Λ-vortices can clearly be seen just after location A. The presence of these Λ-vortices has also been reported in other numerical studies of the temporal and spatial compressible mixing layer using DNS and LES [54, 65, 104]. In Figure 2.3 spanwise vorticity isosurfaces are shown at $t = 552$ and restricted to the laminar and transitional parts of the flow domain. We show the process of a three-dimensional pattern of staggered Λ-vortices resulting in helical pairing which was observed for the first time in mixing layer experiments described in [19]. Further downstream this develops into a turbulent state where many small scales are present. This process is next illustrated with the energy spectrum at several streamwise locations which shows that smaller scales enter the system until a state of sustained turbulence is reached.

The spanwise spectrum for the kinetic energy density at the numerical centerline $x_2 = 0$ is defined in terms of the Fourier transform of the correlation
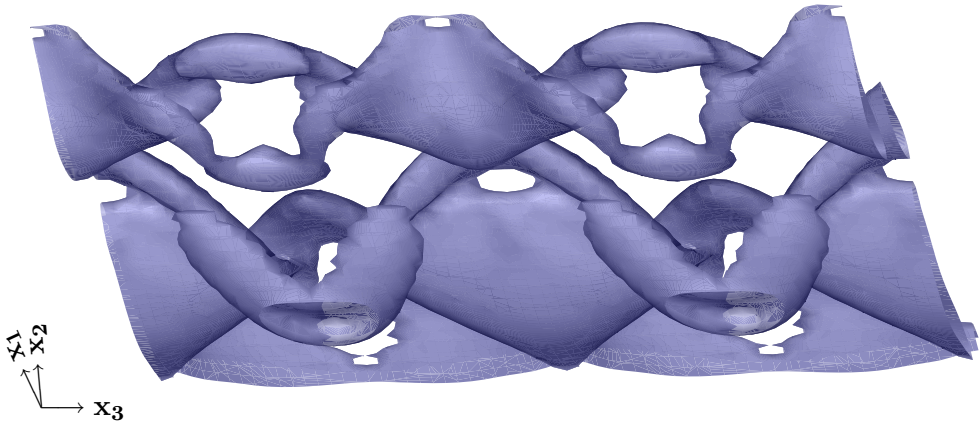
Figure 2.3: Instantaneous spanwise vorticity isosurfaces at value -0.12 from time=552 for the LST perturbed inflow in the domain $[96, 128] \times [-5, 5] \times [-0.5L_3, 1.5L_3]$.

function of u_i [34, 78]. This results in

$$E(x_1, k_3) = \frac{1}{(T - T_0)} \int_{T_0}^{T} \hat{u}_i(x_1, k_3, t) \, \hat{u}_i^*(x_1, k_3, t) dt, \qquad (2.18)$$

with $\hat{u}_i^*(x_1, k_3, t)$ the complex conjugate of the Fourier coefficient $\hat{u}_i(x_1, k_3, t)$. The instantaneous values of $\hat{u}_i(x_1, k_3, t) \, \hat{u}_i^*(x_1, k_3, t)$, with spanwise wavenumber k_3, are averaged over time. Normalization factors in the Fourier coefficients are omitted, $T_0 = 25 \, T_F$ and $T = 60 \, T_F$. In Figure 2.4.a, the centerline kinetic energy is plotted as a function of x_1 for several values of k_3. The coefficient for $k_3 = 0$ represents the mean velocity component which is approximately constant for all values of x_1 and therefore not shown. At the inflow boundary, only one spanwise mode is imposed on top of the average solution. Further downstream, more and more modes come up in the system. This is also clear from Figure 2.4.b where $E(x_1, k_3)$ is shown as a function of k_3 for several streamwise stations. Comparison of the profiles in Figure 2.4.b clearly shows the collapse of the Fourier coefficients beyond $x_1 \approx 120$. This presence of smaller modes during a long streamwise interval shows that the present DNS is capable of attaining a state of fully developed turbulence. The second part of the domain displays a slight linear decrease that is characteristic for all values $k_3 > 1$. In the buffer, the Fourier coefficients for $k_3 > 0$ decrease to zero again. More results are shown in the next section where we focus on the sensitivity of the reference DNS.
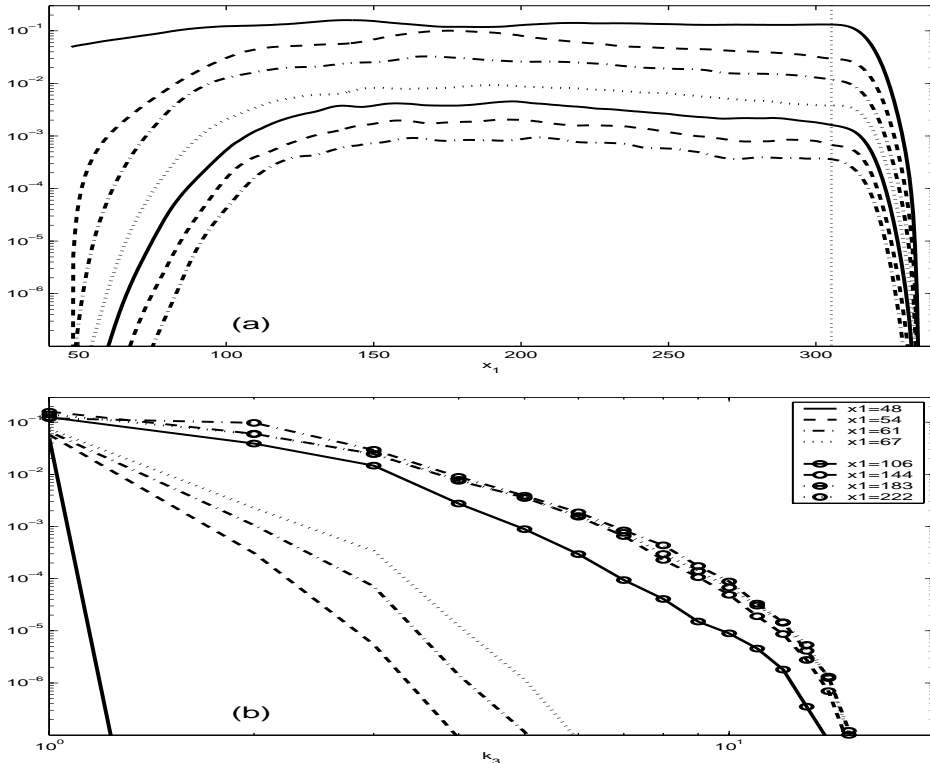
Figure 2.4: Energy spectrum of the reference DNS with LST inflow perturbations. The kinetic energy density $E(x_1, k_3)$ is plotted as a function of x_1 for modes $k_3 = 1(\text{—})$ to $7(-\cdot)$ (a) and as a function of k_3 for several equidistant streamwise locations: $x_1 = 48(\text{—})$ to $67(\cdots)$ and (with symbols) $x_1 = 106(\text{—})$ to $222(\cdots)$ (b).

2.3   Sensitivity of the reference DNS

We will describe DNSs in which relevant numerical properties are systematically varied in order to infer the sensitivity of the reference DNS described in the previous section. This is done for some averaged variables, for the Reynolds stress tensor that involves averaged fluctuations, and for some instantaneous solution components.

This section starts with results of DNSs at two other resolutions which are compared with those of the reference DNS. We continue with a study on the length of the time-averaging interval for the different types of quantities described above. Next, the sensitivity of the solution is considered when changing the size of the computational domain. Finally, we compare results of two different inflow perturbations.

2.3.1 Grid resolution

The DNS described in the previous sections is repeated at both a coarser and a finer resolution. The specifications are shown in Table 2.2 where N_i denotes the number of grid points in the i-th direction. The computational domain is the same for all three resolutions: $L_1 = 290, L_2 = 60, L_3 = 16.07$. The grid spacings of the fine resolution are chosen about the same in all three directions, 0.32, 0.31 and 0.25 and correspond to those in the fine resolution of [20].

In Figures 2.5 and 2.6 the instantaneous streamwise and normal momentum density is compared for varying resolutions at the numerical centerplane ($x_2 = 0, x_3 = L_3/4$) in the laminar and turbulent regime respectively, monitoring at location A and B respectively. It is clear from Figure 2.5 that the solutions arising at the two finer resolutions coincide in the laminar regime and deviate further downstream in the turbulent regime. The coarse-resolution signal is included in Figure 2.6 for ρu_2 at location A. The main resolution effect involves an inaccurate prediction of the solution field, especially at location B. A phase difference is present between the result of the coarsest grid and that of the two other grids, which was also observed for the LST signal with the same resolution for the normal direction shown in Figure 2.1. This phase difference is almost independent of time.

Comparing instantaneous solutions is the most severe test when the sensitivity is considered. We next consider less sensitive properties. In Table 2.3 the mean of the momentum densities and the root mean square (rms) of the fluctuations are collected at the centerplane locations A and B for all three resolutions. Since the normal momentum density is an odd function of x_3, the symmetry assumption mentioned before results in $\overline{\rho u_3} = 0$. The time-average of ρu_1 in A is lower than that in B. This illustrates the slight asymmetric entrainment of the mixing layer towards the low-speed side, corresponding with experimental results already mentioned in this chapter.

At location A the deviation between the middle- and fine-resolution mean momentum densities is of order 10^{-4}. Further downstream, this value gets larger. The deviation between the middle- and coarse-grid mean results is also larger than this value. This is also true for the rms of the fluctuations.

resolution	coarse	middle	fine
N_1	300	450	900
N_2	64	128	192
N_3	16	32	64

Table 2.2: Three resolutions employed to study the sensitivity in grid resolution.
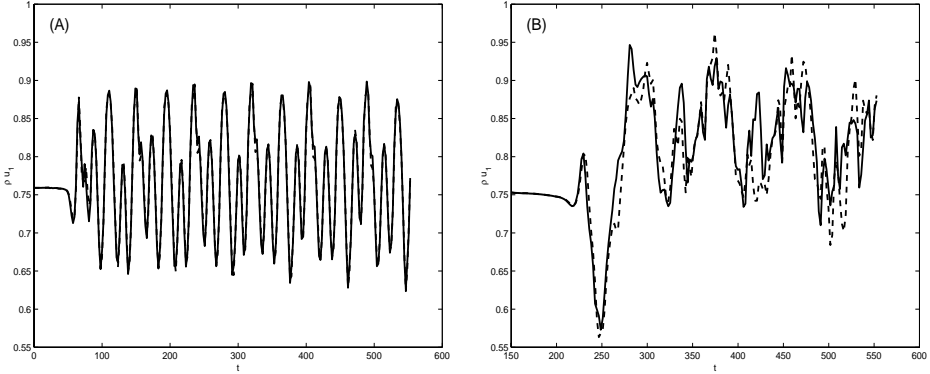
Figure 2.5: Time evolution of the streamwise momentum density ρu_1 at stream-wise locations A $(x_1 = 100)$ and B $(x_1 = 250)$ on the numerical center-plane $(x_2 = 0, x_3 = L_3/4)$ for the middle $(--)$ and fine $(—)$ resolution.
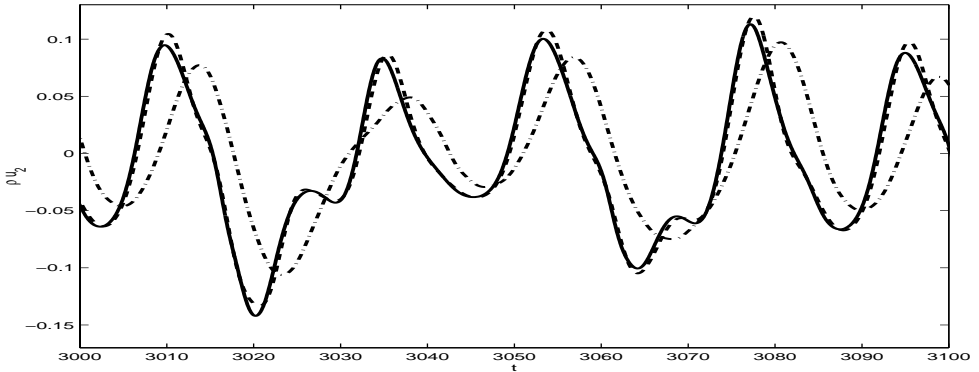
Figure 2.6: Time evolution of ρu_2 at A $(x_1 = 100, x_2 = 0, x_3 = L_3/4)$ for the coarse $(-\cdot)$, middle $(--)$ and fine $(—)$ resolution.

| | ρu_1 | | | | ρu_2 | | | | ρu_3 | |
| | mean | | rms E-2 | | mean E-3 | | rms E-2 | | rms E-2 | |
	A	B	A	B	A	B	A	B	A	B
coarse	0.7485	0.767	6.116	7.32	0.5	9.7	5.3	8.7	6.6	7.0
middle	0.7713	0.782	6.471	6.97	-5.9	1.8	6.1	8.2	7.8	7.6
fine	0.7714	0.790	6.473	6.68	-6.2	1.1	6.0	8.3	7.7	7.8

Table 2.3:   Mean values and rms of the fluctuations of the three momen-tum densities at the laminar (A) and turbulent (B) streamwise centerline lo-cations $(x_2 = 0, x_3 = L_3/4)$ based on the time interval $[25\ T_F, 150\ T_F]$ and compared at three resolutions.

The *rms* value is related with the turbulence intensities which we consider next. We compare results of the streamwise turbulence intensity, R_{11}, in Figure 2.7.a. Here, the maximum deviation between the middle and fine resolution equals 5% for $x_1 = 270$ and is a factor two smaller than the maximum deviation between the coarse and fine resolution. Time-averaging was performed from 25 T_F until 150 T_F, and results based on different averaging intervals are compared in the next subsection. The profiles of all components of the Reynolds stress tensor will be discussed and compared with physical experiments in Section 3.1. Finally, we consider the momentum thickness which is defined as [74, 77]:

$$\theta(x_1) = \int_{-L_2/2}^{L_2/2} \bar{\rho}(x_1, x_2) \frac{\Big(U_1 - \widetilde{u}_1(x_1, x_2)\Big)\Big(\widetilde{u}_1(x_1, x_2) - U_2\Big)}{(U_1 - U_2)^2} dx_2. \quad (2.19)$$

The momentum thicknesses arising from the DNS at the different resolutions are shown in Figure 2.7.b. The maximum deviation between the middle- and fine-resolution momentum thickness is 1% which is a factor of two smaller than the maximum deviation between the fine and coarse result.

Summarizing, the coarse DNS gives a fairly reliable impression of the momentum thickness and the resulting growth rate. The middle resolution gives a reliable impression of, *e.g.*, the mean velocities as well as the components of the Reynolds stress tensor. It is clear that at least the fine resolution is needed to describe the instantaneous quantities accurately. These findings regarding the resolution correspond to those found in [104].
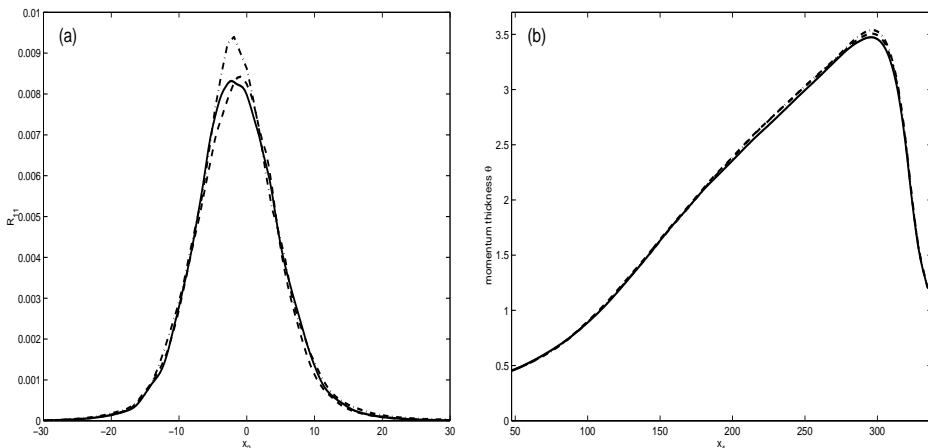

Figure 2.7: Profiles of R_{11} as a function of x_2 at $x_1 = 270$ (a) and momentum thickness θ as a function of x_1 (b) for the coarse ($-\cdot$), middle ($--$) and fine ($-$) resolution.

2.3.2   Time-Averaging process

We introduce the time-averaging process in more detail and define a measure for monitoring convergence of the time-average. Suppose averaging has been performed from time T_0 to time T. This results in a partially averaged flow variable that depends on both the sampling time interval and the spatial coordinates:

$$\overline{\phi}^T(x_1, x_2) \equiv \frac{1}{(T - T_0)} \int_{T_0}^T dt \left[\frac{1}{L_3} \int_0^{L_3} \phi(x_1, x_2, x_3, t)\, dx_3 \right]. \qquad (2.20)$$

It is the finite time equivalent of $\bar{\phi}$ defined in (2.8). Here, we compute $\bar{\phi}^T$ using the trapezoidal rule for the integration over both the spanwise direction and the time.

   In analysing statistical results of a spatially developing flow we should average long enough in time to guarantee a proper estimate of the average solution and its physical properties. To quantify this convergence we introduce the 'residue'

$$\varepsilon(T) = \frac{1}{\Delta} \left[\frac{\int_0^{L_2} dx_2 \int_{x_s}^{x_e} dx_1 \left(\bar{\phi}^{T+\Delta}(x_1, x_2) - \bar{\phi}^T(x_1, x_2) \right)^2}{\int_0^{L_2} dx_2 \int_{x_s}^{x_e} dx_1 \left(\bar{\phi}(x_1, x_2) \right)^2} \right]^{1/2}, \qquad (2.21)$$

where Δ denotes the sampling time step, $[x_s, x_e]$ the 'physical' part of the streamwise computational domain and L_2 the width of the flow domain in normal direction. In practice, $\bar{\phi}$ is approximated by the results of the largest sampling interval available. The residue $\varepsilon(T)$ should decrease to zero for large values of T. It is normalized by a measure of the averaged variable itself to facilitate comparison with the convergence of other variables. Of course the average $\bar{\phi}^T$ depends formally on T_0 as well. However, if $T \gg T_0$ and T_0 is taken sufficiently large for initial transients to have disappeared, the dependence on T_0 can safely be neglected. Throughout this chapter, the averaging process has always started at time $T_0 = 25\, T_F$, at which time the flow is fully developed. The results presented do not change significantly when the averaging is started at a later moment in time.

   In Figure 2.8.a the time-averaging process for the fine resolution is illustrated for R_{33}. The averaging is performed from T_0 until times $T_1 = 70\, T_F$, $T_2 = 110\, T_F$ and $T_3 = 150\, T_F$. The maximum deviation in results of the longer time intervals until T_2 and T_3 equals 2×10^{-4} (6%) for, *e.g.*, $x_1 = 240$ and is a factor of four smaller than the equivalent for the time intervals until T_2 and T_1. Furthermore, the time-averaging process of the momentum thickness is shown in Figure 2.8.b. The three lines almost coincide. The *rms* in the deviation between the results of the shorter time intervals until T_1 and T_2 is within 1% and drops with a factor two for T_2 and T_3.
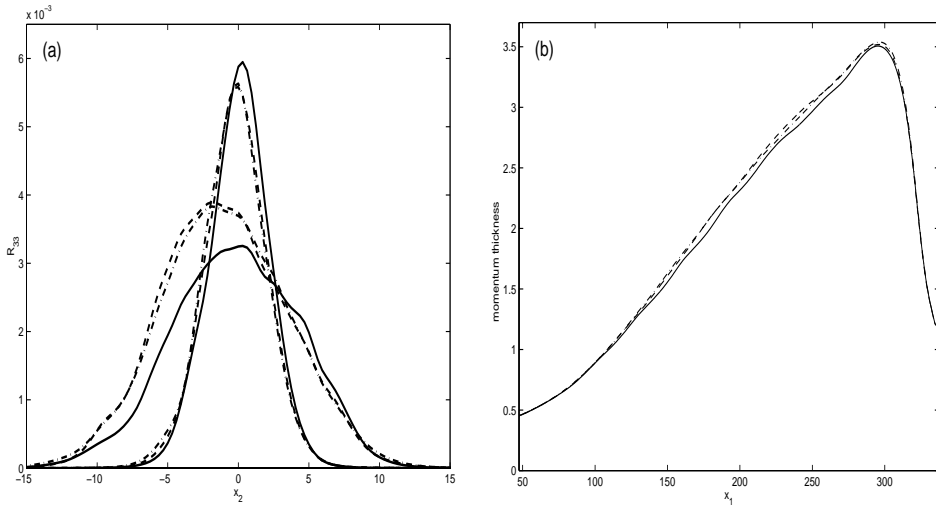
Figure 2.8: Sensitivity of the time-averaging interval for the fine-grid R_{33} as a function of x_2 at values $x_1 = 145$ and $x_1 = 240$ (a) and momentum thickness θ as a function of x_1 (b). For T we employ the (increasing) values T_1 (—), T_2 (− −) and $T_3(-\cdot)$.
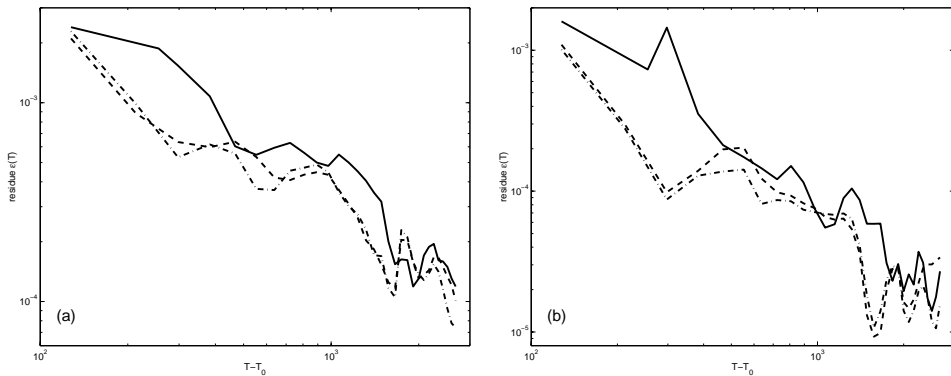
Figure 2.9: $\varepsilon(T)$ for convergence of R_{12} (a) and of $\theta(x_1)$ (b) with $[x_s, x_e] = [120, 265]$ for the coarse (—), middle (− −) and fine ($-\cdot$) resolution.

The residue $\varepsilon(T)$ as defined in (2.21) is illustrated in Figures 2.9.a and 2.9.b for R_{12} and θ respectively for all three resolutions. Both figures show a decrease which is insensitive with respect to the exact choice of the streamwise interval $[x_s, x_e]$ within the total streamwise physical domain $[x_i, x_b]$. It is close for the two finer resolutions where during the last 1000 time units ε is smallest for the fine resolution. Finally, we observe that $\varepsilon(T)$ is smaller for θ than for

R_{12}. This shows that the Reynolds stress tensor is a more sensitive quantity. Although the DNS should be continued much longer to reach a collapse of the Reynolds stress tensor profiles, it appears we have averaged long enough in time to study self-similarity of the DNS results. This will be considered in the next chapter. Before that, we continue this study of the sensitivity of the middle-resolution reference DNS. This is first done with respect to modifications in the locations of the boundaries of the computational domain and finally with respect to variations in the inflow perturbations.

2.3.3   Boundary location

We consider three variations on the reference DNS regarding the computational domain consisting of a physical part followed by a numerical buffer. This involves extending the streamwise physical domain, buffer and domain height and is summarized in Table 2.4. The resulting instantaneous streamwise momentum densities at location B in the turbulent regime (see Figure 2.2.c) are shown in Figure 2.10. The signal from the reference DNS is included as well. The final time of the figure corresponds to two traversal times (defined as L_1/U_c) of the case V_2 ($t = 945$). So, reflected perturbations returning from the outflow boundary should be visible if present. All four signals in the figure behave approximately the same. For the time interval 0-890 the maximum deviation of the instantaneous streamwise momentum density ρu_1 compared to the reference DNS at the turbulent location equals 4%, 13% and 5% for respectively the cases V_1, V_2 and V_3.

For a more quantitative comparison, some values for the mean and *rms* of the fluctuations are collected in Table 2.5. The deviation is largest again for V_2 being 0.003 (0.4%) in the mean value and 0.001 (1.5%) in the *rms.* This implies that related properties like the Reynolds stress tensor, and in particular the momentum thickness that only depends on $\tilde{u}_1$, will not change much as well. So we can conclude that the reference DNS is quite insensitive

	buffer length (λ_F)	domain length (λ_F)	domain height
Ref.	2	16	60
V_1	4	16	60
V_2	2	20	60
V_3	2	16	90

Table 2.4: Configurations of the three variations on the reference DNS with λ_F the fundamental wavelength from LST.
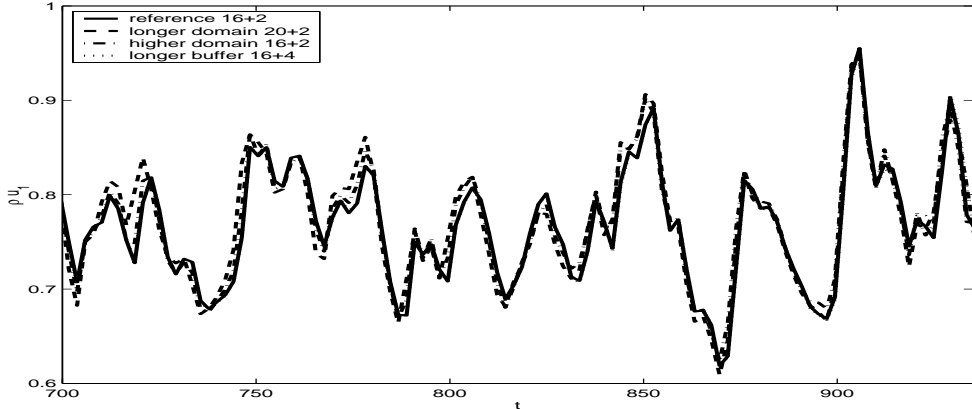
Figure 2.10: Temporal development of ρu_1 at B for the reference DNS(—) and domain extensions $V_2(--), V_3(-\cdot)$ and $V_1(\cdots)$.

ρu_1	Ref.	V_1	V_2	V_3
mean	0.783	0.783	0.786	0.784
rms	0.0664	0.0666	0.0673	0.0661

Table 2.5: Mean values and rms of the fluctuation of the streamwise momentum densities at location B based on the time interval 0-890 for several configurations of the computational domain.

with respect to variations in the buffer length and the sizes of the domain. In the next subsection we consider the sensitivity of the reference DNS when an other inflow perturbation is used.

2.3.4 Inflow perturbations

The inflow is used to force perturbations onto the mixing layer. Several studies stress that the details of initial conditions persist very far downstream [27, 87]. Different inflow perturbations may therefore imply different transitional behaviour. As a result, the sensitivity of the results arising from different inflow perturbations can only be considered for the turbulent regime. Besides, only properties that are supposed not to change in streamwise direction can be compared, like the growth rate of a mixing layer thickness and the peak values of the Reynolds stress tensor. The experimental observations display discrepancies in characteristic features like the growth rate [87]. The study of inflow boundary sensitivity also allows to consider the existence of multiple

similarity states.

An overview of some alternatives of perturbations used to generate tur-
bulence in other settings and shear flows is given in [25]. The reference DNS
described in Section 2.2.2 was performed using inflow perturbations from LST.
The subject of this section is to compare this case with the results of a DNS
using a randomly perturbed inflow. This is done in a domain with equal grid
spacing and domain sizes as in the reference DNS, except for the extension of
the streamwise domain imposed by the larger transition region. The evolution
of the momentum thickness and the resulting growth rate in the streamwise
direction for both simulations are compared with results of physical experi-
ments.

We consider the case where the perturbations at the inflow are random
variables multiplied by a Gaussian function in the normal coordinate to locate
the perturbations near the centerline. Three-dimensionality is introduced by
including a sinusoidal perturbation in the spanwise direction. The perturba-
tions Q imposed at the inflow have the following form:

$$Q(x_2, x_3, t) = \epsilon \, \exp(-x_2^2)\Big(A_{2D} \, \Psi_{2D} \, R_{2D}(t) + A_{3D} \, \Psi_{3D} \, g(\beta \, x_3) \, R_{3D}(t)\Big)$$

with β the spanwise wavenumber from before in order to conserve the spanwise
domain extent and respect the periodicity in the boundary condition. For g we
employ a sine for the u_3 perturbation and a cosine for the remaining variables.
Furthermore, R_{2D} and R_{3D} are random functions according to the following
stochastic differential equation:

$$\frac{dR}{dt}(t) = -\frac{R(t)}{\tau} + \chi(t). \tag{2.22}$$

The time derivative equals a relaxation term and a random part [34]. The
relaxation time, τ, is taken equal to 1.2 which is about ten times the time
step in the middle resolution. Furthermore, $\chi(t)$ is a random function with
a Gaussian distribution with zero mean and unit standard deviation which
is computed at each Runge-Kutta stage. However, the exact relaxation time
and frequency of updating the random function have no direct influence on
the global behaviour of the results further downstream. For all R_{2D} and
R_{3D} components of the perturbations, the random function is computed in-
dependently. These perturbations are added to the (laminar) solution of the
boundary layer equations. The value of the amplitude ϵ is taken equal to 0.2.
The relative amplitudes equal $A_{2D} = 0.0433$ and $A_{3D} = 0.290$. The relative
and total amplitudes of both $2D$ and $3D$ modes correspond to those of the
reference configuration described in Section 2.2.1 when we take into account
that $R(t)$ from (2.22) approximately fluctuates between -3 and 3. Finally, the
values of Ψ_{2D} and Ψ_{3D} depend on the component and are based on the average
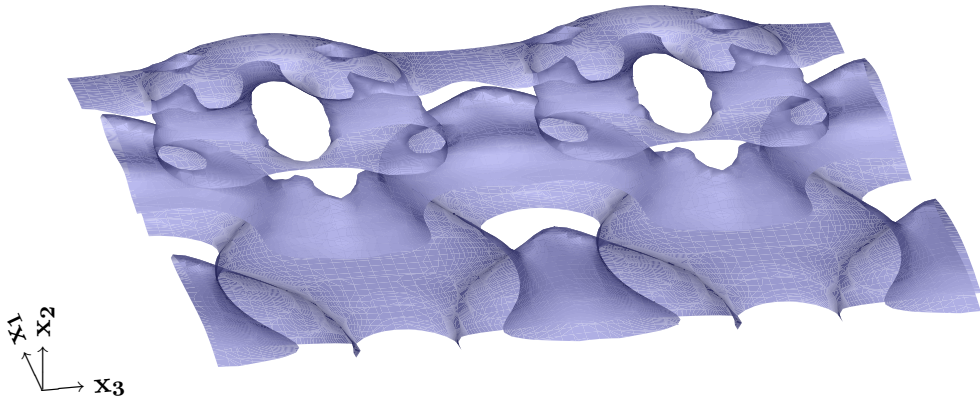
Figure 2.11: Instantaneous spanwise vorticity isosurfaces at value -0.12 from time=552 for the randomly perturbed inflow in the domain $[111, 151] \times [-1, 6] \times [-0.5L_3, 1.5L_3]$.

of the peak values of the corresponding LST eigenfunctions. The differential equations are solved simultaneously during the simulation with the four-stage Runge-Kutta method.

When taking the same streamwise extent of the domain as used with the perturbations from LST, the flow no longer becomes turbulent downstream. Extending the streamwise domain with some 25% resulted in a simulation in which the solution downstream compares well with the results arising from the LST case. In Figure 2.11 the spanwise vorticity for this case is shown at the same time as in Figure 2.3. It is considered for larger values of x_1, however, since the flow remains near the laminar state over a longer streamwise extent and transition arises further downstream compared to the LST case. In fact, translating the LST perturbed simulation downstream over this extra laminar zone of about 70 units, roughly results in the same flow features. The three-dimensional pattern of staggered Λ-vortices resulting in helical pairing is present in this simulation as well. Further downstream this develops into a turbulent state where many small scales are present.

The spectrum of the randomly perturbed DNS is shown in Figure 2.12. One of the main differences with the LST perturbed DNS is that the contribution of the modes in Figure 2.4.a is a factor ten higher for the first quarter of the domain. Further downstream, the levels of the Fourier coefficients saturate at about equal values for both simulations. As a result, the level of turbulence that is reached in both simulations is approximately the same. From Figure 2.12.b it is clear that at the inflow only the mode with index $k_3 = 1$ is present. The behaviour for the larger wavenumbers, similarly as in the LST
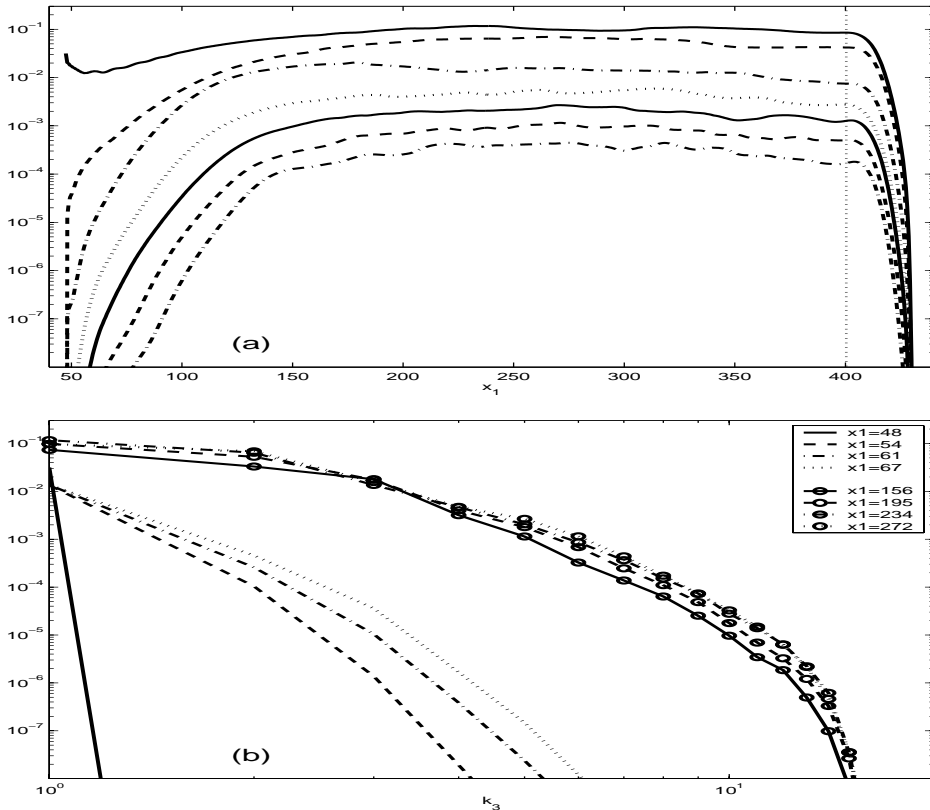
Figure 2.12: Energy spectrum of the DNS with random inflow perturbations. The kinetic energy density $E(x_1, k_3)$ is shown as a function of x_1 for modes $k_3 = 1(—)$ to $7(-\cdot)$ (a) and as a function of k_3 for several equidistant streamwise locations: $x_1 = 48(—)$ to $67(\cdots)$ and (with symbols) $x_1 = 156(—)$ to $272(\cdots)$ (b).

equivalent, does not reach the well-known slope of $-5/3$, probably because the Reynolds number is too low. Besides, in several temporal mixing layer studies it is reported that this $-5/3$ behaviour is hard to reach in the spanwise direction [21, 77]. Finally, we conclude that a collapse of the mode coefficients occurs beyond about $x_1 = 180$. In the rest of this section we show the impact of the change in inflow perturbations on a statistical variable.

In Figure 2.13 the momentum thickness, averaged over 125 T_F and the spanwise direction, is plotted as a function of the streamwise coordinate for both inflow perturbations. The computed thicknesses can be compared with the thickness of the laminar field which is proportional to the square root of the streamwise coordinate. Both DNS momentum thicknesses in Figure 2.13 appear in good approximation to be linear functions of the streamwise coor-
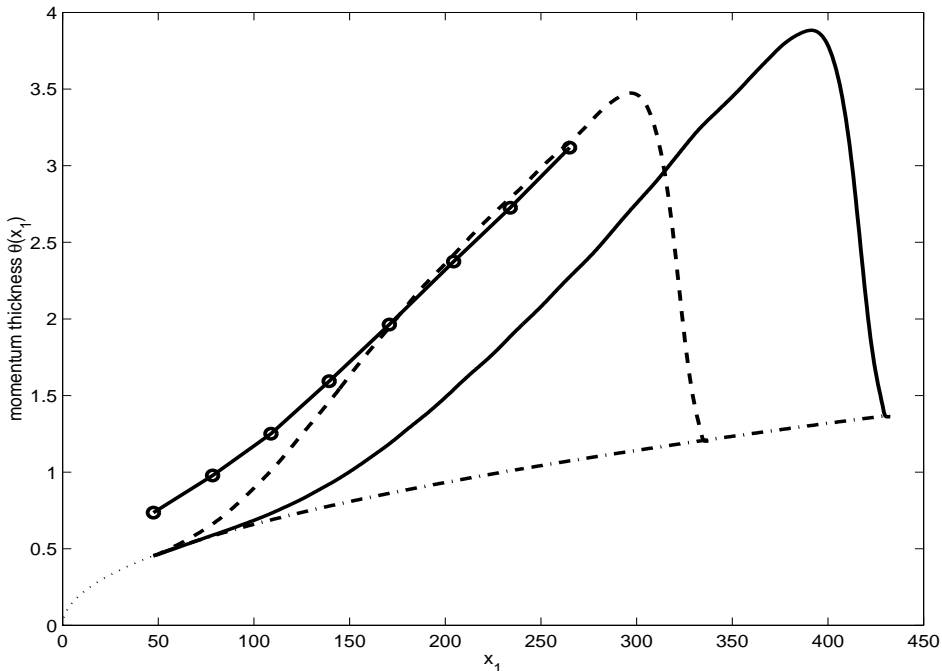
Figure 2.13: Momentum thickness θ as a function of x_1 for the DNS with random (—) and LST (−−) inflow perturbations. Also the development of the steady laminar mixing layer (−·) and the experiment of Oster $e.a.$ [67] is included (o).

dinate in a large part of the domain. Therefore this variable is suitable in the study of self-similarity of the flow in the turbulent regime where it can be used for the scaling of the normal coordinate when studying, $e.g.$, the Reynolds stress tensor. For the random inflow DNS, some extra streamwise distance is required to reach transition and allow the most unstable modes to arise from the random noise imposed at the inflow. The shorter streamwise distance, required for the LST inflow DNS results to exhibit linear growth, supports the spectrum findings that in the first part of the domain the signal contains more modes than for the random inflow DNS. Finally we remark that for both simulations the collapse of the mode coefficients from the spanwise Fourier spectrum globally corresponds to the streamwise location beyond which the momentum thickness develops linearly. This is the case from $x_1 = 120$ for the LST perturbed inflow and from $x_1 = 180$ for the randomly perturbed inflow.

For the approximation of the growth rate $\alpha = d\theta/dx_1$ we use the method of least squares fit in the appropriate part of the domain. Other alternatives are available and give rise to the same conclusions. The estimation of α depends slightly on the location and length of the streamwise domain used for its determination. The growth rates arising from the momentum thicknesses

of the two different inflow perturbations both equal 0.014. At this level of accuracy for α, the precise selection of the region from which this slope is computed is somewhat sensitive especially for the LST perturbed inflow [24]. The behaviour of the momentum thickness of the randomly perturbed inflow approaches linearity better. A measure for this deviation from linearity is the *rms* value between the momentum thickness and the linear slope. The value for the LST inflow DNS is a factor two larger than the random inflow DNS.

Finally, we compare the growth rate with physical experiments. From [29], for incompressible shear layers with equal free-stream densities, the momentum thickness growth rate was found to be in a range that for the present free-stream velocity ratio amounts to [0.009, 0.017]. A factor four was used to convert vorticity thickness in momentum thickness as suggested in [77]. The value for the growth rate computed here can be compared with incompressible results and falls well in this range. This is illustrated in Figure 2.13 where we included results of an incompressible mixing layer experiment which is one of the few experimental studies that show the momentum thickness evolution [67]. The length scale is adjusted in order to fit this result in the dimensions of the present computational domain. We emphasize, however, that this adaptation does not affect the growth rate.

2.4   Conclusions

In this chapter we have presented DNSs for a spatially developing three-dimensional mixing layer. The sensitivity of the DNS is considered with respect to grid resolution, length of time-averaging, boundary locations of the computational domain and inflow perturbations. The DNS results of three different resolutions displayed that the coarse DNS already gives a reliable impression of the momentum thickness and the resulting growth rate. The middle resolution gives a reliable impression of, *e.g.*, the components of the Reynolds stress tensor and is therefore suitable to study self-similarity of the mixing layer. At least the fine resolution is needed to describe the instantaneous quantities accurately.

Subsequently we focused on the time-averaging intervals and concluded that already early in the DNS the momentum thickness was predicted properly but the total time of the current DNS was needed for an accurate determination of the Reynolds stress tensor. Also the results turned out to be insensitive enough with respect to variations in the buffer length and the size of the domain. Finally, a similar growth rate was found for the LST and randomly perturbed DNS. So in further studies this may contribute to the discussion of the existence of a single self-similarity state. Summarizing, in this chapter we have presented a robust DNS that generated a database. This database

can next be used for, *e.g.*, the validation of model assumptions in numerical techniques other than DNS. First, similarity features are considered in the next chapter. These involve the self-similar development of several quantities and the classification of the terms in the turbulence kinetic energy equation.

Chapter 3

Analysis of statistical results

In this chapter we complement the experimental investigations of the turbulent mixing layer with an analysis of the statistical DNS data as described in the previous chapter. A numerical study has the advantage of allowing a precise control of inflow conditions with which, *e.g.*, the strong persistence can be examined. The results described in Chapter 2 are explored regarding the presence of self-similarity as well as the collection of energy budgets as they arise in the turbulence kinetic energy equation. The first motivation is a further validation of the DNS. The database of a turbulent shear flow simulation is supposed to display self-similarity. Moreover, the total of the energy budgets should be conserved. A second motivation involves both properties as such. A quantity is considered to be self-similar when it can be described by only one profile. Self-similarity therefore implies a considerable collapse of the data. Furthermore, the energy budgets can be used to test some RaNS assumptions as will be done in the next chapter.

Turbulent mixing layers are known to develop into a self-similar state sufficiently far downstream of the splitter plate that is used to generate them. There have been several experimental investigations of the statistics of self-similar turbulent mixing layers [9, 41, 108]. A large variation in the experimental results is observed even for the most basic statistical quantities, like the normalized growth rate and the turbulence intensities. In ref. [87] an historical overview of the growth rate determination for physical experiments is given. In much of these studies, it was found that far downstream the growth rate and profiles of the Reynolds stress tensor change in response to variations in the inflow conditions. In ref. [27] it is suggested that the reason for these, and other discrepancies in experimental observations, may be that details of upstream conditions are very persistent in turbulent mixing layers.

Neither physical experiments nor numerical computations have been able to definitively settle the issue about the existence of multiple similarity states.

Regarding the fact that details of the initial conditions have been observed to persist very far downstream, it is suggested in ref. [77] that the same self-similar state could be achieved if simulations were allowed to evolve for longer times (temporal setting) or larger boxes (spatial setting). Mixing layers are not unique in exhibiting such persistent strong dependence on inflow conditions. Other numerical studies involve the similarity of time-evolving plane wakes [40, 66], where a similar ongoing discussion regarding the existence of multiple similarity states takes place. The effect of initial conditions on the development of temporally evolving planar three-dimensional incompressible wakes is studied in ref. [88]. A related numerical investigation on the effect of the inflow conditions on the self-similar region of a round jet is presented in ref. [13].

The extensive database that arises from the DNS can also be used for RaNS modeling purposes. In the second part of this chapter, all terms of the turbulence kinetic energy equation are calculated in order to see which terms are important. Also some terms satisfy the constraints of self-similarity. Furthermore, we consider which terms vanish after integration in the normal direction. In the next chapter this analysis is extended to the eddy viscosity and gradient-diffusion hypotheses. Finally we note that, if not mentioned otherwise, all results presented in this chapter are based on the longest time sample (from $T_0 = 25 \ T_F$ until $T = 150 \ T_F$, with T_0 and T_F defined in Section 2.2.1).

The chapter is organized as follows. In Section 3.1 we consider several quantities like the growth rate, mean streamwise velocity and components of the Reynolds stress tensor that may show features of self-similarity. These are also compared with results of other numerical studies and physical experiments. Section 3.2 is used for the presentation and discussion of the budgets from the turbulence kinetic energy equation. We summarize our findings in Section 3.3.

3.1   Self-similarity

In this section we describe the self-similar development of the mixing layer in more detail. The similarity profile of several quantities is studied. Results of physical experiments regarding the growth rate, averaged streamwise momentum density and width and peak of profiles of the Reynolds stress tensor components are compared with the present findings.

We already mentioned that developed turbulent mixing layers evolve self-similarly, with a linearly increasing thickness as a function of the streamwise coordinate. By scaling with the local thickness and the difference in the free-stream velocities, the profiles of several quantities at different downstream

locations (or at different times in the temporally evolving flow) approximately collapse onto a single curve. In what follows, the results of the present DNS are explored for evidence of such self-similar evolution. We need a similarity variable that is a measure for the layer thickness. This variable is subsequently used for the scaling of the profiles of various quantities, *e.g.*, the time-averaged velocity or components of the Reynolds stress tensor. As reported in [77] a suitable similarity variable is the momentum thickness.

A variable ϕ is said to be self-similar beyond a streamwise location $\widehat{x}_1$ if it depends only on a combination of the independent variables rather than on each independent variable individually. Because of the bending down of the mixing layer, that was already mentioned in Chapter 1, usually an extra translation variable is employed. Self-similarity in a set of profiles can be written as:

$$\phi(x_1, x_2) = f(\eta(x_1, x_2)) \quad x_1 > \widehat{x}_1, \tag{3.1}$$

with

$$\eta(x_1, x_2) = (x_2 - x_2^c)/\theta(x_1).$$

Here, θ is the momentum thickness, η is a similarity variable and x_2^c is chosen such that the mean streamwise velocity equals U_c at $\eta = 0$ [41, 60, 67].

In [61] the most important characteristics for self-similarity in fully-developed flow were collected for the streamwise development of mixing layers. A first property is a linear growth of a characteristic thickness with respect to downstream distance. Furthermore, self-similarity of the mean velocity profiles is needed. Finally, all turbulence intensity profiles should also satisfy this similarity constraint. The latter requirement, among others, implies that the peak values should remain constant. Note that a linear growth of the mixing layer is only one of the conditions for the achievement of self-similarity. In most configurations, the profiles of the turbulence intensities are more sensitive in determining self-similarity. Following [95], the velocity difference across the layer is chosen as the normalizing velocity and this is used for, *e.g.*, the scaling of the Reynolds stress tensor. In the rest of this section, the present mixing layer is considered for the presence of self-similar behaviour.

The linear growth of the momentum thickness as shown in Figure 2.7.b arises beyond $\widehat{x}_1 \approx 120$. In Figure 3.1.a we compare the averaged streamwise velocity at several downstream locations. So, $\tilde{u}_1(x_1, x_2)$ is plotted as a function of $\eta = (x_2 - x_2^c)/\theta(x_1)$ for various values of x_1. Except for the first streamwise location, the maximum deviation in the figure is 1%. The average of these profiles in the self-similar region is also compared with other experimental [41, 67] and numerical studies [77]. The study in [77] deals with the temporal incompressible mixing layer. The physical experiment from [41]
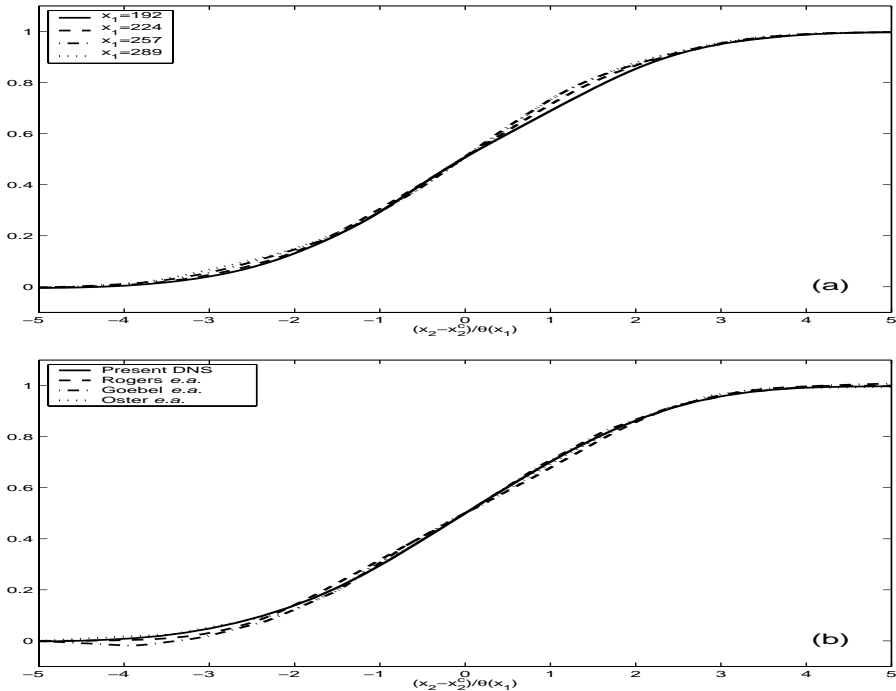
Figure 3.1: Similarity profiles of $(\tilde{u}_1 - U_2)/\Delta U$ from several streamwise locations as a function of $\eta = (x_2 - x_2^c)/\theta(x_1)$ in the present DNS (a) and compared with other studies [77, 41, 67] (b).

is done at the same convective Mach number as in the present case. Moreover, we include the results of an incompressible experiment [67] which is one of the few experimental studies where the results are presented in terms of the momentum thickness. So, it can be compared directly with the results from [77] and the present study. From Figure 3.1.b it is clear that the present streamwise momentum density profile corresponds to results of other studies regarding the slope around the center of the mixing layer. Similarly as for the momentum thickness in Figure 2.13, the deviation with the experiment from Oster *et al.* [67] is small (at most 1%).

However, the collapse of the scaled mean profiles is not a sensitive indicator of self-similarity [41, 61]. Therefore we consider the streamwise development of the streamwise and normal turbulence intensity profiles as shown in Figure 3.2. It is clear that the width of the profile increases with downstream distance. Two isolines are included as well to illustrate self-similar behaviour far downstream resulting in linear dependence on the streamwise coordinate. In order to compare the width and peaks of the stress components R_{11} with the normal coordinate normalized by the momentum thickness is displayed in Figure 3.3.
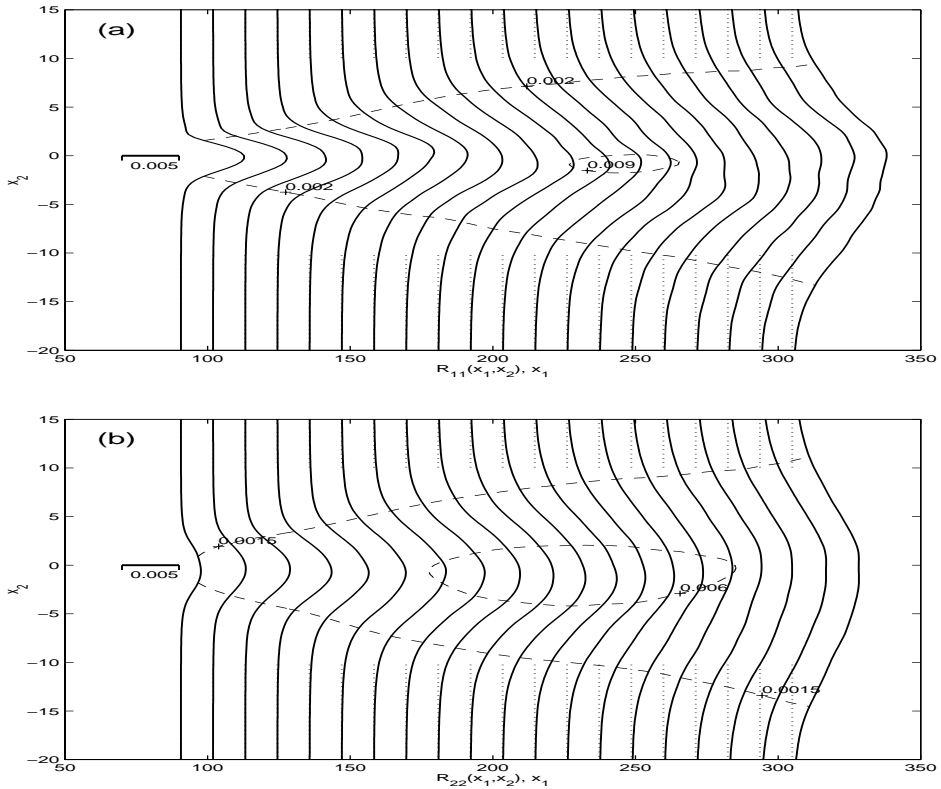
Figure 3.2: Streamwise development of the turbulence intensities R_{11} (a) and R_{22} (b) (—), isolines at 0.002 and 0.009 (a) and 0.0015 and 0.006 (b) (−−) and the level of zero ($\cdots$).
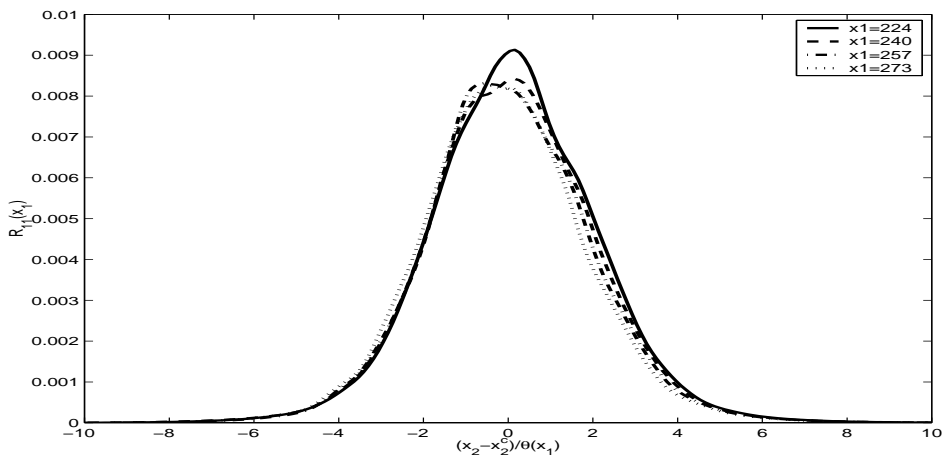

Figure 3.3: Similarity profiles of R_{11} from several streamwise locations as a function of $(x_2 - x_2^c)/\theta(x_1)$ for the fine DNS with LST inflow perturbations.

The scaled width of the profiles is approximately the same at all streamwise locations. Except for the first streamwise location, the maximum deviation in the figure is 3%. Summarizing, the momentum thickness θ displayed a linear growth beyond $\widehat{x}_1 \approx 120$. This value approximately equals 224 for the averaged streamwise velocity $\tilde{u}_1$ and 240 for the streamwise turbulence intensity R_{11}.

Similarly as for the sensitivity studies regarding resolution and averaging time in the previous chapter, the most sensitive part of the profile becoming self-similar is the value of the peak. The streamwise development of the peak values of the Reynolds stress tensor is collected in Figure 3.4. Here, results are shown of the middle-resolution DNS (see Table 2.2) with LST perturbations as well as with random perturbations at inflow. The fine-resolution DNS data are close to the middle-grid results as illustrated in Figure 2.7 for R_{11}. As is clear from the streamwise evolution of the peak value in all components of the Reynolds stress tensor for the LST perturbed DNS, the peak value in the region after the inflow is higher than the asymptotic level attained as x_1 becomes large. This is reported also in other studies of temporal DNS [3] and experiments [9] of the mixing layer. The peak value of the Reynolds stress, $\overline{u_1' u_2'}$, from the random inflow DNS approaches a constant level only far downstream.

The peak values for the fine-grid DNS with LST inflow perturbations and results of other studies are summarized in Table 3.1. Also some incompressible results that contain the spanwise turbulence intensity are collected [9, 44]. We focus on the experimental results that are initiated with a laminar boundary layer and ignore those generated from a turbulent boundary layer. We recall
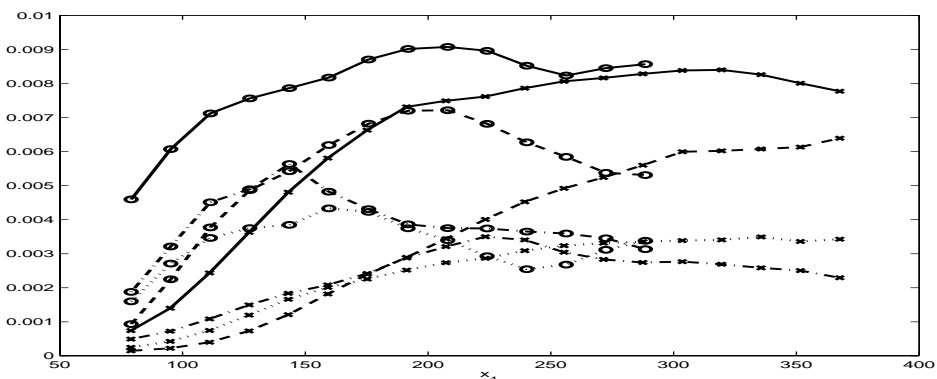

Figure 3.4: Streamwise development of the peak in velocity fluctuations for all components of the Reynolds stress tensor: $R_{11}(—)$, $R_{22}(--)$, $R_{33}(-\cdot)$ and $-R_{12}(\cdots)$ for the DNS results of LST (o) and random (x) perturbations at the inflow boundary.

	α_n	$u_1'/\Delta U$	$u_2'/\Delta U$	$u_3'/\Delta U$	$u_1'u_2'/\Delta U^2$
DNS $(M_c = 0.2)$	0.021	0.19	0.15	0.12	-0.012
Rogers $e.a.$ (incompr.)	0.014	0.16	0.13	0.15	-0.010
Bell $e.a.$ (incompr.)	0.022	0.18	0.13	0.15	-0.012
Goebel $e.a.$ $(M_c = 0.2)$	0.019	0.22	0.15		-0.017
Huang $e.a.$ (incompr.)	0.028	0.19		0.16	-0.011
Oster $e.a.$ (incompr.)	0.020	0.19			

Table 3.1: Normalized momentum thickness growth rates and peak values of components of the Reynolds stress tensor for the present DNS, the temporal DNS of [77] and experimental studies [9, 41, 44, 67].

that u_i' refers to $\sqrt{R_{ii}} = (\overline{u_i'u_i'})^{1/2}$ for the incompressible and to $(\overline{\rho u_i''u_i''}/\bar{\rho})^{1/2}$ for the compressible setting. Furthermore the normalized growth rate is introduced which can be used for direct comparison of spatial configurations. It is denoted by α_n and defined as:

$$\alpha_n = d\theta/dx_1 \cdot U_c/\Delta U$$
$$= d\theta/dx_1 \cdot (1+r)/(2(1-r)),$$

where r equals the ratio of free-stream velocities:

$$r = U_2/U_1.$$

The equivalent growth rate for the temporal setting follows from relation (2.16) and equals $(1/\Delta U)\ d\theta/dt$. The normalized growth rate equals 0.021 for the present simulation and is in the range of findings from several studies, summarized in [77] as $[0.014, 0.025]$.[1]

From the table we observe that the peak value in the streamwise turbulence intensity $R_{11} = \overline{u_1'u_1'}$, normal turbulence intensity $R_{22} = \overline{u_2'u_2'}$ and shear stress $R_{12} = \overline{u_1'u_2'}$ of the present DNS is in the range of peak values reported in other studies. The spanwise turbulence intensity $R_{33} = \overline{u_3'u_3'}$ turns out to be too low compared to other studies. This may be due to the fact that the spanwise domain covers only one fundamental wavelength. In a numerical study of an incompressible spatially-growing mixing layer [21], it is found that a wider spanwise domain results in a lower peak for $\overline{u_2'u_2'}$ and a higher

---

[1]Note the adaptation: $[0.014, 0.025]$ instead of $[0.014, 0.022]$ from [77]. This interval is based on the collection of experimental growth rate values in [29] with respect to $d\delta/dx_1(1+r)/(1-r) : [0.25, 0.45]$. This thickness is rewritten to the vorticity thickness with a factor 2 as suggested in [29] and next to the momentum thickness growth rate with a factor 4.44 as suggested in [77]. Finally an extra factor 2 is needed in the definition of α_n. This results in an interval of $[0.014, 0.025]$ for α_n.

peak for $\overline{u_3' u_3'}$ which supports this conjecture. The large-domain calculations from [55] display higher fluctuation levels than the present small-box ones.

An empirical relation that couples the maximum shear stress and the self-similar growth rate can be written as [6, 60, 95]:

$$-\overline{u_1' u_2'}_{max}/\Delta U^2 = 0.626\,\alpha_n. \qquad (3.2)$$

For the present results, the left-hand side equals 0.012 and is close to the right-hand side value of 0.013. So, although the mixing layer may not have been fully developed in terms of R_{12}, its value in Table 3.1 already satisfies this relation. Furthermore, we remark from Figure 2.13 that the momentum thickness generated with the LST inflow displays a slight increase of the growth rate around $x_1 = 150$. This corresponds to a maximum level of the R_{12} peak in Figure 3.4. On the other hand, the streamwise development of the R_{12} peak is more constant for the random inflow DNS. This supports the fact that the corresponding momentum thickness growth is closer to linearity.

In Figure 3.5 the profiles of all components of the Reynolds stress tensor are collected and compared with the studies displayed in Table 3.1. The normalized profiles are averaged in the self-similar region in order to reach the best estimation. For the present DNS in Figure 3.5.a the profile of the streamwise turbulence intensity around the peak is close to the experimental result from [67]. For the peak values in Table 3.1 we concluded that differences in the peak values compared to experiments may be due to the extent of the spanwise domain. So, similarly as for the growth rate, the 'minimal mixing layer' configuration may be a restrictive factor in the simulations. Note that the turbulence intensities at the upper and lower boundaries do not equal zero for all components. Since the profiles decrease in a smooth sense, this is assumed to be a numerical effect that vanishes when the height of the computational domain is enlarged. This conjecture is based on the findings from Section 2.3.3.

3.2   Analysis of energy budgets

In this section we focus on the turbulence kinetic energy equation. This equation describes the transfer of energy which mainly flows from large to small scales. The turbulence kinetic energy can be used to specify the eddy viscosity and thus model the Reynolds stress tensor. We start with the turbulence kinetic energy equation. Each of the terms in this equation is next evaluated in order to identify the importance of all terms separately. Finally we show the sensitivity of the results due to changes in the grid resolution and the length of the time-averaging. Similarly as mentioned in Section 3.1, all results are normalized by ΔU and $\theta(x_1)$ which corresponds to the incompressible setting
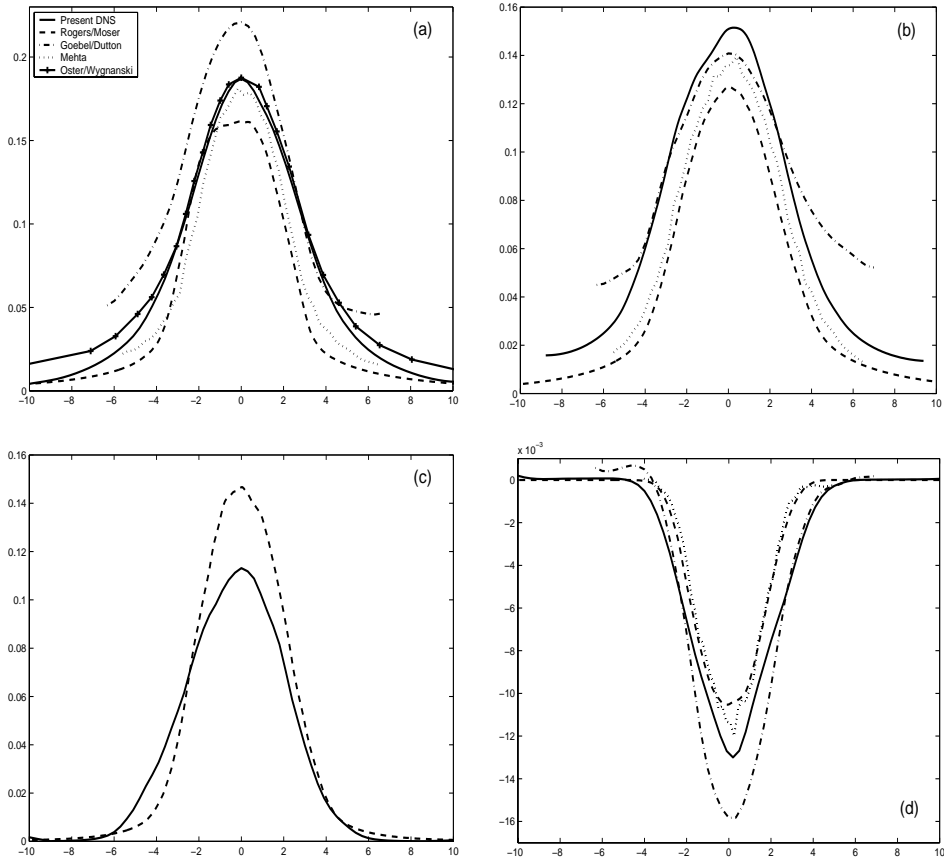
Figure 3.5: Components of the normalized turbulence intensities $R_{ii}^{1/2}/\Delta U$ (i=1-3;a-c) and Reynolds stress $R_{12}/\Delta U^2$ (d) as a function of the normal coordinate normalized with the momentum thickness and centered around the peak value, $\eta = (x_2 - x_2^c)/\theta(x_1)$.

of ref. [77]. An extra normalization ρ^* for the density is needed in the compressible situation. For ρ^* we take the upper free-stream density, which is similar to the scaling of the temporal mixing layer study in [104].

The present results are compared with a temporal mixing layer study at the same convective Mach number [104]. We also consider the incompressible temporal mixing layer DNS study described in [77]. Other studies of the turbulence kinetic energy budgets of the incompressible mixing layer are the experiments described in [108]. Numerical studies for incompressible applications other than the incompressible mixing layer also show that DNS can be helpful to support modeling in RaNS [2, 43, 59, 76]. The findings from these studies are compared with the present mixing layer results.

3.2.1   Turbulence kinetic energy equation

An overview of studies of the Reynolds stress closures of incompressible turbulent flows is given in [86]. Already for some years, in particular the compressible setting of the turbulence kinetic energy equation is extensively analysed and modeled [81, 85]. We use the compressible formulation of the turbulence kinetic energy equation as given in refs. [12, 48]:

$$\partial_t(\bar{\rho}k) + T_t = P + D + P_d - \bar{\rho}\,\epsilon, \tag{3.3}$$

with

$$
\begin{aligned}
T_t &= \partial_j(\bar{\rho}k\,\tilde{u}_j), \\
P &= -\overline{\rho u_i'' u_j''}\,\partial_j\widetilde{u}_i, \\
D &= D_t + D_p + D_v, \\
P_d &= \overline{p\,\partial_j u_j''}, \\
\bar{\rho}\,\epsilon &= \overline{\sigma_{ij}\,\partial_j u_i''},
\end{aligned}
$$

where D is split into a triple correlation, pressure and viscous term:

$$
\begin{aligned}
D_t &= -1/2\,\partial_j\overline{\rho u_i'' u_i'' u_j''}, \\
D_p &= -\partial_j\overline{p u_j''}, \\
D_v &= \partial_j\overline{u_i''\sigma_{ij}}.
\end{aligned}
$$

It is stressed that the bar operator is defined as in (2.8) with infinitely long time-averaging and is approximated by the finite-time equivalent. From Section 2.1.1 we recall that $u_i'' = u_i - \widetilde{u}_i$. Furthermore, k denotes the turbulence kinetic energy per unit mass and is defined as:

$$\bar{\rho}k \equiv \frac{1}{2}\overline{\rho u_i'' u_i''}. \tag{3.4}$$

The various terms appearing in (3.3) account for changes in the turbulence kinetic energy of the mixing layer. Furthermore, $T_t \approx \tilde{u}_j\partial_j(\bar{\rho}k)$ since $\partial_j\tilde{u}_j \approx 0$ [107]. As a result, the left-hand side of (3.3) may be considered as the material derivative of $\bar{\rho}k$ [107]. It gives the rate of change of $\bar{\rho}k$ following the mean flow, with T_t the part that represents the convective motion. The time derivative $\partial_t(\bar{\rho}k)$ equals zero when it is based on a infinitely long time interval of a spatially developing flow. In the rest of this thesis it is neglected. The remaining term on the left-hand side is the turbulent transport, denoted as T_t.

    The conventional description that is traditionally used for each of the terms on the right-hand side of (3.3) is given in Table 3.2. The production P represents the rate at which kinetic energy is transferred from the mean flow to the

Term	Description
P	Production
D	Diffusion:
	D_t Turbulent Diffusion
	D_p Pressure Diffusion
	D_v Viscous Diffusion
P_d	Pressure-dilatation
$\bar{\rho}\,\epsilon$	Dissipation

Table 3.2: Terms in the turbulence kinetic energy equation.

small scales. Rewritten as $-\overline{\rho u_i'' u_j''} S_{ij}(\tilde{\mathbf{u}})/2$, this term is seen to be the rate at which work is done by the mean strain rate against the turbulent stresses [107]. The major contribution of production for the mixing layer is from $-\overline{\rho u_1'' u_2''}\,\partial_2 \tilde{u}_1$ which is known to be positive for the mixing layer (see Section 3.1). The diffusion D is commonly split in three terms, $D = D_t + D_p + D_v$, representing turbulent diffusion, pressure diffusion and viscous diffusion respectively.[2] The triple velocity correlation is often called turbulent transport and can be regarded as the rate at which turbulence energy is transported through the fluid by turbulent fluctuations. The turbulent transport resulting from correlation of pressure and velocity fluctuations is contained in the pressure diffusion term. The viscous diffusion quantifies the diffusion of turbulence energy caused by molecular transport processes in the flow and is sometimes called molecular diffusion. The pressure-dilatation P_d only arises in compressible flow since conservation of mass yields $\partial_i u_i'' = 0$ for incompressible flow. The remaining term, $\bar{\rho}\epsilon$, is responsible for the decrease in turbulence kinetic energy due to viscous dissipation. It is the rate at which turbulence kinetic energy is converted into thermal energy. Finally, we define the balance, E:

$$E = P + D + P_d - \bar{\rho}\,\epsilon - T_t. \tag{3.5}$$

The fact that the balance is not exactly equal to zero is a result of the finite interval of time sampling as well as the presence of errors of numerical origin. The balance E only becomes exactly zero for an infinitely small grid distance and infinitely long time-sampling. Longer time-averaging is needed for the balance to get closer to zero. The amount of computer time that is needed for a better convergence of the results is beyond the limit of this study.

Similarly as before, the filtering in the spatial setting should be performed over x_3 and t (see definition (2.8) and its finite time equivalent (2.20)). Due to memory restrictions this can only be done during the DNS itself. Details

---

[2]Sometimes the first two $(D_t + D_p)$ are referred to as transport [94].

regarding the computation of the terms in the kinetic energy equation are given in Appendix A. Basic elements are defined from which all terms in the equation can be build. This results in a clear and simple implementation of the energy budgets in the DNS code. Next, we evaluate the energy budgets.

3.2.2   Energy budgets

In this section we first classify the terms in the turbulence kinetic energy equation according to their peak values at three streamwise locations. The streamwise development of all terms is described next and shown from the laminar to the turbulent stage at some characteristic values of x_2. Finally we give an impression at a downstream location. Data from DNS in the transitional and turbulent stage can be helpful to test RaNS models. This is especially the case for low Reynolds number corrections of RaNS models.

The peak value of each term in the kinetic energy equation (3.3) is collected at three streamwise locations in the turbulent regime. The results are shown in Table 3.3 where the energy budget terms are ordered from large to small. According to the maximum norm, the terms of major importance are P, D_t, $\bar{\rho}\epsilon$ and P_d. Beyond $x_1 \approx 200$, the normalized viscous diffusion D_v is closer to zero than the balance E.

As a next step, in Figures 3.6.a-c we have collected the normalized energy budgets as a function of the streamwise coordinate for three characteristic values of $x_2/\theta(x_1)$. The profiles at a streamwise location in the turbulent regime are shown in Figure 3.6.d. The viscous diffusion D_v is not included since it cannot be distinguished from zero. We take the same signs as in the definition for the balance E (3.5), so we plot P, D_t, D_p, P_d, $-\bar{\rho}\epsilon$ and $-T_t$.

$\max(|\cdot|)$	x_1		
$(\times 10^{-3})$	225	257	289
P	2.5	2.7	3.4
D_t	1.8	2.3	2.4
$\bar{\rho}\epsilon$	1.6	1.7	1.6
P_d	0.97	1.3	1.2
T_t	0.47	0.56	0.66
D_p	0.32	0.54	0.54
E	0.14	0.19	0.22
D_v	0.10	0.076	0.081

Table 3.3: Maximum over x_2 of the terms in the turbulence kinetic energy equation taken at three streamwise locations and normalized with $(\Delta U)^3/\theta(x_1)$.
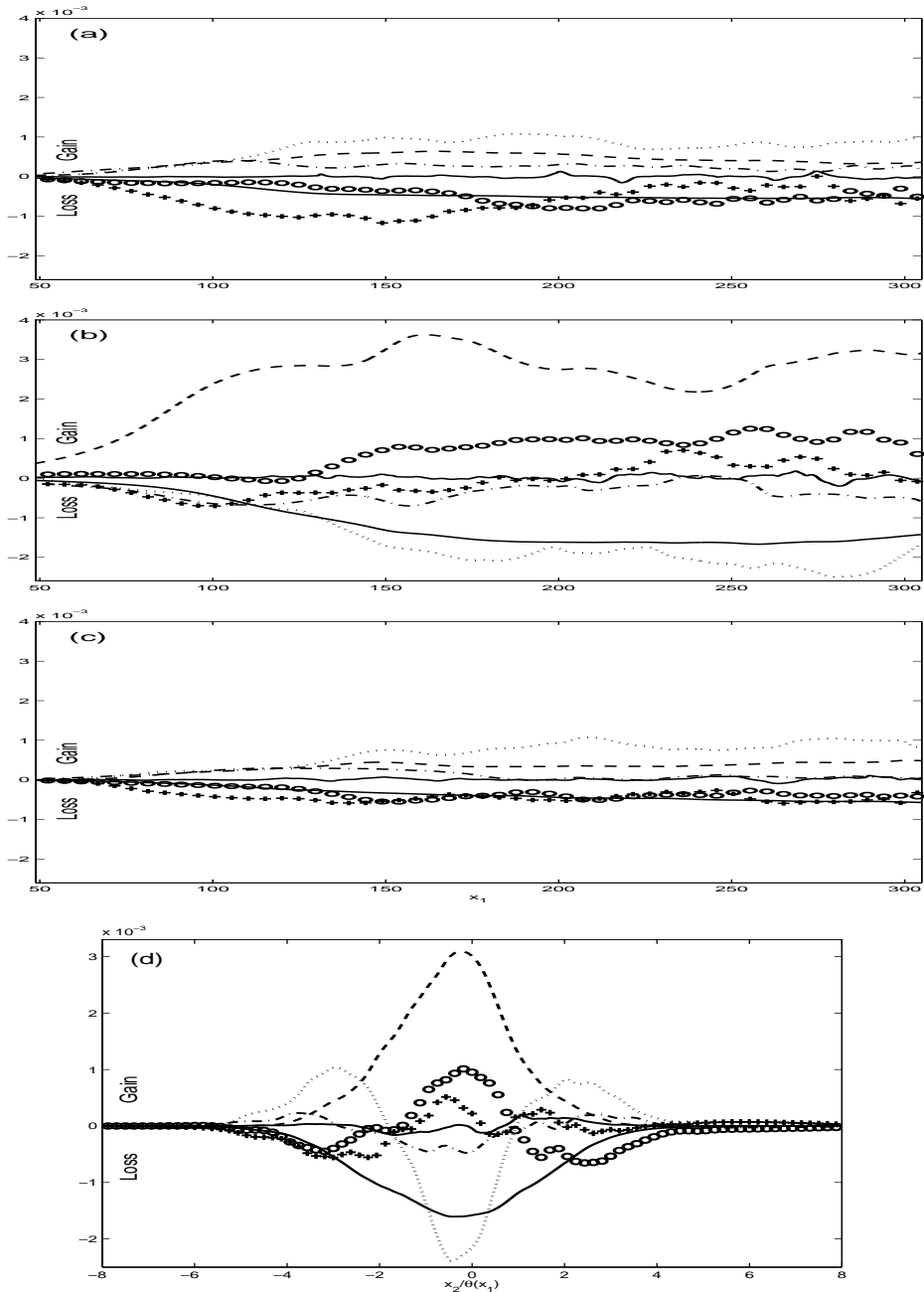
Figure 3.6: Turbulence kinetic energy profiles, normalized with $\Delta U^3/\theta(x_1)$, at $x_2 = 2.2$ (a), -0.4 (b), -3.0 (c) as a function of x_1 and at $x_1 = 275$ as a function of $x_2/\theta(x_1)$ (d). The separate terms are denoted by: $P(--)$, $D_t(\cdots)$, $D_p(-\cdot)$, $P_d(o)$, $-\bar{\rho}\epsilon$(—, negative line), $-T_t(+)$ and E(—, line closest to zero).

We note that the terms can be divided into two groups. The first group consists of terms that are either positive (P), or negative ($-\bar{\rho}\epsilon$). From this perspective, it seems reasonable to start modeling the balance with the production and dissipation only, as suggested in [94]. Next, we have the group of terms where the contribution to the kinetic energy is positive or negative depending on x_2. Some terms are positive on the mixing layer centerline and have negative bumps on either side (P_d, $-T_t$), while others have a negative value at the centerline and positive bumps (D_t, D_p).

We next discuss the profiles from Figure 3.6. Just after the inflow, the production P around the centerline grows significantly. It is balanced by $-T_t$, $-\bar{\rho}\epsilon$, D_t, and D_p, which all still are small but negative. Around the edges of the mixing region, the transport term $-T_t$ decreases while P, D_t and D_p increase as a function of x_1. This corresponds with results of the separation bubble configuration in [2]. In this study, the key balance at the layer edge close after the inflow is between on one hand convection, $-T_t$, which implies a decrease of k, and on the other hand production, P, and triple moment transport, D_t, which tend to increase k. For this inflow area away from the wall respectively center of the mixing layer, the dissipation only plays a role of minor importance. The transport $-T_t$ is negative over the whole domain close after inflow, similarly as in [2]. This is primarily due to $\tilde{u}_1 \partial_1 k$ since k increases rapidly with x_1 during transition. Further downstream it remains negative around the edge of the layer while it gets positive at the mixing layer centerline as well as close to the wall after the reattachement of the bubble.

The pressure-dilatation behaviour, which is typical for compressible turbulence, corresponds to results from [101] in the sense that it is positive around the centerline and negative at both mixing layer edges. In an incompressible setting, the pressure-dilatation equals zero. For the low convective Mach number ($M_c = 0.2$) used in [101] and here, we therefore might expect a small contribution of P_d. This is not the case however, as can be observed from Table 3.3 and Figure 3.6. The normalized P_d profile from [101] even is a factor two larger than the present results. So, in both the temporal and spatial configuration the pressure-dilatation is not negligible.

As mentioned before, the basic assumption in several RaNS modeling approaches is the balance between production and dissipation of kinetic energy. The dissipation profile in Figure 3.6.d is slightly wider than the production profile, similarly as in [77]. This implies that, relative to the production, energy is dissipated in the outer sides of the mixing region. This results in a wide profile of $-T_t$ and thus the material derivative of $\bar{\rho}k$ is positive at the edges. Summarizing, comparison of all terms in the turbulence kinetic energy equation shows that for the present flow all terms, except for the viscous diffusion, should be taken into account. This was already concluded before for spatially developing shear flows other than the mixing layer [2, 43, 59]. Next,

we consider the integrated energy budgets.

In order to study the self-similarity, the contour plot for the dissipation is shown in Figure 3.7. Especially in the outer ranges of the mixing layer, the contour lines are linear. The turbulence kinetic energy also exhibits this tendency to self-similar behaviour as is clear from Figure 3.8. Furthermore, the contour plot demonstrates that $\partial \bar{\rho} k / \partial d x_1$ is positive. Finally we note that the rate of change of $\bar{\rho} k$ is larger in the x_2-direction.
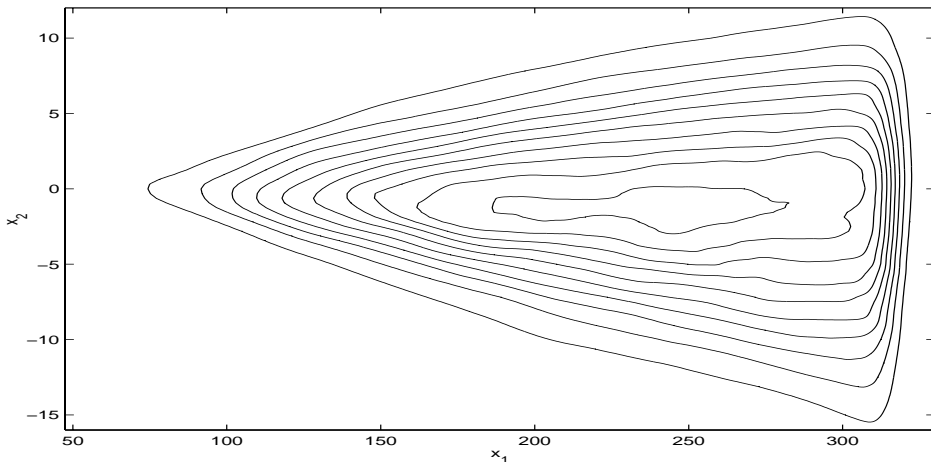
Figure 3.7: Contour lines of the dissipation $\bar{\rho}\epsilon$ normalized with $\Delta U^3/\theta(x_1)$ in the (x_1, x_2)-plane at 10 values equally distributed between 1.6×10^{-4} (on the flanks) and 1.6×10^{-3} (at the centerline).
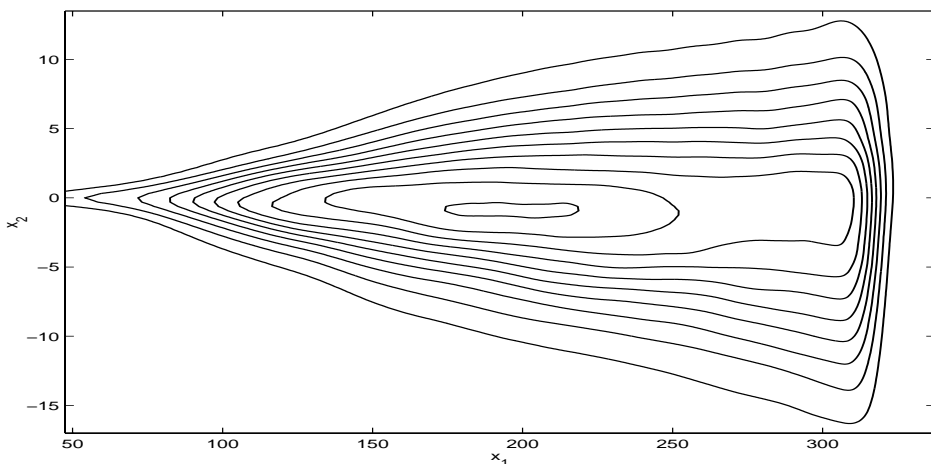

Figure 3.8: Contour lines of $\bar{\rho} k$ in the (x_1, x_2)-plane at 10 values equally distributed between 1×10^{-4} (on the flanks) and 1×10^{-3} (at the centerline).

3.2.3   Integrated energy budgets

In this subsection we study the total contribution of the terms in the turbulence kinetic energy equation at a streamwise location by integrating over x_2. The results are shown in Table 3.4 for the same streamwise locations as in Table 3.3.

Although the turbulent diffusion D_t itself has a large contribution in the turbulence kinetic energy budgets, the turbulent diffusion integral $\int D_t \, dx_2$ is negligible. In fact, the integral of all terms contained in D is small. It is even smaller than the numerical approximation of the (finite time) integral over the balance E itself. The total diffusion integral is small since D is in divergence form and its values at the upper and lower free-stream boundary can be neglected.

Furthermore, $\int T_t \, dx_2$ is more important than $\int P_d \, dx_2$. As shown in Table 3.3 and Figure 3.6, the peak of P_d is about a factor two to three smaller than the production and dissipation. The integrated pressure-dilatation $\int P_d \, dx_2$ is much smaller, however, than the integrated production and dissipation. In the next chapter, the data presented in this and the previous subsection is evaluated with respect to RaNS assumptions.

3.2.4   Sensitivity analysis

We consider the sensitivity of the flow predictions due to changes in the grid resolution and the length of the time-averaging. An extensive sensitivity study of the DNS results has already been discussed in Section 2.3. It is repeated here for some energy budgets that represent combinations of terms that before were only considered separately. This is done in order to verify that the terms

$\int \cdot dx_2$ ($\times 10^{-4}$)	x_1		
	225	257	289
P	87.8	84.2	97.5
$\bar{\rho}\,\epsilon$	69.2	70.6	68.8
T_t	16.3	12.7	32.2
P_d	1.3	2.5	2.7
E	2.5	2.1	-1.3
D_t	-0.75	-0.76	-0.88
D_p	-0.29	-0.39	0.49
D_v	-0.059	-0.085	-0.17

Table 3.4: Integral over x_2 of the terms in the turbulence kinetic energy equation taken at three streamwise locations and normalized with $(\Delta U)^3$.

together do not cause cumulative effects. In Figure 3.9 we have collected the normalized P, $\bar{\rho}\epsilon$ and P_d which are characteristic terms in the turbulence kinetic energy equation. These quantities are evaluated using the DNS results for the three resolutions described in Table 2.2 and are based on the longest time sample (from $T_0 = 25\ T_F$ until $T = 150\ T_F$, with T_0 and T_F defined in Section 2.2.1). It is clear that the middle- and fine-grid results are close. Deviations occur mainly around the centerline. The maximum deviation between the normalized production of the middle and fine grid equals 2×10^{-4} (8%) and this is a factor of two smaller than the maximum deviation between the coarse and fine grid.

The balance E, introduced in (3.5), is defined from all terms in the kinetic energy equation that do not vanish after infinitely long time averaging. The DNS only covers a finite time sample. The DNS result for E quantifies the error that is made when averaging over a finite time interval and computing at a numerical grid. It is found that when a finer grid is used, the DNS results for the balance are closer to zero. The maximum deviation from zero at the same x_1 value as in Figure 3.9 equals 1×10^{-4}, 2×10^{-4} and 6×10^{-4} for the fine, middle and coarse resolution respectively.

Next we vary the length of the interval used for the time-averaging. The normalized fine-grid results are plotted in Figure 3.10 based on the time sample

Figure 3.9: Profiles of P, $-\bar{\rho}\,\epsilon$ and P_d as a function of $x_2/\theta(x_1)$ at $x_1 = 241$, normalized with $\Delta U^3/\theta(x_1)$ and plotted for the coarse $(-\cdot)$, middle $(--)$ and fine $(-)$ resolution DNS (based on the longest time sample available).
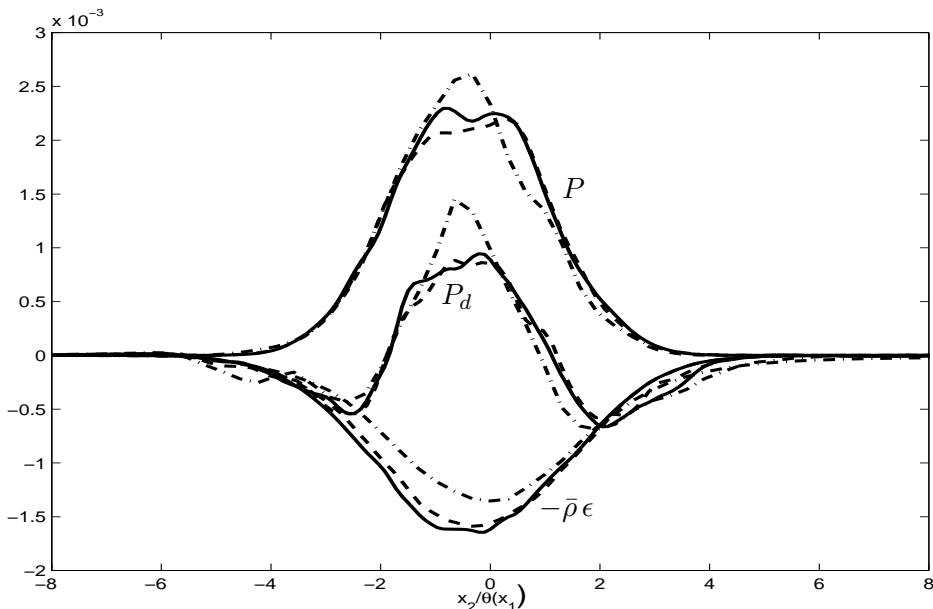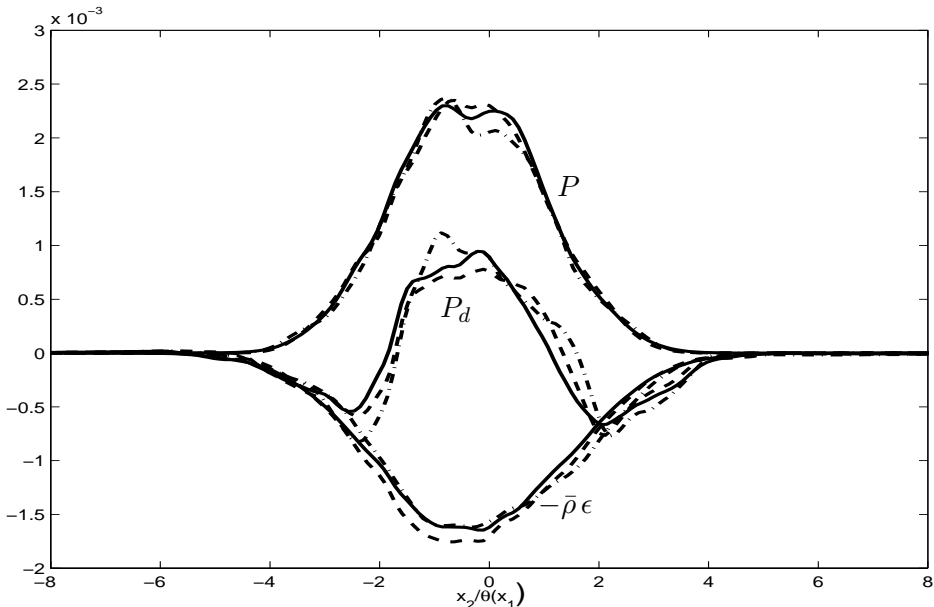
Figure 3.10: Profiles of P, $-\bar{\rho}\,\epsilon$ and P_d as a function of $x_2/\theta(x_1)$ at $x_1 = 241$, normalized with $\Delta U^3/\theta(x_1)$ and averaged over a short $(-\cdot)$, middle $(--)$ and long $(—)$ time interval (from $t = 552 = 25\ T_F$ until $T_1 = 70\ T_F$, $T_2 = 110\ T_F$ and $T_3 = 150\ T_F$ respectively and based on the fine-grid results).

from $T_0 = 25\ T_F$ until times $T_1 = 70\ T_F$, $T_2 = 110\ T_F$ and $T_3 = 150\ T_F$. The maximum deviation between the normalized production for the middle and long time interval at $x_1 = 241$, which is a streamwise location in the turbulent regime, equals 1×10^{-4} (5%). This is a factor of two smaller than the deviation between the short and long time interval. For the normalized balance, E, the maximum deviation from zero equals 1×10^{-4} for the long time interval. This is a factor of two smaller than the equivalent for the middle and short time intervals. Note that already from the shortest time interval the corresponding balance is reasonable since it is one order of magnitude smaller than for example P and $\bar{\rho}\epsilon$.

3.3   Conclusions

The first motivation of this chapter involved a further validation of the DNS based on the statistical results from the previous chapter. The database of a turbulent shear flow simulation should display self-similarity. Moreover, the total of the energy budgets should be conserved. A second motivation involved both properties as such. In the first part of this chapter, we have shown some evidence of self-similarity of the mixing layer. The development lengths showed

that the momentum thickness, already displayed in the previous chapter, becomes self-similar after a short downstream distance, followed by the averaged streamwise momentum density and finally the streamwise turbulence intensity. This order of variables becoming self-similar corresponds to observations from physical experiments. Most profiles in the streamwise development of these properties are close to results of other numerical and experimental studies. They can be used to describe the statistics on all downstream locations in the self-similar region of the DNS.

In the second part of this chapter the contributions to the budgets of the turbulence kinetic energy have been presented. The sensitivity analysis showed that results of the finest-grid DNS that were sampled over the longest time interval available, appear of sufficient accuracy for our purposes. The data can be improved by averaging longer in time with the same resolution, but this is beyond the limit of this study. We have described the development of all terms in the turbulence kinetic energy equation when moving in downstream direction. Except for the viscous diffusion, all terms should be taken into account. After integration over the normal direction, the contribution of the diffusion terms as well as the pressure-dilatation could be neglected. As a result, the integrated dissipation was balanced by the integrated production and transport.

An interesting point for further study is the question how much the single spanwise wavelength constrains the simulation in developing into a three-dimensional numerical turbulent mixing layer, *i.e.*, will a larger spanwise domain result for example in other peak values of the Reynolds stress tensor and a better approximated self-similar behaviour? The results and the work done in [82, 104] also encourage the application of the numerical method to large-eddy simulations. These items will be considered in Chapters 5 and 6.

Chapter 4

Guidance for RaNS modeling by DNS results

The modeling of the Reynolds stress tensor has been a topic of great interest for several decades. This tensor arises in the Navier-Stokes equations after ensemble averaging. For some years, databases from direct numerical simulations of relatively low Reynolds number turbulent flows in simple geometries are available with which individual model assumptions can, in principle, be tested directly. The data can also be used to support further development of these models. The turbulence kinetic energy can be used to specify the eddy viscosity and thus model the Reynolds stress tensor within the gradient hypothesis framework [48].

One of the main ideas in modeling the turbulence kinetic energy equation is the assumption of a balance between production and dissipation [94]. Viscous shear stresses increase the internal energy of the fluid and decrease the kinetic energy of the turbulence. Turbulence needs a continuous supply of energy to make up for these viscous losses. If no energy is supplied, turbulence decays rapidly. In order to keep the system going, a production source is required. In Chapter 3 we already described the development of all terms in the turbulence kinetic energy equation throughout the whole streamwise domain. The terms were classified according to the maximum norm. Comparison showed that for the present results most terms need to be taken into account, *i.e.*, the balance does not consist of production and dissipation only. The classification of the terms changed when they were integrated over the normal direction instead and the integrated production and transport appeared to largely balance the integrated dissipation. The resulting integrated balance is evaluated in more detail in this chapter.

The eddy viscosity assumption is considered, in particular for the standard $k - \epsilon$ model and two low Reynolds number corrections. The best comparison

for the Reynolds stress between the DNS results and the $k - \epsilon$ model can be used to optimize model parameters. Also the diagonal components of the Reynolds stress tensor are evaluated. Finally we consider the gradient-diffusion hypothesis. It is often used in RaNS and relates the turbulent diffusion with the turbulence kinetic energy derivative.

The chapter is organized as follows. In Section 4.1 the Reynolds-averaged equations are given. We introduce the concept of an eddy viscosity that is used to close the RaNS model equations. The DNS results are used for an *a priori* analysis in Section 4.2. All terms of the kinetic energy equation have already been evaluated from the DNS results and interpreted in Chapter 3. This study is continued with the evaluation of three assumptions that are typical for modeling in RaNS. First a balance between production and dissipation is investigated. Also the eddy viscosity assumption is considered and compared with results of the standard $k - \epsilon$ model and two low Reynolds number corrections. Finally, the gradient-diffusion hypothesis is evaluated with the use of the present DNS results. The findings are summarized in Section 4.3.

4.1   Governing equations

In this section we give the equations that are relevant for the study of turbulence kinetic energy budgets. We assume that ensemble averaging can be replaced by averaging over the homogeneous directions (and time). Averaging over the homogeneous coordinates as defined in (2.8) is applied to the Navier-Stokes equations (2.1)-(2.3). This results in a set of steady averaged equations, which are the well-known Reynolds-averaged Navier-Stokes equations. We use the spatial frame of reference, in which only the spanwise direction is homogeneous. In this setting, averaged quantities are independent of time. The averaged continuity and momentum equations are the following:

$$\partial_j(\bar{\rho}\widetilde{u}_j) = 0, \tag{4.1}$$

$$\partial_j(\bar{\rho}\widetilde{u}_i\widetilde{u}_j) + \partial_i\overline{p} - \partial_j\bar{\sigma}_{ij} = -\partial_j(\bar{\rho}R_{ij}) \quad (i = 1, 2), \tag{4.2}$$

with $\bar{\sigma}_{ij} = S_{ij}(\widetilde{\mathbf{u}})/Re$ as defined in (2.5). For the present configuration, the averaged momentum equation in the spanwise direction ($i = 3$) is trivial. In the filtered system of equations (4.1)-(4.2) we have ordered the terms such that the left-hand side is similar to the corresponding terms in the Navier-Stokes equations (2.1)-(2.3) but now applied to the filtered variables $\bar{\rho}$, $\widetilde{u}_j$ and $\overline{p}$.

The filtering of the nonlinear terms gives rise to the right-hand side which requires modeling in order to close the system of equations. The only term in this closure is the Reynolds stress tensor, $R_{ij} = \overline{\rho u_i'' u_j''}/\bar{\rho}$ (see (2.10)). A set of equations for the Reynolds stress tensor can be obtained from the conservation of momentum and mass. These are called the Reynolds stress equations [12,

48] and comprise the turbulence kinetic energy equation which was already introduced in Chapter 2. These equations introduce triple correlations, such as $\overline{\rho u_i'' u_j'' u_k''}$. Additional equations could be derived for these correlations, but would introduce even higher order correlations. The system of equations is not closed. Therefore it is necessary to introduce models either for the terms in the Reynolds stress equation or for the Reynolds stress tensor itself. An extensive overview of several models that are used in RaNS is given in [107].

The earliest model is due to Boussinesq [15] and is still widely used. Here, in analogy with the description of viscous stresses in a laminar flow (2.5), the Reynolds stress tensor is assumed to be proportional to the strain rate tensor applied to the Favre-filtered velocity:

$$-\overline{\rho u_i'' u_j''} = \mu_t \, S_{ij}(\tilde{\mathbf{u}}) - 2/3 \, \bar{\rho} k \, \delta_{ij}. \tag{4.3}$$

The assumption introduces the eddy viscosity μ_t and the turbulent kinetic energy k, defined in (3.4), that need to be determined.

The unknown eddy viscosity μ_t has dimensions $\mu_t \sim density \times velocity \times length$. A fundamental assumption in the development of turbulence models for RaNS is *Morkovin's hypothesis* [30],

$$\sqrt{\overline{\rho'^2}} \ll \bar{\rho},$$

which assumes that the effect of density fluctuations ρ' on the turbulence structure are unimportant. For the present case, this hypothesis is valid within 1%. Therefore it is generally assumed that the density can be taken to be the local mean density $\bar{\rho}$. Thus the eddy viscosity is expressed as

$$\mu_t \sim \bar{\rho} \, v \, l, \tag{4.4}$$

where v and l are the 'local' velocity and length scales that are supposed to describe the turbulence [85]. The problem is now reduced to specifying v and l. Several popular models exist and they are categorized according to the way they specify v and l. Two-equation models are commonly used [85]. Almost all two-equation models employ the turbulence kinetic energy to characterize the velocity scale but there are many different approaches for the characteristic length scale l.

One of the most popular two-equation models is the $k - \epsilon$ model from [47], and usually referred to as the 'standard' $k - \epsilon$ model. Here, ϵ denotes the dissipation per unit mass, as already defined in (3.3). The model uses the following expressions for the characteristic velocity and length scale:

$$v = \sqrt{k},$$
$$l = k^{3/2}/\epsilon.$$

Now the eddy viscosity is expressed in terms of quantities that usually are known from the DNS results:

$$\mu_t = C_\mu \, \bar\rho \, k^2/\epsilon, \tag{4.5}$$

using (4.4). The model constant C_μ is usually set to 0.09.

The $k - \epsilon$ model, like many others, has coefficients that are tuned for high-Reynolds number applications. Many researchers have attempted to formulate viscous corrections for the $k - \epsilon$ model. These so-called low Reynolds number (LRN) corrections usually are formulated for incompressible shear layers [52, 76, 107]. The idea is to introduce a damping function f_μ that damps the near wall model approximation that usually overpredicts the eddy viscosity. The variant described in [52] is adapted to the compressible formulation:

$$\mu_t = \bar\rho\nu_t = C_\mu \, f_\mu \, \bar\rho k^2/\epsilon^*,$$

with

$$\epsilon^* = \epsilon - \epsilon_0,$$
$$\bar\rho\epsilon_0 = \frac{2}{\bar\rho \, Re}\big(\partial_2 \sqrt{\bar\rho k}\big)^2,$$
$$f_\mu = \exp(-3.4/(1 + Re_T/50)^2),$$
$$Re_T = \frac{\bar\rho k^2 \, Re}{\epsilon^*}.$$

It is clear that for large Reynolds numbers Re, Re_T becomes large, f_μ approaches one and ϵ_0 zero. As a result, the low-Reynolds number correction results are approximately equal to results of the standard $k - \epsilon$ model if $Re \gg 1$. For moderate Reynolds numbers, the contribution of ϵ_0 to ϵ cannot be ignored. Combined with a steep kinetic energy gradient in normal direction, ϵ_0 may approach ϵ and result in a large value of μ_t.

A more recent variant described in [107] is defined for the $k - \omega$ model. Rewritten for the $k - \epsilon$ formulation, this implies[1]:

$$\mu_t = \bar\rho\nu_t = C_\mu \, f_\mu \, \bar\rho k^2/\epsilon,$$

with

$$f_\mu = \frac{1/40 + Re_T/67}{1 + Re_T/67},$$
$$Re_T = \frac{\bar\rho k^2 \, Re}{\epsilon}.$$

---

[1]Note that the formulation of [107] with respect to Re_T is changed here in order to preserve the similarity with the notation of the LRN correction from [52]. The C_μ is no longer included in the definition of Re_T. As a result, the term $Re_T/6$ in the definition of f_μ is replaced by $Re_T \cdot C_\mu/6 = Re_T/67$.

Again, a large Reynolds number, Re, results in a value of f_μ that is close to one. It is important to perform direct numerical simulations in order to get an impression of the validity of these RaNS models. We next continue with a comparison between several model assumptions and the present DNS data.

4.2 RaNS approximations

Three assumptions are studied that are typical for modeling in RaNS. This is done in the sense of an *a priori* analysis of the DNS data. We start with the assumption of a balance between production and dissipation [94]. Subsequently the eddy viscosity hypothesis is considered. The Reynolds stress tensor, based on results of the $k - \epsilon$ model and two of its low Reynolds number corrections, is evaluated and compared with the DNS predictions. Finally we consider the gradient-diffusion hypothesis. In this chapter the results are based on the fine-resolution DNS and the largest time sample available (until $T = 150 \, T_F$).

4.2.1 Production equals dissipation?

In several RaNS models, a local balance of production and dissipation of turbulence kinetic energy is assumed [94]. In the previous chapter, the energy budgets of the turbulence kinetic energy equation were collected. It was already concluded that almost all terms should be included. Next to the production and dissipation, also the turbulent diffusion and pressure-dilatation contributions had a significant contribution to the behaviour of the turbulence kinetic energy.

Subsequently, the balance was integrated over x_2 in order to consider the total contribution of each quantity at one streamwise location. The terms that remained were $\int P \, dx_2$, $\int \bar{\rho} \epsilon \, dx_2$ and $\int T_t \, dx_2$. This is summarized in Figure 4.1 where the streamwise evolution of the integral of these terms is plotted. It is clear that both the integral production P and transport T_t decrease in the same way between $x_1 = 150$ and $x_1 = 250$ and then increase again until $x_1 = 300$. The main part of P comes from $-\overline{\rho u_1'' u_2''} \partial_2 \tilde{u}_1$ and $-\overline{\rho u_1'' u_2''}$ also showed a decrease followed by an increase from $x_1 = 150$ (see Figure 3.4 where the peak of $\overline{\rho u_1'' u_2''}$ is plotted as a function of x_1). Furthermore, the fluctuations in $\int T_t \, dx_2$ are balanced by the small fluctuations around zero in the pressure-dilatation $\int P_d \, dx_2$. Summarizing, the dissipation $\int \bar{\rho} \epsilon \, dx_2$ is about equal to $\int (P - T_t) \, dx_2$ and remains at about the same level from $x_1 = 200$ onward.

As a result, it can be concluded that the assumption of a balance of production and dissipation is not valid in a local sense. On the level of budgets integrated over x_2, the contribution of several terms could, however, be neglected.
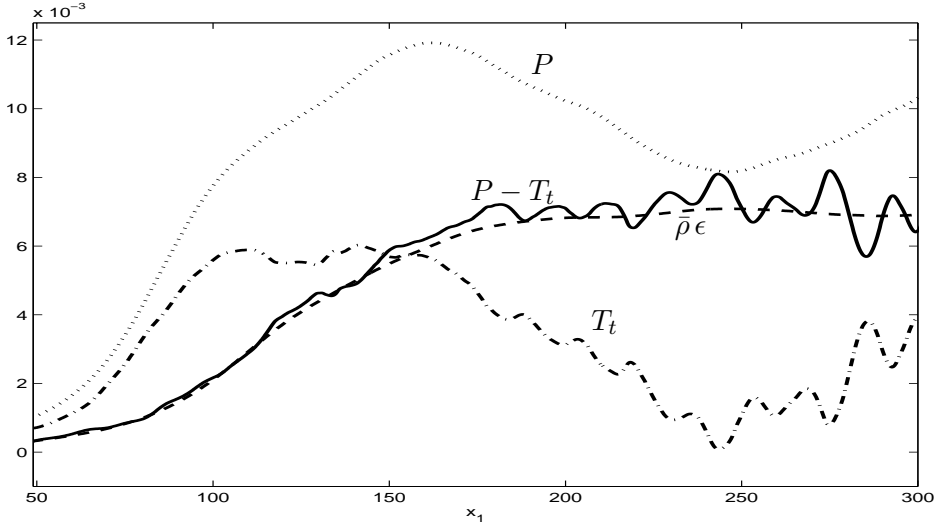
Figure 4.1: Main terms of the tke-equation integrated over x_2, normalized with ΔU^3 and plotted as a function of x_1.

The integrated production and dissipation are of equal order of magnitude. However, the balance result is definitively improved when also the integrated transport term is included in the integral balance. The streamwise evolution of the integrated dissipation with respect to the combination of integrated production and transport displays deviations up to ten percent. When also the integrated pressure-dilatation is included, this deviation is reduced with a factor of two. This evaluation of RaNS approximations is next continued with the assumption of eddy viscosity.

4.2.2   Eddy viscosity assumption

We consider the eddy viscosity relation, presented in Section 4.1. We recall the following expression for the eddy viscosity (see (4.3)):

$$\mu_{ij}(x_1, x_2) = \frac{N_{ij}}{D_{ij}} = \frac{-\overline{\rho u_i'' u_j''} + 2/3\,\bar{\rho}k\delta_{ij}}{\partial_j \tilde{u}_i + \partial_i \tilde{u}_j - 2/3\,\partial_k \tilde{u}_k \delta_{ij}}, \tag{4.6}$$

with numerator N_{ij} and denominator D_{ij}. Here, a tensor expression is used for the eddy viscosity μ_t since it may be different for each component of the Reynolds stress tensor. For the present results, N_{ij} and D_{ij} are largest for $(i,j) = (1,2)$. The dominant term of D_{12} is $\partial_2 \tilde{u}_1$, and μ_t is approximated by:

$$\mu_{12} \approx \frac{-\overline{\rho u_1'' u_2''}}{\partial_2 \tilde{u}_1}. \tag{4.7}$$

In this way, we have constructed an eddy viscosity that can be used to test RaNS model assumptions. From the DNS results of the previous chapter, we know that both the numerator and the denominator are positive. As a result, the eddy viscosity is positive as it should.

In Figure 4.2 we show the actual Reynolds stress profile at a characteristic x_1 and x_2 location and compare it with the standard $k - \epsilon$ model approximations and two LRN corrections. In Table 4.1 the three settings that are considered have been summarized. We stress that k and ϵ used in the models are not approximated but directly evaluated from the DNS result. Figure 4.2.a shows that the model results are approximately symmetric while the actual Reynolds stress displays a skewness. In the far field, the best approximation for the Reynolds stress arises from the standard $k - \epsilon$ model. Around the centerline, the standard $k - \epsilon$ prediction is worse than the two LRN corrections, however. On the whole, the agreement is quite limited.

Results of an incompressible turbulent channel flow [43] show that the standard $k - \epsilon$ result also underestimates the DNS at low-shear locations far
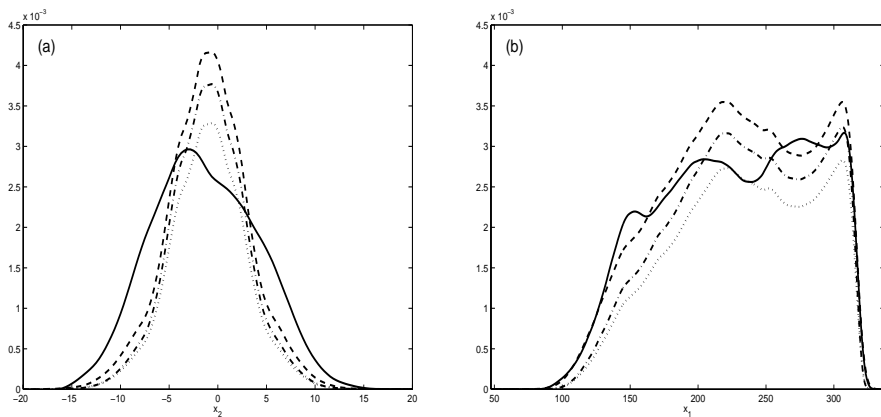
Figure 4.2: Negative Reynolds stress profiles, $-\overline{\rho u_1'' u_2''}$, (—), standard $k - \epsilon$ approximations $(--)$, LRN corrections from [52] $(-\cdot)$ and from [107] $(\cdots)$ at $x_1 = 257$ as a function of x_2 (a) and at $x_2 = -4$ as a function of x_1 (b).

	Reynolds stress
DNS	$\overline{\rho u_1'' u_2''}$
$k - \epsilon$	$C_\mu\, \bar{\rho} k^2 / \epsilon\, \partial_2 \tilde{u}_1$
LRN	$C_\mu\, f_\mu\, \bar{\rho} k^2 / \epsilon^*\, \partial_2 \tilde{u}_1$

Table 4.1: Expressions for the Reynolds stress (approximation).

from the wall while the LRN result from [52] is even smaller. The behaviour close to the wall in channel flow may be compared with the mixing layer centerline in the sense that both have a steep streamwise velocity gradient that decreases again when moving away from this region. In ref. [43] the DNS values close to the wall are overestimated by the standard $k - \epsilon$ model and the LRN prediction. So, the findings from the channel flow regarding the modeling of the Reynolds stress support the present mixing layer findings.

Finally, we focus on the value of C_μ which throughout this chapter was taken equal to 0.09 as is usually done [47, 52, 107]. From Figure 4.2.b it is clear that for this value of C_μ the centerline $k - \epsilon$ result is in reasonable agreement with the DNS result. This can be illustrated in a more quantitative way by calculating the value of C_μ such that the integral contribution of the exact and the $k - \epsilon$ approximation for $\overline{\rho u_1'' u_2''}$ are equal. Based on (4.5) and (4.7), we minimize the error that is made:

$$-\overline{\rho u_1'' u_2''} - C_\mu \bar{\rho} k^2 / \epsilon \, \partial_2 \tilde{u}_1.$$

The expression for the value, C_μ^*, that fits the DNS result best, is found from the following least square approximation:

$$C_\mu^* = \frac{\iint AB \, dx_2 dx_1}{\iint BB \, dx_2 dx_1}, \tag{4.8}$$

where

$$A = -\overline{\rho u_1'' u_2''},$$
$$B = \bar{\rho} k^2 / \epsilon \, \partial_2 \tilde{u}_1.$$

For the LRN settings, C_μ^* is computed in a similar way with f_μ included in B. Results for C_μ^* are collected in Table 4.2.

It is clear from the table that relatively high profiles in Figure 4.2.a give rise to a lower value of C_μ^*. These overall values equal 0.075, 0.085 and 0.100 for

x_s	x_e	$k - \epsilon$	LRN [52]	LRN [107]
50	290	0.071	0.085	0.098
100	290	0.074	0.086	0.099
150	290	0.079	0.087	0.102
200	290	0.076	0.084	0.097

Table 4.2: Values of C_μ^* for the standard $k - \epsilon$ model and two of its LRN corrections, based on different streamwise intervals from x_s to x_e.

respectively the $k-\epsilon$ model and LRN corrections from [52] and [107]. We note that the values of C_μ^* based on several streamwise intervals are approximately equal within each model. However, when the profiles at several values of x_1 are compared, it is clear that the local difference is still large. In Figure 4.2.a, the difference between the DNS and the $k-\epsilon$ result is up to 1.5×10^{-3} which is fifty percent of the maximum DNS value of 3.0×10^{-3}. As a result, optimization does not resolve the more severe problems with eddy viscosity.

Up to now, only the Reynolds stress, $\overline{\rho u_1'' u_2''}$ was considered. We next study the turbulence intensities, *i.e.*, the diagonal components of the Reynolds stress tensor. Evaluating the eddy viscosity assumption (4.6) for $i = j = 1$ results in:

$$\overline{\rho u_1'' u_1''} = -\mu_t(2\partial_1 \tilde{u}_1 - 2/3\,\partial_k \tilde{u}_k) + 2/3\,\bar{\rho}k$$
$$\approx 2/3\,\bar{\rho}k,$$

since the term between brackets can be neglected as was verified in the present DNS setting. Its value is less than three percent of $2/3\,\bar{\rho}k$. In the same way we can conclude this for $i = j = 2$ where $\partial_2 \tilde{u}_2$ is small and for $i = j = 3$ using $\tilde{u}_3 \equiv 0$. Thus, for the present flow, the eddy viscosity μ_t does not play a role of importance in the modeling of the diagonal components of the Reynolds stress tensor. As a result, the eddy viscosity assumption implies that the turbulence is approximately isotropic, *i.e.*,

$$\frac{2}{3}\bar{\rho}k \approx \overline{\rho u_1'' u_1''} \approx \overline{\rho u_2'' u_2''} \approx \overline{\rho u_3'' u_3''}.$$

Moreover, we conclude that results of the LRN models (for $i = j$) cannot be distinguished from the standard $k - \epsilon$ results. As a result, the LRN models only appear to be relevant for the Reynolds stress $\overline{\rho u_1'' u_2''}$.

From Chapter 3 we know that the peaks of the three diagonal elements of the Reynolds stress tensor are not at the same level. This contrast is clearly illustrated in Figure 4.3. The turbulence intensities, $\overline{\rho u_i'' u_i''}$, and their predictions from the standard $k - \epsilon$ model for all three directions are collected at a characteristic streamwise location. It is clear from the figure that the $k - \epsilon$ approximation is equal for all three turbulence intensities. This profile is close to that of $\overline{\rho u_2'' u_2''}$, while it underestimates $\overline{\rho u_1'' u_1''}$ and overestimates $\overline{\rho u_3'' u_3''}$. The resulting contour plot for $\overline{\rho u_2'' u_2''}$ is shown in Figure 4.4 together with its $k - \epsilon$ prediction. The $k - \epsilon$ approximation provides a good estimate of this particular turbulence intensity. However, in Chapter 3 we conjectured that the spanwise turbulence intensity will increase when a wider domain is used for the simulation. As a result, k will increase as well and this may change the adequacy of the eddy viscosity assumption. Also other turbulent shear flow studies find a structurally higher level for $\overline{\rho u_1'' u_1''}$ compared to $\overline{\rho u_2'' u_2''}$ [33, 105]. This indicates a need for anisotropic models.
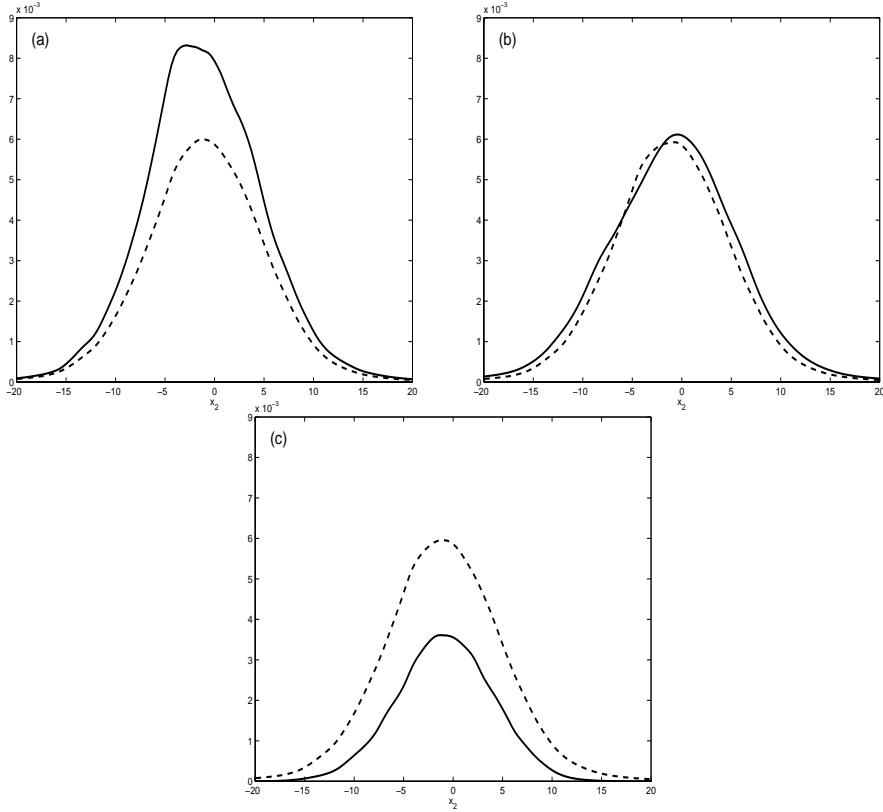
Figure 4.3: Streamwise (a), normal (b) and spanwise (c) turbulence intensities, $\overline{\rho u_i'' u_i''}$ (—), as well as the standard $k-\epsilon$ prediction, $-\mu_{k\epsilon}(2\partial_i \tilde{u}_i - 2/3\, \partial_k \tilde{u}_k) + 2/3\, \bar{\rho}k$ $(--)$, with $i = 1,\ 2$ and 3 at $x_1 = 257$ as a function of x_2.

Figure 4.4: Contour plot of normal turbulence intensity $\overline{\rho u_2'' u_2''}$ from the DNS (—) and based on $\mu_{k\epsilon}$ $(--)$ at isovalues $(2, 4, 6) \times 10^{-3}$ (from sides to centerline).

4.2.3 Gradient-diffusion hypothesis

In the $k - \epsilon$ model the turbulence kinetic energy equation is solved. One of the terms in this equation is the triple correlation, $-\frac{1}{2}\overline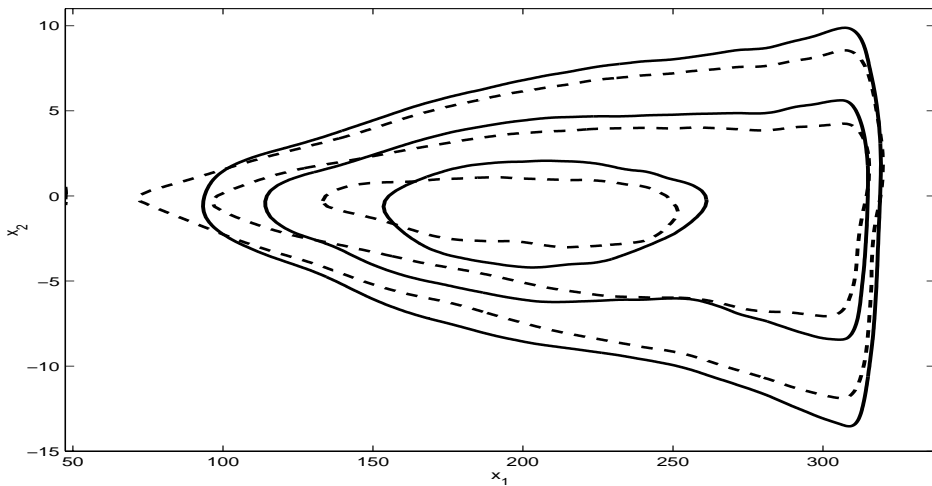{\rho u_i'' u_i'' u_j''}$. Based on Section 3.2.2, it is clear that this term has a large contribution and should be taken into account. It has to be modeled and the standard approximation made to represent transport of scalar quantities in a turbulent flow is that of gradient-diffusion. Its origin is in molecular transport processes, where $\overline{\phi \, u_j'} \sim \mu_t \, \partial_j \phi$ for the incompressible case and any quantity ϕ [107]. For comparison with incompressible flow, we recall the velocity fluctuation with respect to the bar-filter: $u_i' = u_i - \bar{u}_i$. For the compressible setting, the relation results in $-\frac{1}{2}\overline{\rho u_i'' u_i'' u_j''} \approx \mu_t/(\bar{\rho} \, \sigma_k) \, \partial_j(\bar{\rho}k)$, where the closure coefficient σ_k usually is taken equal to one [107]. This approximation is referred to as the *gradient-diffusion hypothesis* and leads to

$$-\frac{1}{2}\partial_j \overline{\rho u_i'' u_i'' u_j''} \approx \partial_j\left(\frac{\mu_t}{\bar{\rho}}\partial_j \bar{\rho}k\right). \tag{4.9}$$

A first impression of this model can be obtained from Figure 3.6 which shows that the shape of the profile of D_t corresponds with the shape of $\partial_{22}k$ (see also Figure 3.8). Based on the findings from Section 4.2.2 we employ μ_{12} for the eddy viscosity, so:

$$-\frac{1}{2}G_j \approx \frac{\mu_{12}}{\bar{\rho}}\partial_j(\bar{\rho}k), \quad j = 1, 2, \tag{4.10}$$

where G_j denotes the triple correlation in the j-direction, $\overline{\rho u_i'' u_i'' u_j''}$. The signs of both sides of (4.10) are collected in Table 4.3. It is clear from the table that the sign of $\mu_{12}/\bar{\rho}\, \partial_1 \bar{\rho}k$ is not corresponding to that of $-G_1$ for $x_2 < 0$. However, since the derivative with respect to x_1 is always small compared to the derivative with respect to x_2, both terms are of minor importance in (4.9). We next compute the correlation coefficients. Finally, the profiles of both sides

	$x_2 < 0$	$x_2 > 0$	max $\times 10^{-4}$
$\mu_{12}/\bar{\rho}\, \partial_1 \bar{\rho}k$	> 0	> 0	0.059
$\mu_{12}/\bar{\rho}\, \partial_2 \bar{\rho}k$	> 0	< 0	1.3
$-\overline{\rho u_i'' u_i'' u_1''}/2$	< 0	> 0	3.8
$-\overline{\rho u_i'' u_i'' u_2''}/2$	> 0	< 0	2.8

Table 4.3: Signs and $\max_{x_1, x_2}(|\cdot|)$ values of terms in the gradient-diffusion hypothesis and evaluated for the DNS results.

in (4.9) are compared directly. In the rest of this section, μ_{12} is evaluated according to approximation (4.7), if not mentioned otherwise.

In order to study the model hypothesis (4.10) more quantitatively, we define a correlation coefficient. Several correlations are shown in Figure 4.5 as a function of the streamwise coordinate. The correlation coefficient C is defined as follows:

$$C(f,g) = \frac{(f,g)}{\sqrt{(f,f) \cdot (g,g)}},$$

where (f,g) denotes the integral of $f\,g$ over x_2. By definition $|C| \leq 1$ and is close to one if f is close to αg with α an arbitrary constant. Therefore, we also compare the profiles directly. The correlation coefficient between $-G_1/2$ and $\mu_{12}/\bar{\rho}\,\partial_1(\bar{\rho}k)$ ($j=1$ in (4.10)) is weak, with a correlation coefficient below 0.5. In contrast, the correlation coefficient between $-G_2/2$ and $\mu_{12}/\bar{\rho}\,\partial_2(\bar{\rho}k)$ is larger than 0.95 (dashed line) for about the whole streamwise domain beyond $x_1 = 60$. Finally we included the correlation coefficient between $-G_1/2$ and $+G_2/2$. This correlation value is even better.

For a proper analysis, also the profiles themselves should be compared directly. In Figure 4.6 the four terms are plotted as a function of x_1 and x_2 at some specific value of x_2 and x_1 respectively. As expected, $\mu_{12}/\bar{\rho}\,\partial_1(\bar{\rho}k)$ is very small. The profiles of $-G_2/2$ and $\mu_{12}/\bar{\rho}\,\partial_2(\bar{\rho}k)$ display relatively the same spatial variations. However, $-G_2/2$ is about a factor two to three larger than $\mu_{12}/\bar{\rho}\,\partial_2(\bar{\rho}k)$. So, the gradient-diffusion assumption is satisfied better when we adjust the closure coefficient to $\sigma_k = 2/5$.

Figure 4.5: Correlation coefficient between $-G_1/2$ and $\mu_{12}/\bar{\rho}\,\partial_1(\bar{\rho}k)$ (—), between $-G_2/2$ and $\mu_{12}/\bar{\rho}\,\partial_2(\bar{\rho}k)$ (−−), and between $-G_1/2$ and $+G_2/2$ (−·) as a function of the streamwise coordinate.
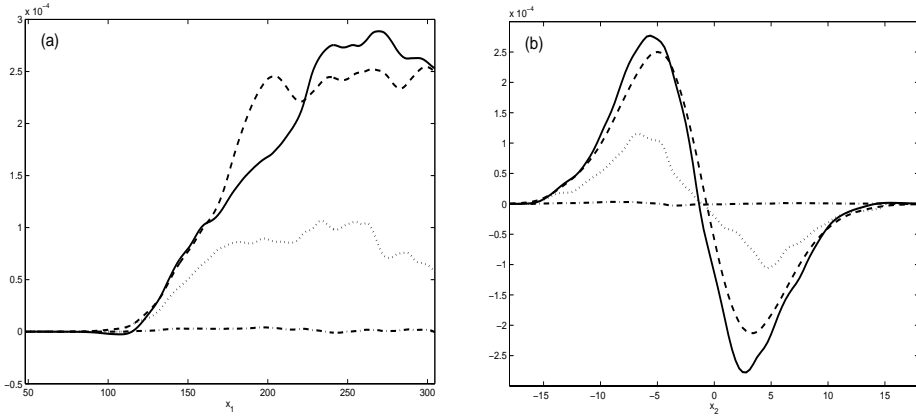
Figure 4.6: Profiles of $+G_1/2$ (—), $-G_2/2$ (−−), $\mu_{12}/\bar{\rho}\,\partial_1(\bar{\rho}k)$ (−·) and $\mu_{12}/\bar{\rho}\,\partial_2(\bar{\rho}k)$ (···), as a function of x_1 at $x_2 = -4$ (a) and as a function of x_2 at $x_1 = 257$ (b).
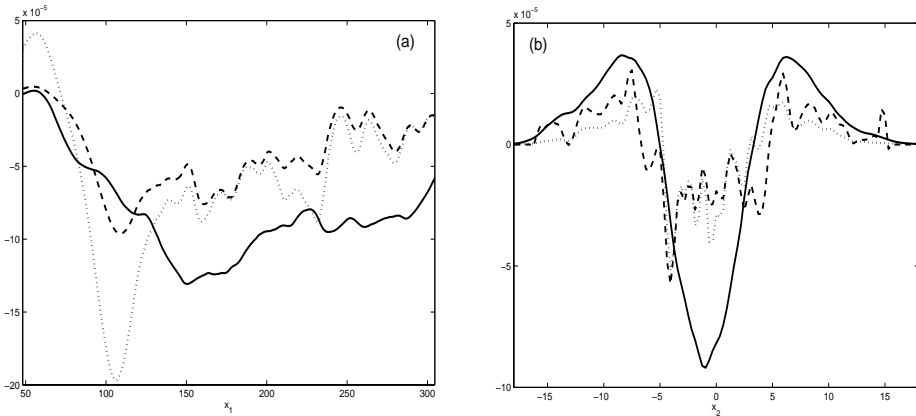

Figure 4.7: Profiles of $-\partial_j G_j/2$ (—) and $\partial_j(\mu_{12}/\bar{\rho}\,\partial_j(\bar{\rho}k))$ for the exact evaluation (−−) and the $k-\epsilon$ result (···) as a function of x_1 at $x_2 = -1$ (a) and as a function of x_2 at $x_1 = 257$ (b).

Finally these quantities are compared at the divergence level from relation (4.9). In Figure 4.7 we have collected the profiles from both sides of this approximation, again at some specific value of x_1 and x_2. Also the evaluation based on the standard $k-\epsilon$ result is included. Similarly as in the turbulent channel study from [43], the turbulent diffusion is larger than $\partial_j\mu_{12}/\bar{\rho}\,\partial_j(\bar{\rho}k)$ when μ_{12} is evaluated exactly. When the latter is based on the $k-\epsilon$ result, where C_μ^* is taken equal to the traditional value of 0.09, the positive peaks in Figure 4.7.b move closer to zero. On the contrary, they grow with some factors in [43].

4.3   Conclusions

In this chapter *a priori* comparisons between the DNS data and RaNS approximations have been made. Already in the previous chapter, it was found that the turbulence kinetic energy balance could not be reduced to a balance between only production and dissipation. Considering the integrated balance, the contribution of several terms could be neglected. Moreover, the integrated production and dissipation approximately balanced each other when also the integrated transport was included.

Next, the eddy viscosity assumption was considered for the Reynolds stress. This was done for the standard $k - \epsilon$ model and two low Reynolds number corrections. All three models displayed quite large deviations from the DNS result, either around the centerline peak value or at the edges of the mixing layer. However, when computing the coefficient C_μ that results in the best fit, in the sense of equal integral contributions of DNS and $k - \epsilon$ results as well as LRN corrections, the deviation from the traditional value was found to be only up to fifteen percent. For the remaining components in the Reynolds stress tensor, the eddy viscosity contribution could be neglected. As a result, the eddy viscosity assumption resulted in equal turbulence intensities for all three directions, similarly as in isotropic turbulence. This was not in correspondence, however, with the DNS results.

The gradient-diffusion hypothesis models the main diffusion term with the eddy viscosity and turbulence kinetic energy. This was first evaluated in a global way by collecting signs of the relevant terms. The term containing the streamwise derivative of k was close to zero, as expected. Furthermore, a correlation was defined to measure the correspondence of several combinations of terms. Similarly as for the analysis based on the signs of the relevant terms, the hypothesis was not satisfied in streamwise direction. On the divergence level, only the contribution of the normal direction is important. As a result, the correlation with the turbulent diffusion was considered to be satisfactory. Finally, the profiles were compared for characteristic locations of x_1 and x_2. The $+\overline{\rho u_i'' u_i'' u_1''}$, $-\overline{\rho u_i'' u_i'' u_2''}$ and $\mu_{12}/\bar{\rho}\,\partial_2(\bar{\rho}k)$ profiles relatively behaved approximately the same, with both triple correlations even at approximately the same level, while the term with the normal derivative of k was a factor two to three smaller. So, based on this direct comparison, the gradient-diffusion hypothesis is approximately satisfied, provided we use an adapted closure coefficient.

The model approximations acquired in this chapter may be used for the evaluation of some main contributions in the balance of the turbulence kinetic energy. Based on the model results for the Reynolds stress tensor, the production could be evaluated. The main part of the diffusion could be modeled with use of the gradient diffusion hypothesis.

Summarizing, we have evaluated three assumptions that often are em-

ployed in RaNS studies. The assumption of a local balance between production and dissipation was not supported by the present DNS result. Based on the Reynolds stress, a lower value for the model coefficient in the eddy viscosity assumption was found. The diagonal Reynolds stress tensor components prescribed a need for anisotropic models. The closure coefficient in the gradient-diffusion hypothesis should be adapted as well to a value of around 2/5. Finally we stress that this study of RaNS approximations has been restricted to an *a priori* analysis. Similarly as in LES, an *a posteriori* evaluation may imply other findings [104]. In the next chapter the DNS data is employed for the analysis of *a posteriori* LES modeling.

Chapter 5

Assessment of large-eddy simulation for the spatial mixing layer

The previous three chapters were devoted to direct numerical simulation (DNS) and the extraction of consequences for RaNS models from it. Such simulations are very costly since all scales of the turbulent motion must be accurately resolved. In practice this limits the Reynolds number, the complexity and the spatial extent of the flow that can be simulated. This suggests that large-eddy simulation (LES) might be better suited to study high-Reynolds-number fully developed mixing layer turbulence over long streamwise intervals. In LES one explicitly solves a coarse-grained version of the Navier-Stokes equations. The collective effect of the small scales on the large scales is taken into account through a 'subgrid-model'. Although LES is computationally much less expensive, it has the disadvantage that it leaves open the possibility of significant errors resulting from the approximation of the unknown subgrid stress by a model. Moreover, the influence of the specific numerical scheme used in LES needs to be assessed in detail.

The main goal of this chapter is the assessment of LES through comparison with DNS. Based on the results of this chapter, we specify a subgrid-model, a suitable resolution and initial and boundary conditions for LES of more complex flows, presented in Chapter 6. Throughout the present chapter we retain the 'minimal mixing layer' as used up to now. In the analysis we incorporate various flow quantities. These involve instantaneous variables, mean quantities, fluctuation characteristics and properties such as self-similarity.

The study of self-similarity in turbulent shear flows, as considered in Chapter 3, requires a large computational domain as well as long time-sampling. This makes the LES technique very suitable. Already in Chapter 2 we found

that the current configuration only displayed signs of self-similarity for the momentum thickness, streamwise mean momentum density and the streamwise turbulence intensity. The remaining components of the Reynolds stress tensor did not display self-similar behaviour, perhaps because of a lack of streamwise or spanwise domain length. We come back to this subject in the next chapter where a feasibility study is performed with regard to the numerical simulation of more realistic mixing layers.

In the present chapter, large-eddy simulations for the reference configuration described in Chapter 2 are performed. This will involve various subgrid-models. The transition from laminar to developed turbulent flow is monitored and the performance of the subgrid-models is investigated in both the transitional and the turbulent regime. The present simulations and the equivalent temporal mixing layer study from [104] are compared. In the rest of this chapter, we refer to the study in [104] as the temporal mixing layer. In order to develop LES in a reliable manner, we study the sensitivity regarding resolution and boundary conditions. We recall that the 'minimal mixing layer' as used up to now is not possible in laboratory experiments. Especially the narrow spanwise direction with its periodicity condition is not physical. So, similarly as for the DNS we should be careful in the comparison of the LES results with experimental findings. This is postponed until the next chapter where we relax this constraint.

LES of the temporal mixing layer is extensively described in [104] where several models were employed and compared. It appeared that at a relatively low Reynolds number the dynamic models were considerably better than non-dynamic models. The dynamic mixed model which combines the scale-similarity model of Bardina [5] with a dynamic eddy viscosity displayed the best performance although the differences among the dynamic model predictions are comparably small [104]. The values of convective Mach number and Reynolds number in the present study are based on this configuration. For simulations at a much higher Reynolds number, which were performed at a larger computational domain, a certain amount of dissipation was necessary for stability. The dynamic eddy viscosity model yielded turbulent statistics which displayed a nearly self-similar development.

A number of somewhat related DNS-LES studies have been reported in literature. In ref. [4] the DNS calculations of [77] for the temporal mixing layer were extended by examining the effect of domain size and initial conditions using LES. It was concluded that the self-similar state of mixing layers is not unique since, among others, the initial conditions and the size of the domain have quite significant effects. These influence the shape of the coherent eddies of the flow and their statistics. In ref. [40] self-similarity of the temporal turbulent plane wake is considered using LES. Large-eddy simulations employing the dynamic localization model from [39] were used to extend

the computational domain of previous direct numerical simulations reported in [66]. Like the wake experiments, the large-eddy simulations suggest that non-unique self-similar states, characterized by different spreading rates and turbulent statistics, are possible and that they can be maintained for significant temporal periods. In ref. [21] a spatially developing incompressible mixing layer is studied using LES with the filtered structure function subgrid-scale model. The molecular viscosity is assumed to be zero. The pairing process is investigated and it turned out that for the LES the same types of flow patterns were obtained as in previous temporal DNS studies. Finally, we mention that an *a priori* LES analysis of the DNS database acquired from Chapter 2 is reported in ref. [36].

This chapter is organized as follows. In Section 5.1 the equations and definitions needed for LES are given. Subsequently, the basic subgrid-models and their dynamic formulations are introduced in Section 5.2. The specification of the LES of the mixing layer is given in Section 5.3. Furthermore the evaluation of the filtered fine-grid DNS data used for reference is described. In Section 5.4 the results of different subgrid-models are presented and discussed. The sensitivity of these results with respect to changes in, *e.g.*, resolution is considered in Section 5.5. Finally, we give the conclusions in Section 5.6.

5.1 Governing equations

In large-eddy simulations, similarly as in the Reynolds-averaging procedure as described in Chapter 4, any flow variable f is decomposed into a large-scale contribution $\overline{f}$ and a small-scale contribution f' :

$$f = \overline{f} + f'.$$

The filtered field, $\overline{f}$, is generated from the unfiltered field with the use of a filter function G:

$$\overline{f}(\mathbf{x}) = \int_{\Omega} G(\mathbf{x}, \boldsymbol{\xi}) f(\boldsymbol{\xi}) \, d\boldsymbol{\xi},$$

for vectors $\mathbf{x}$ and $\boldsymbol{\xi}$ in the flow domain Ω. Similarly, the Favre-filter is introduced to simplify the notation for compressible flow:

$$\tilde{f} = \frac{\overline{\rho f}}{\overline{\rho}},$$

giving rise to the decomposition $f = \tilde{f} + f''$.

The filter function has a filter width Δ and is normalized such that

$$\int_\Omega G(\mathbf{x}, \boldsymbol{\xi}) \, d\boldsymbol{\xi} = 1, \tag{5.1}$$

for every $\mathbf{x}$ in Ω. A popular filter is the top-hat filter which is defined as follows:

$$G(\mathbf{x}, \boldsymbol{\xi}) = \begin{cases} 1/\Delta^3 & \text{if } |x_i - \xi_i| < \Delta_i/2, \\ 0 & \text{otherwise.} \end{cases} \tag{5.2}$$

The basic filtered flow variables are the filtered density $\bar{\rho}$, the filtered pressure $\bar{p}$ and the Favre filtered velocity vector $\tilde{\mathbf{u}}$. The corresponding filtered continuity, momentum and energy equations are obtained if the 'bar'-filter is applied to the Navier-Stokes equations [101]:

$$\partial_t \bar{\rho} + \partial_j(\bar{\rho}\tilde{u}_j) = 0, \tag{5.3}$$

$$\partial_t(\bar{\rho}\tilde{u}_i) + \partial_j(\bar{\rho}\tilde{u}_i\tilde{u}_j) + \partial_i\bar{p} - \partial_j\breve{\sigma}_{ij} = -\partial_j(\bar{\rho}\tau_{ij}) + \partial_j(\overline{\sigma}_{ij} - \breve{\sigma}_{ij})$$
$$(i = 1, 2, 3), \tag{5.4}$$

$$\partial_t\breve{e} + \partial_j((\breve{e} + \bar{p})\tilde{u}_j) - \partial_j(\breve{\sigma}_{ij}\tilde{u}_i) + \partial_j\breve{q}_j = -\alpha_1 - \alpha_2 - \alpha_3 + \alpha_4$$
$$+ \alpha_5 - \alpha_6, \tag{5.5}$$

with

$$\bar{\rho}\tau_{ij} = \overline{\rho u_i u_j} - \overline{\rho u_i}\,\overline{\rho u_j}/\bar{\rho} = \bar{\rho}(\widetilde{u_i u_j} - \tilde{u}_i\tilde{u}_j),$$

$$\breve{\sigma}_{ij} = S_{ij}(\tilde{\mathbf{u}})/Re,$$

$$\breve{e} = \frac{\bar{p}}{\gamma - 1} + \frac{1}{2}\bar{\rho}\tilde{u}_i\tilde{u}_i,$$

$$\breve{q} = -\frac{1}{(\gamma - 1)RePrM_\infty^2}\partial_j\tilde{T},$$

$$\tilde{T} = \gamma M_\infty^2 \frac{\bar{p}}{\bar{\rho}},$$

and $\alpha_1 - \alpha_6$ are further specified as follows [101]:

$$\alpha_1 = \tilde{u}_i\partial_j(\bar{\rho}\tau_{ij}),$$

$$\alpha_2 = \partial_j(\overline{pu_j} - \bar{p}\tilde{u}_j)/(\gamma - 1),$$

$$\alpha_3 = \overline{p\partial_j u_j} - \bar{p}\partial_j\tilde{u}_j,$$

$$\alpha_4 = \overline{\sigma_{ij}\partial_j u_i} - \overline{\sigma}_{ij}\partial_j\tilde{u}_i,$$

$$\alpha_5 = \partial_j(\overline{\sigma}_{ij}\tilde{u}_i - \breve{\sigma}_{ij}\tilde{u}_i),$$

$$\alpha_6 = \partial_j(\overline{q}_j - \breve{q}_j).$$

The turbulent stress tensor $\bar{\rho}\tau_{ij}$ is the only subgrid-term in incompressible flow. Therefore we assume that also compressible LES at low Mach numbers

mainly requires the modeling of $\bar{\rho}\tau_{ij}$. This is supported by the temporal mixing layer study [100]. It is clear from (5.4) that the subgrid-term $\bar{\rho}\tau_{ij}$ contains information from the unfiltered field. A subgrid-model should be included for the turbulent stress tensor $\bar{\rho}\tau_{ij}$ in order to express the filtered Navier-Stokes equations solely in filtered variables.

Finally we note that up to this chapter, the bar notation implied averaging over the homogeneous variables time and x_3 (RaNS). In the remainder of this thesis the bar-operator denotes the LES filter as introduced above, while the (additional) averaging over time and x_3 is now denoted by $\langle \cdot \rangle$. In the next section we present the subgrid-models that will be employed in this chapter.

5.2 Basic models and their dynamic realizations

The most important term in the closure of the filtered equations is the turbulent stress tensor. In this section two basic models are presented for the turbulent stress tensor $\bar{\rho}\tau_{ij}$: the Smagorinsky [83] and the Bardina model [5]. The former is an eddy viscosity model while the latter is based on a scale-similarity assumption. Subsequently the Germano identity is formulated. This identity leads to the dynamic eddy viscosity model and the dynamic mixed model. The model for $\bar{\rho}\tau_{ij}$ will be denoted by m_{ij}.

5.2.1 The Smagorinsky model

The Smagorinsky model [83] is given by

$$m_{ij} = -\bar{\rho}C_S^2\Delta^2|S_{ij}(\tilde{\mathbf{u}})|S_{ij}(\tilde{\mathbf{u}}),$$

where

$$|S_{ij}(\tilde{\mathbf{u}})|^2 = \frac{1}{2}S_{ij}(\tilde{\mathbf{u}})S_{ij}(\tilde{\mathbf{u}}),$$

with S_{ij} the strain rate defined in (2.5). It is a popular model because its evaluation does not require extra filtering unlike many other models. It is purely dissipative and provides an effective way of energy reduction at small retained scales.

Following high Reynolds number temporal simulations for the temporal mixing layer, the Smagorinsky constant C_S is taken equal to 0.1. The model was observed to be too dissipative and to hinder the transition to turbulence when a higher value of 0.17 was taken [104]. This is commonly known and is also experienced in the present study. *A priori* tests of the temporal mixing layer and several other flows display a low correlation between the Smagorinsky model and the actual turbulent stress [99].

5.2.2 The Bardina model

The scale-similarity model was formulated by Bardina [5] and reviewed in [57]. The tensor m_{ij} is based on two subsequent applications of the bar-filter and is defined as:

$$m_{ij} = \overline{\overline{\rho u_i}\,\overline{\rho u_j}/\bar{\rho}} - \overline{\overline{\rho u_i}}\,\overline{\overline{\rho u_j}}/\overline{\bar{\rho}}.$$

This model involves the assumption that velocities from different filter levels generate turbulent stresses with similar structures. The model for the turbulent stress tensor equals the definition for $\bar{\rho}\tau_{ij}$ with the unfiltered variables ρ and ρu_i replaced by their filtered equivalents $\bar{\rho}$ and $\overline{\rho u_i}$. The model does provide global dissipation as well as backscatter of energy. In several studies a high correlation is reported between the subgrid-stress of the Bardina model and the exact turbulent stress [57, 99]. In many simulations this model was found insufficiently dissipative and required an extra dissipative term.

5.2.3 The dynamic procedure

Several LES studies have shown that in particular the dissipative character of both basic models introduced above is not appropriate being either too large or too small. These short-comings are often removed by applying the dynamic procedure which is introduced next. The Germano identity [38] for the turbulent stress tensor forms the basis for so-called dynamic subgrid-models. It involves a second test filter denoted by $(\cdot)\hat{}$ or $\widehat{(\cdot)}$ with a width usually equal to $2\,\Delta$. The identity states that

$$\widehat{\bar{\rho}}T_{ij} - \widehat{\overline{\rho\tau_{ij}}} = L_{ij}, \tag{5.6}$$

with

$$\widehat{\bar{\rho}}T_{ij} = \widehat{\overline{\rho u_i u_j}} - \widehat{\overline{\rho u_i}}\,\widehat{\overline{\rho u_j}}/\widehat{\bar{\rho}}, \tag{5.7}$$

$$L_{ij} = (\overline{\overline{\rho u_i}\,\overline{\rho u_j}}/\bar{\rho})\hat{} - \widehat{\overline{\rho u_i}}\,\widehat{\overline{\rho u_j}}/\widehat{\bar{\rho}}. \tag{5.8}$$

The first term on the left-hand side of (5.6) is the turbulent stress tensor appearing in the LES equations after subsequent application of the two filters. The second tensor is the test-filtered turbulent stress tensor. The remaining so-called 'resolved' term L_{ij} on the right-hand side can explicitly be calculated from the bar-filtered variables. The two dynamic models for the turbulent stress tensor in the following are obtained by substituting the corresponding basic models into the Germano identity and optimizing the coefficient.

5.2.4   The dynamic eddy viscosity model

The dynamic eddy viscosity model [37, 38] is based on the formulation of Smagorinsky's model with C_S^2 replaced by a coefficient C_d. The tensor m_{ij} is given by:

$$m_{ij} = -\bar{\rho} C_d \Delta^2 |S(\tilde{\mathbf{u}})| S_{ij}(\tilde{\mathbf{u}}). \tag{5.9}$$

The coefficient C_d is adjusted to the local structure of the flow in a dynamic way. As a result, the eddy viscosity reduces in places where turbulence is not very active. After substitution of the subgrid-model m_{ij} from (5.9) into the Germano identity, this results in the following relation for C_d :

$$C_d M_{ij} = L_{ij}, \tag{5.10}$$

with

$$M_{ij} = -\widehat{\bar{\rho}}(\kappa\Delta)^2 |S(\mathbf{v})| S_{ij}(\mathbf{v}) + (\bar{\rho}\Delta^2 |S(\tilde{\mathbf{u}})| S_{ij}(\tilde{\mathbf{u}}))\hat{} , \tag{5.11}$$

$$v_i = \widehat{\overline{\rho u_i}}/\widehat{\bar{\rho}}, \tag{5.12}$$

and L_{ij} as defined in (5.8). Here, we assumed that $\widehat{C_d f} \approx C_d \hat{f}$, *i.e.*, variations of C_d on the scale of the test-filter are assumed to be small. The value of κ appearing in the filter width of the consecutive application of both filters is taken equal to $\sqrt{5}$ as suggested in [104].

To calculate the model coefficient from equation (5.10) we apply an additional averaging over homogeneous directions. For the optimal description in a least squares sense [56], the 'error' is minimized with respect to C_d. This results in:

$$C_d = \frac{\langle M_{ij} L_{ij} \rangle_{x_3}}{\langle M_{ij} M_{ij} \rangle_{x_3}}. \tag{5.13}$$

The symbol $\langle \cdot \rangle_{x_3}$ denotes averaging over the spanwise domain which is the only homogeneous direction in the spatial domain. The averaging over the (periodic) streamwise direction as in the temporal setting is no longer performed. The model coefficient C_d is artificially put to zero at locations where the right-hand side of (5.13) results in a negative value. This clipping prevents numerical instability caused by negative values of C_d [104].

5.2.5   The dynamic mixed model

The dynamic mixed model has been introduced in [109] and modified in [98] in order to remove a mathematical inconsistency. It employs the sum of the Bardina and Smagorinsky model as basic model:

$$m_{ij} = \overline{\overline{\rho u_i}\,\overline{\rho u_j}/\bar{\rho}} - \overline{\overline{\rho u_i}}\,\overline{\overline{\rho u_j}}/\overline{\bar{\rho}} - \bar{\rho} C_d \Delta^2 |S(\tilde{\mathbf{u}})| S_{ij}(\tilde{\mathbf{u}}). \tag{5.14}$$

This model gives a relatively accurate representation of the turbulent stress by the similarity model while the lack of dissipation in this model is counteracted by the introduction of a dynamic eddy viscosity [104]. After substitution of the subgrid-model into the Germano identity, the following expression for C_d can be found:

$$H_{ij} + C_d M_{ij} = L_{ij},$$

with

$$H_{ij} = \widehat{\overline{\overline{\widehat{\overline{\rho u_i}\,\overline{\rho u}_j}/\widehat{\overline{\rho}}}}} - \widehat{\overline{\overline{\rho u}_i\,\overline{\rho u}_j}}/\widehat{\overline{\overline{\rho}}} - \left(\overline{\overline{\rho u_i}\,\overline{\rho u}_j/\overline{\rho}} - \overline{\overline{\rho u}_i}\,\overline{\overline{\rho u}_j}/\overline{\overline{\rho}}\right)\widehat{},$$

and the tensors L_{ij} and M_{ij} defined in (5.8) and (5.11) respectively.

Again, C_d is computed using the least square approximation, combined with averaging over homogeneous directions and if required clipping, *i.e.*:

$$C_d = \frac{\left\langle M_{ij}(L_{ij} - H_{ij})\right\rangle_{x_3}}{\left\langle M_{ij} M_{ij}\right\rangle_{x_3}}.$$

In the rest of this chapter the subscript x_3 is left out of the notation for the average operator $\langle\cdot\rangle_{x_3}$. The operator $\langle\cdot\rangle$ denotes spanwise averaging when used in the expression of C_d and it implies averaging over time and spanwise direction otherwise.

5.3   Description of the LES

In this section, we describe the LES and discuss some aspects that need special attention for spatially developing shear flows. Several choices are based on previous findings for the temporal mixing layer.

5.3.1   Specification of the reference large-eddy simulation

The filtered Navier-Stokes equations need a subgrid-model for the turbulent stress tensor in order to close the system of equations. The subgrid-terms created by nonlinearities in the viscous stress tensor are neglected and no model is assumed for the subgrid-terms in the energy equation [100]. At the inflow boundary, perturbations from Linear Stability Theory are imposed as before. The inflow perturbations are filtered in normal and spanwise direction to preserve theoretical consistency. It turned out that the streamwise filtering was not necessary.

The LES is initiated from a filtered DNS field that corresponds to a well developed turbulent flow. In this way, the effect of the different models on the flow can be considered directly. In particular, the deviation between the

LES solutions corresponding to different models can be assessed in detail as a function of time. The filtered field to start the LES is acquired from the finest DNS ($900 \times 192 \times 64$ points) using filter widths $(\Delta_1, \Delta_2, \Delta_3) = (6h_1, 6h_2, 8h_3)$. The grid size in x_i-direction is denoted by h_i. A resolution of $300 \times 64 \times 16$ is employed for the LES. The filter width is taken equal to twice the grid-spacing of the LES grid as suggested in [104]: $\Delta_i = 2h_i^{(\mathrm{LES})}$. As filter function we employ the top-hat filter, already defined in (5.2). This filter operator applied to a field f results in the following expression for $\overline{f}$:

$$\overline{f}(\mathbf{x}) = \frac{1}{\Delta^3} \int_{-\frac{1}{2}\Delta_3}^{\frac{1}{2}\Delta_3} \int_{-\frac{1}{2}\Delta_2}^{\frac{1}{2}\Delta_2} \int_{-\frac{1}{2}\Delta_1}^{\frac{1}{2}\Delta_1} f(\mathbf{x} + \mathbf{y}) \, d\mathbf{y}.$$

It is discretized using the trapezoidal rule. For the filter width Δ we take:

$$\Delta = (\Delta_1 \Delta_2 \Delta_3)^{1/3}.$$

The LES is started from the filtered DNS field at time 552. From Chapter 2 we know that the flow is fully developed by that time. The sampling for time-averaged properties starts at time 935. This is based on findings from Chapter 2 regarding the time for a signal to traverse the streamwise domain. The suitability of this time to start time-averaging is illustrated further on in Section 5.4.1. Unphysical effects which may have their origin in the initialization have disappeared at this stage of the flow development.

5.3.2   Filtering spatially developing DNS results

One of the steps in a systematic development of LES is the comparison with results acquired from DNS. To this purpose we use the DNS database discussed in the previous chapters. During the DNS several quantities averaged over time and x_3 are calculated, among which $\langle \rho \rangle$, $\langle \rho u_i \rangle$ and $\langle p \rangle$. In order to compare with LES these quantities are filtered, which yields $\overline{\langle \rho \rangle}$, $\overline{\langle \rho u_i \rangle}$ and $\overline{\langle p \rangle}$. It is important to note that the two operations commute. For example the momentum thickness can be calculated from

$$\theta(x_1) = \int_{-L_2/2}^{L_2/2} \langle \bar{\rho} \rangle \frac{\left(U_1 - \langle \overline{\rho u_1} \rangle / \langle \bar{\rho} \rangle \right) \left(\langle \overline{\rho u_1} \rangle / \langle \bar{\rho} \rangle - U_2 \right)}{(U_1 - U_2)^2} dx_2,$$

and thus can be expressed in terms of the basic filtered flow variables. As a result, the so-called filtered momentum thickness can be computed from (x_3, t)-averaged DNS results in a post-processing phase and furnish reference data for comparison with LES.

This procedure, however, cannot be applied for the Reynolds stress tensor, since it involves extra multiplication operators. In particular, during the DNS,

e.g., $\langle\rho u_i u_j\rangle$ usually is calculated which can be filtered to produce $\overline{\langle\rho u_i u_j\rangle}$, while in an LES $\bar{\rho}\tilde{u}_i\tilde{u}_j$ is computed which after averaging yields $\langle\bar{\rho}\tilde{u}_i\tilde{u}_j\rangle$. The latter usually cannot be extracted from the DNS database. A solution to this problem follows from the relation between filtered DNS and LES results:

$$\overline{\langle\rho u_i u_j\rangle} - \langle\bar{\rho}\tau_{ij}\rangle = \langle\bar{\rho}\tilde{u}_i\tilde{u}_j\rangle,$$

which leads to:

$$R_{ij}^* - \langle\bar{\rho}\tau_{ij}\rangle = R_{ij}^{LES}, \tag{5.15}$$

with

$$R_{ij}^* = \overline{\langle\rho u_i u_j\rangle} - \overline{\langle\rho u_i\rangle}\,\overline{\langle\rho u_j\rangle}/\overline{\langle\rho\rangle}$$
$$= \langle\bar{\rho}\widetilde{\tilde{u}_i\tilde{u}_j}\rangle - \langle\bar{\rho}\tilde{u}_i\rangle\langle\bar{\rho}\tilde{u}_j\rangle/\langle\bar{\rho}\rangle, \tag{5.16}$$
$$R_{ij}^{LES} = \langle\bar{\rho}\tilde{u}_i\tilde{u}_j\rangle - \langle\bar{\rho}\tilde{u}_i\rangle\langle\bar{\rho}\tilde{u}_j\rangle/\langle\bar{\rho}\rangle, \tag{5.17}$$
$$\langle\bar{\rho}\tau_{ij}\rangle = \langle\bar{\rho}(\widetilde{u_i u_j} - \tilde{u}_i\tilde{u}_j)\rangle. \tag{5.18}$$

Note that R_{ij}^* is the Reynolds stress tensor based on $\bar{\rho}$, $\tilde{\mathbf{u}}$ and $\overline{\rho u_i u_j}$ instead of ρ, $\mathbf{u}$ and $\rho u_i u_j$. The term $\langle\bar{\rho}\tau_{ij}\rangle$ usually is not monitored as part of the DNS. It can, *e.g.*, be estimated from a sufficiently large number of snapshots as shown in the next section. This is relevant for the comparison between DNS and LES. Further analysis is required regarding how higher order moment fluctuations from the DNS should be obtained for comparison with LES. These arise for example in the turbulence kinetic energy equation (3.3).

In order to compare the fine-grid DNS data with coarse-grid LES results, the DNS data are first filtered using the fine-grid result and subsequently injected onto the LES grid. This coarse field of basic filtered flow variables may be used to compute, *e.g.*, the spanwise vorticity or the momentum thickness. Note that the issue raised in this subsection does not occur in temporal simulations.

5.4 LES results

In this section we compare the results that arise from LES using the subgrid-models introduced in Section 5.2. Also results of a coarse-grid simulation in which no model is used, are included. This simulation corresponds to a simulation on a coarse grid starting from a filtered initial field and with filtered inflow perturbations. The filtered DNS results are included when available and appropriate. In this section we first present some results that characterize the instantaneous flow and help to assess the quality of specific models. We continue with the assessment of LES results based on long time-averaging.

5.4.1 Comparison of instantaneous results

The description of instantaneous results is started with the spanwise vorticity which has typical characteristics for each subgrid-model. We also illustrate how the solutions corresponding to different models develop in time. It is emphasized that one should be careful in comparing instantaneous LES predictions because the difference of two signals can appear large while, *e.g.*, mainly a phase difference is present.

In Figure 5.1 we collected the spanwise vorticity in a characteristic spanwise plane as well as in the centerplane for several subgrid-models. Also the filtered DNS results of Chapter 2 are included. The results of the dynamic mixed model are not included since they show similar structures as the dynamic eddy viscosity model. In the first part of the streamwise domain the Bardina model predictions are close to those of the dynamic mixed model and the filtered DNS. Beyond one third of the streamwise domain the contour lines in the centerplane display strong gradients when using no model or the Bardina model. The empty spaces in the filtered DNS solution that arise when the vortex tubes are above respectively below the centerplane can also be distinguished for the dynamic models. The dynamic eddy viscosity model is close to the no model simulation which can be explained by the fact that the dynamic coefficient is often clipped to zero. Compared to the temporal large-eddy simulation [104], the grid distance in the present study is a factor two finer in each direction. Also the Smagorinsky constant of 0.17 is reduced to 0.1. This results in a reduction of the excessive dissipation that is typical for this model. These two aspects explain why the present results do not show as clear a distinction between the Smagorinsky, Bardina and dynamic models as was found in the temporal study reported in [104].

Due to the dominant mean boundary layer profile, the filtered spanwise vorticity, $\overline{\omega}_3$, in the laminar part of the mixing layer is negative. As a result, the occurrence of positive spanwise vorticity in the mixing layer is related to the transition to turbulence [104]. Therefore we focus on the level of positive spanwise vorticity. In Figure 5.2 we show the time-averaged maximum values of the spanwise vorticity as a function of the streamwise coordinate. The maximum is taken over the x_3 and part of the x_2 domain where the $\langle \overline{\rho u_1} \rangle$ value deviates more than two percent from both free-stream values. For all models, this quantity is obtained from about forty snapshots and is subsequently averaged.

In Figure 5.2, the negative values of the time-averaged maximum spanwise vorticity just after the inflow display the laminar character of the flow there. Downstream of $x_1 = 170$, the filtered DNS result is overestimated by the Bardina- and no-model simulations while it is underestimated in the simulations using the other subgrid-models. More quantitatively, the deviation
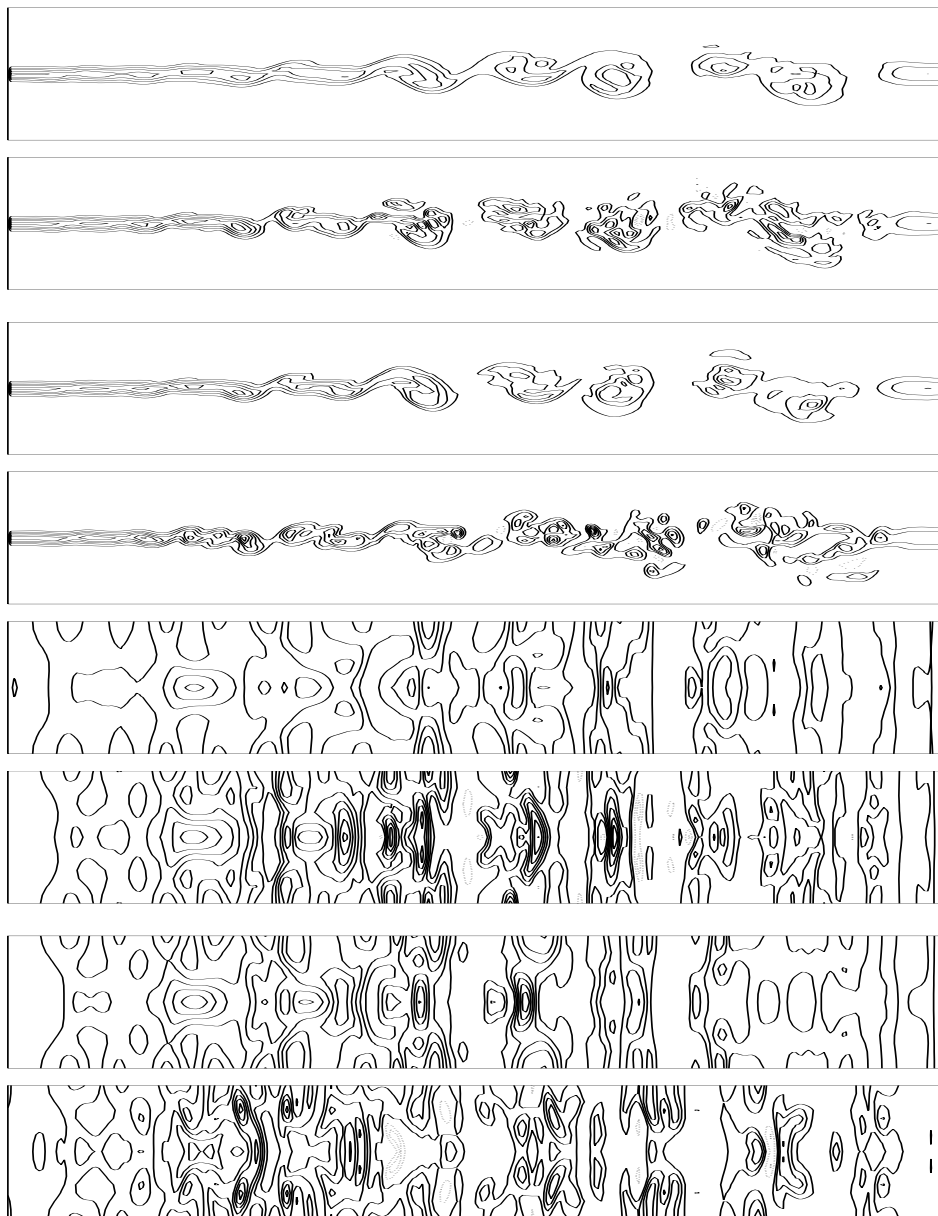
Figure 5.1: Filtered spanwise vorticity, $\overline{\omega}_{x_3}$, at time 935. The contour lines display negative (—) and positive ($\cdots$) values for $\pm(0.03, 0.06, \ldots, 0.21)$ in the spanwise plane at $x_3 = -L_3/4$ (top four plots) followed by the centerplane at $x_2 = 0$ (bottom four plots). All plots have x_1 as the horizontal axis. They display the results of (in top-down order) the Smagorinsky, Bardina, dynamic eddy viscosity and filtered DNS.
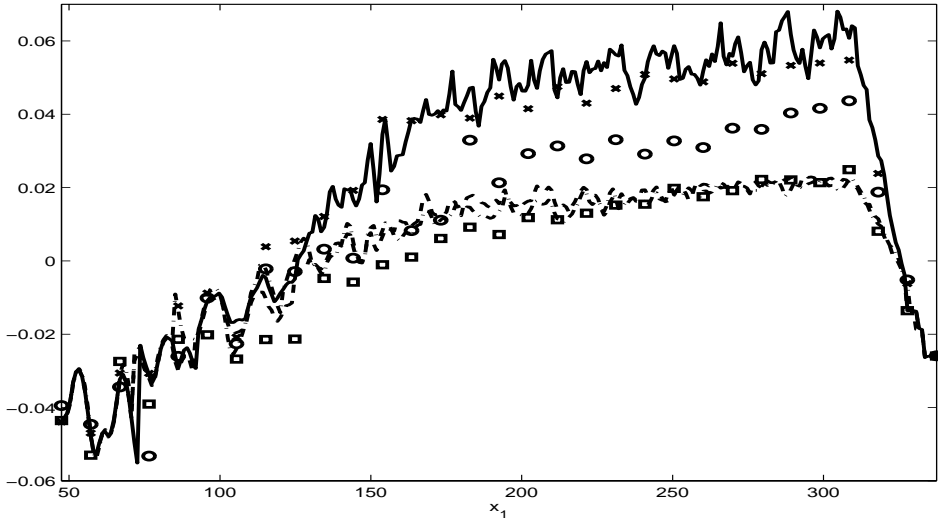
Figure 5.2: Time-averaged maximum value of filtered spanwise vorticity, $\langle\overline{\omega}_3\rangle_t$, as a function of x_1. The models used are Smagorinsky ($\square$), Bardina ($\times$), dynamic eddy viscosity ($--$), dynamic mixed ($-\cdot$). Also the no-model ($-$) and filtered DNS (o) results are included.

with the filtered DNS result - on average - is smallest for the dynamic eddy viscosity model and largest for the no-model result in the second part of the domain.

These findings will next be compared with those of the temporal study (see Figure 9 in [104]). The main difference with the present results is the low maximum spanwise vorticity level for the Smagorinsky model throughout the whole time (or, for the present setting, streamwise) domain. This can be explained from the higher value for the Smagorinsky constant in the temporal simulation. Furthermore, the deviation between the present filtered DNS and LES values is smaller for all models because of the finer LES grid. The moment in time in the temporal study around which the maximum spanwise vorticity of the filtered DNS becomes larger than that of the dynamic models equals about $t = 55$. This is in close correspondence with the streamwise location of $x_1 = 170$ mentioned above when using the convective velocity of 0.75 and the factor of four between the velocity differences of both settings (see relation (2.16)). Finally we mention that downstream of $x_1 = 200$ also the spanwise vorticity minimum for the filtered DNS is in between the (lower) no-model and Bardina predictions and the remaining models. So, we conclude that the extreme values of the spanwise vorticity from the filtered DNS are overestimated by the Bardina and no-model simulations and underestimated by those of the Smagorinsky and both dynamic models.

From the instantaneous snapshots we move to the time history of the centerplane streamwise momentum density. At a laminar streamwise location ($x_1 = 98$) the signals fluctuate with an amplitude which is largest for the Bardina model. A clear distinction exists between the Smagorinsky signal statistics and those of the other subgrid-models. The Smagorinsky value of the fluctuation amplitude is a factor of two smaller than the equivalent for the Bardina model. The time histories of the signal in the turbulent regime are shown in Figure 5.3. All models display a rapidly oscillating behaviour in time alternated with a slowly oscillating behaviour. Downstream of the laminar region the fluctuations in the Smagorinsky model have reached approximately the same level as those from other models. The root mean square value for the Smagorinsky signal is smallest and is about 25% lower than that of the Bardina and no-model result. The streamwise momentum density in the turbulent regime is seen not to result in a clear distinction between the performance of either subgrid-model.
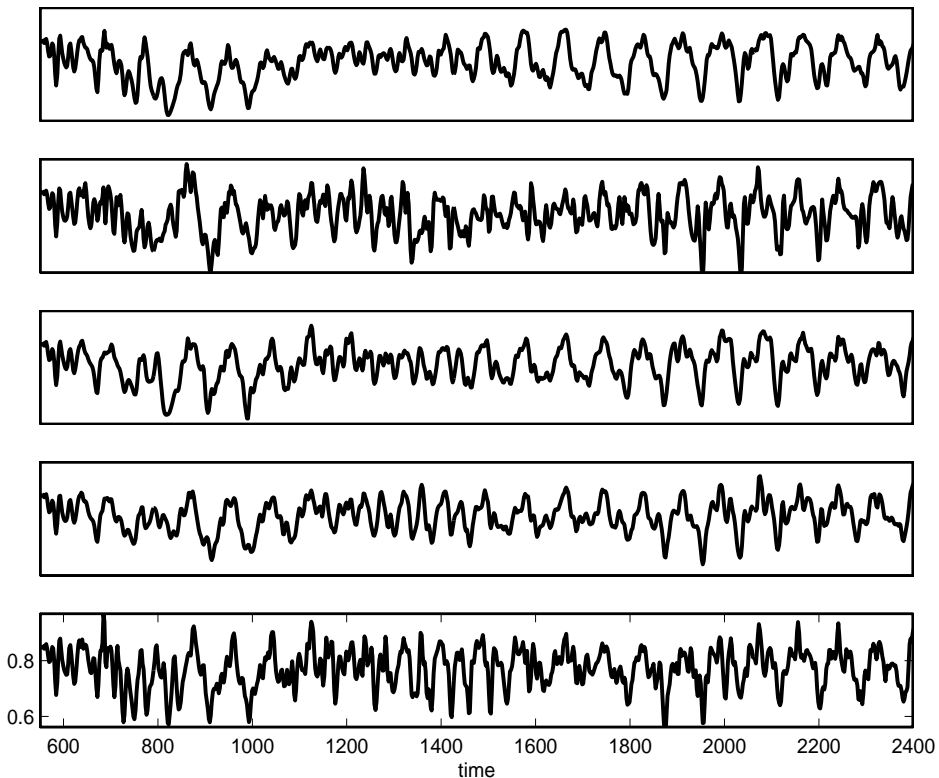

Figure 5.3: Centerplane $\overline{\rho u}_1$ signal at $x_3 = -L_3/4$ for x_1=250 as a function of time. The models used are (in top-down order) the Smagorinsky, Bardina, dynamic eddy viscosity, dynamic mixed and the no-model result.
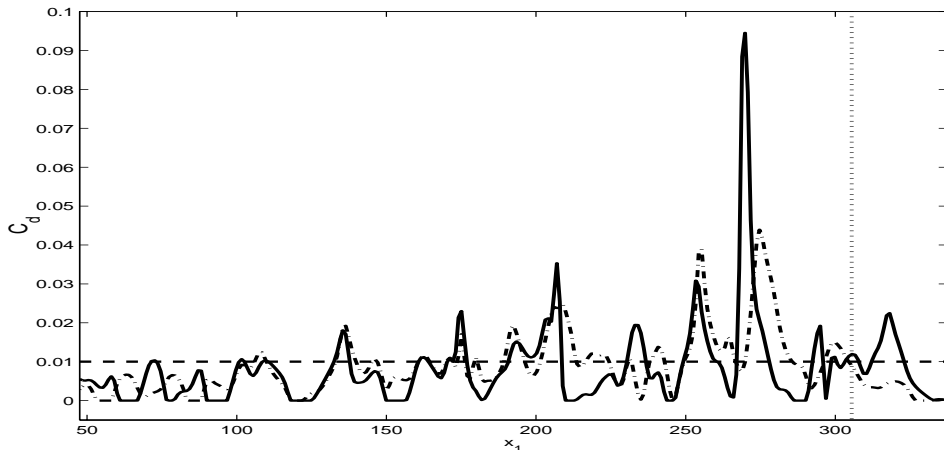
Figure 5.4: Centerplane value ($x_2 = -3$) of C_d as a function of x_1 for the dynamic eddy viscosity model (—), dynamic mixed model ($-\cdot$) and the value of C_S^2 for the Smagorinsky model ($--$) at time $t = 935$.

In order to further explore the differences in the models, we next discuss the streamwise momentum flux. It can be split in a convective, viscous and subgrid contribution. The convective flux is by far the largest. For all models the convective flux is at least a factor of forty larger than the viscous and subgrid fluxes. The latter two are roughly comparable in size at the present Reynolds number. The viscous flux for the Bardina model and the case without model is about a factor of two larger than that of the other models. This can be explained from the fact that the subgrid dissipation is smaller. As a result, more small structures are present. Also the convective fluxes of these two models are about thirty percent larger than those of the other models. This is also reflected in Figure 5.3 since the largest amplitude of fluctuations of the streamwise momentum density signal was reported for the no-model and Bardina model.

5.4.2   Features of subgrid-models

Up to now we have compared the instantaneous flow for some subgrid-models considering several quantities like the spanwise vorticity and the streamwise momentum density. In this subsection we show the dynamic behaviour of the eddy viscosity model and the energy transfer in the non-eddy viscosity models by considering the forward and backscatter.

We start with the eddy viscosity coefficient. In the dynamic models, this coefficient depends on the local turbulent structure of the flow. In Figure 5.4 we display the instantaneous value of the coefficient close to the centerplane for both dynamic models while it is generally too low further downstream.

The buffer area is behind the dotted line. Both values of C_d globally increase in streamwise direction which indicates that the flow becomes more turbulent. We also mention that in the first quarter of the domain the Smagorinsky value of $C_S^2 = 0.01$ is larger than the dynamic coefficient of both dynamic models while it is generally too low further downstream.

Next we focus on the dynamic coefficient in relation to the artificial way to keep it non-negative. In the first half of the domain the dynamic eddy viscosity model contribution is clipped twice as often as in the second half. This difference is even larger for the dynamic mixed model. We also observed a low correlation between the solutions of the dynamic eddy viscosity model and the Smagorinsky model and a high correlation between the dynamic eddy viscosity model and no-model solutions. In contrast with the temporal mixing layer simulation, the dynamic coefficient is averaged over the homogeneous spanwise direction only. This explains why its behaviour is less smooth in the spatial setting. This behaviour of the dynamic coefficient may be improved by an additional averaging over time which is somewhat comparable to averaging over the streamwise direction in the temporal setting. We return to this in the next chapter.

Next, we consider the two non eddy viscosity models used here: the Bardina model and dynamic mixed model. We focus on the production term of the turbulence kinetic energy equation:

$$P = -\bar{\rho}\tau_{ij} \ \partial_j \tilde{u}_i.$$

It represents the rate at which kinetic energy is transferred between the mean flow and the small scales. It corresponds with the expression from equation (3.3) of the RaNS setting with the exception that the bar-filter here denotes spatial filtering. For the RaNS setting of the previous chapter we found that in a local sense as well as after integration in the normal direction, the production had the largest contribution in the turbulence kinetic energy equation.

Following refs. [69, 99], the production term is decomposed into two parts $P = P_+ + P_-$, with:

$$P_+ = (P + |P|)/2 \ \geq 0, \text{ (forward scatter)},$$
$$P_- = (P - |P|)/2 \ \leq 0, \text{ (backscatter)}.$$

In regions of the flow where P (and P_+) is positive, energy flows from the resolved scales to subgrid scales and the amount of turbulence kinetic energy is increased which results in higher levels of turbulence. Contrary, negative values of P (and P_-) imply a transfer of energy in reverse direction and correspond to a decrease of turbulence kinetic energy. If the turbulent stress tensor $\bar{\rho}\tau_{ij}$ is modeled by an eddy viscosity model, the production cannot be negative.

So, the Smagorinsky and dynamic eddy viscosity model only generate forward scatter.

In Figure 5.5 we show the back- and forward scatter for the Bardina and dynamic mixed model at $t = 935$ as a function of x_1 and averaged over x_2 and x_3. Both models display considerable forward scatter which on average is about a factor five respectively twelve larger than the amount of backscatter. We observe that both models exhibit backscatter everywhere up to $x_1 = 150$. Further downstream, in particular for the dynamic mixed case, several regions exist with almost zero backscatter. Upstream of $x_1 = 100$ the amount of forward scatter is a factor two to three smaller than downstream. The lower amount of backscatter and to a lesser extent the higher amount of forward scatter imply that further downstream more smaller scales arise. The Bardina model is seen to generate more backscatter than the dynamic mixed model.
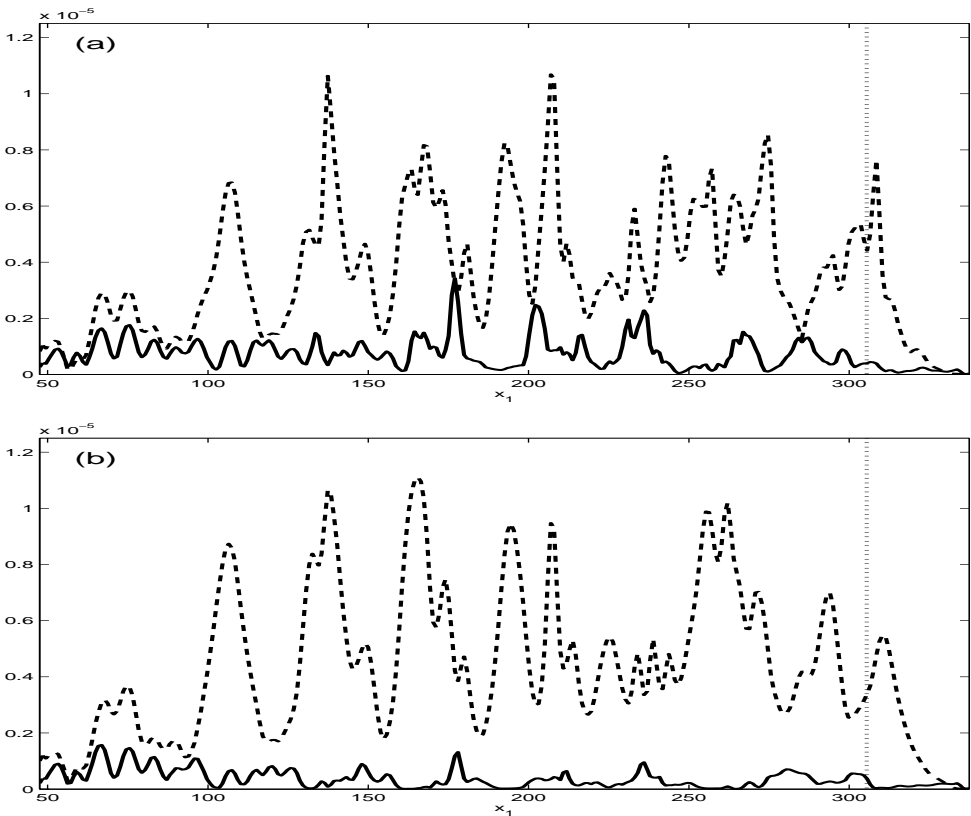

Figure 5.5: Plots of $P = -\bar{\rho}\tau_{ij}\,\partial_j\tilde{u}_i$ at $t = 935$ as a function of x_1 and averaged over x_2 and x_3. The amounts of backscatter $|P_-| = -P_-$ (—) and forward scatter $|P_+| = P_+$ (− −) are shown for the Bardina (a) and dynamic mixed model (b).

Finally we focus on the production of the Bardina model. We are interested in a possible correlation between locations of back- and forward scatter, *i.e.*, negative and positive production respectively, in relation to the spanwise vorticity. In Figure 5.6 the contour plot of $P = -\bar{\rho}\tau_{ij}\partial_j\tilde{u}_i$ at $t = 935$ is shown. Regions of backward- and forward scatter form a regular pattern in the laminar region up to x_1=110. The white regions (backscatter) remain about the same size while the dark areas (forward scatter) globally become wider in downstream direction. Furthermore we observe that the first half of the streamwise domain contains much larger regions of backscatter than the second half. The dark regions globally coincide with negative peaks of the spanwise vorticity. This agrees with results of the study from [42] on homogeneous isotropic turbulence. In this work, the coherent vortical structures that are responsible for the energy transfer between the grid scale and the subgrid scales are classified. Events associated with backscatter occur along 'compressed vortex tubes' cf. [42]. The equivalent structures in the present mixing layer configuration appear to be the negative vortex rollers. In the next section we consider results based on long-time statistics to complement the instantaneous flow results discussed until now.

5.4.3   Comparison of mean and fluctuating LES predictions

Up to now we have compared the instantaneous behaviour of the subgridmodels. Here we consider results from long time-sampling. All statistical
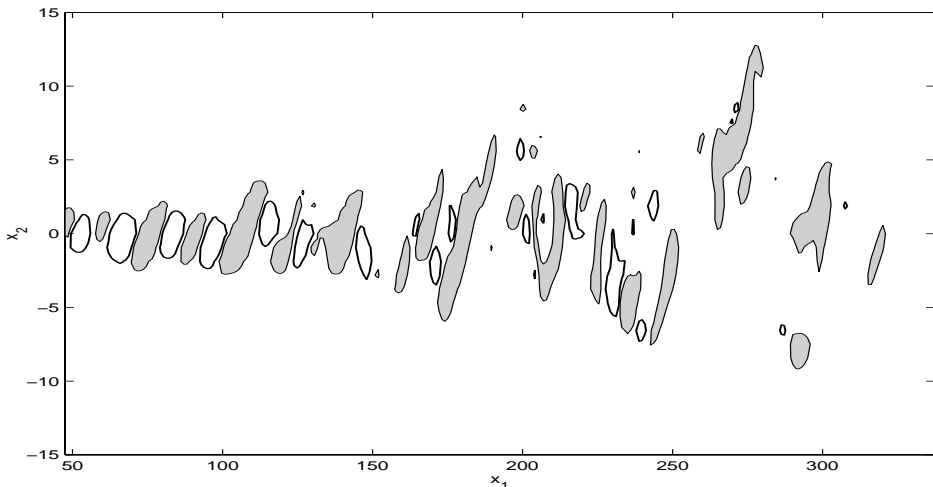

Figure 5.6: Contour plot of $P = -\bar{\rho}\tau_{ij}\partial_j\tilde{u}_i$ at $t = 935$ for values $P = 0.000025$ (dark spots; forward scatter) and $P = -0.000025$ (white spots; backscatter) for $x_3 = -L_3/2$. We have x_1 as the horizontal and x_2 as the vertical axis.

averaging is based on results from the time interval $[935, 3231]$. After $t = 935$, extra effects, that may be present as a result of initiating the LES from a filtered turbulent DNS field, appear to have disappeared. We start with the momentum thickness. In Figure 5.7 we collected the momentum thickness predictions of the different subgrid-models. A short distance behind the inflow boundary, the results of all subgrid-models display an increase in the growth rate around $x_1 = 100$ which is indicative of transition. The values for the growth rates approximately remain roughly unchanged in the rest of the streamwise domain. The largest deviation between the momentum thicknesses is about 30%. The deviation between the resulting growth rates is within 20%. Similar as for the spanwise vorticity, the differences among the momentum thicknesses of all subgrid-models is small compared to the deviations in the coarse-grid temporal study. This can be explained by the better resolution in the present setting. The momentum thickness is largest for the filtered
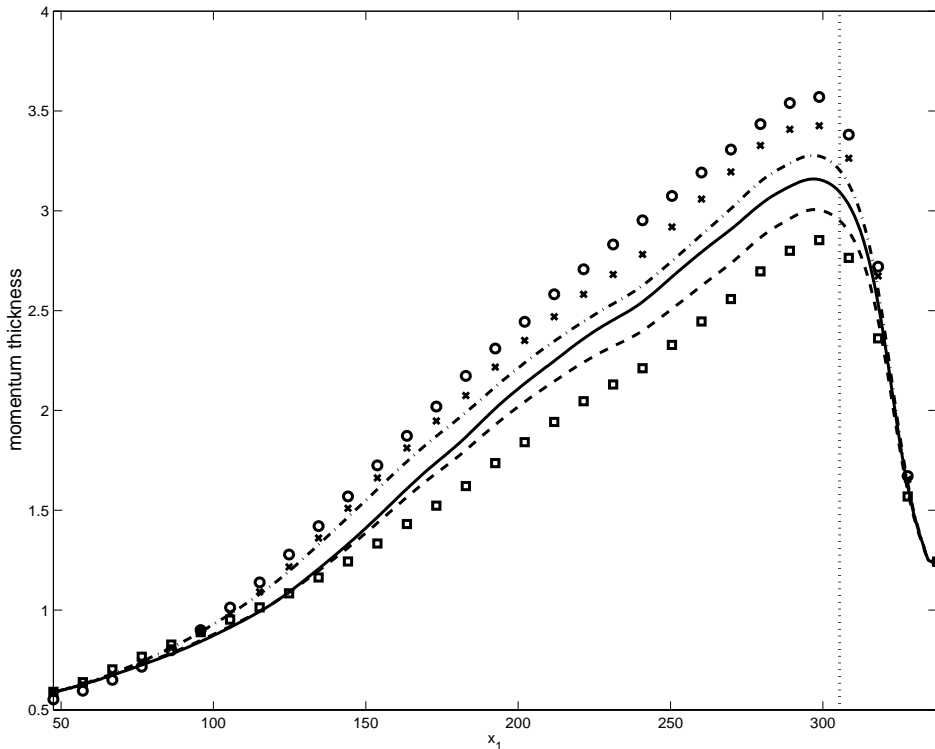

Figure 5.7: Momentum thicknesses θ as a function of x_1 and based on time=935-3231. The models used are Smagorinsky ($\square$), Bardina ($\times$), dynamic eddy viscosity ($--$), dynamic mixed ($-\cdot$). Also the no-model ($-$) and filtered DNS (o) results are included.

DNS result, followed by that of the Bardina and dynamic mixed model. The no-model and dynamic eddy viscosity results coincide for small values of x_1 and split further downstream where the no-model result grows slightly faster. The growth rate of the Smagorinsky model is lowest, but closer to that of the others than in the temporal setting, due to the lower Smagorinsky constant adopted here.

We next consider the profiles of the time-averaged streamwise momentum density $\langle \overline{\rho u}_1 \rangle$. As can be seen in Figure 5.8.a, the lines more or less coincide around the centerplane. However, the values near the 'edges', *i.e.*, around $x_2 = -8$ and 6, are different for each subgrid-model. If the normal coordinate in Figure 5.8.a is scaled with the predicted local momentum thickness, all lines nearly coincide with data taken from the second half of the domain. This scaling of the normal coordinate is also necessary in order to consider self-similarity in the averaged streamwise momentum density profiles of all
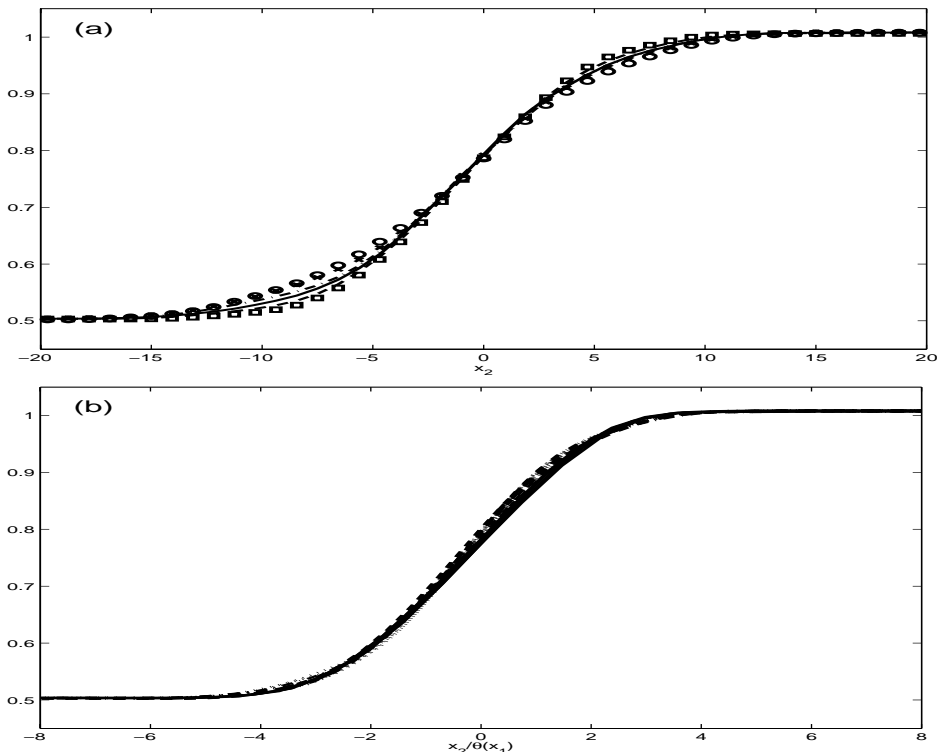
Figure 5.8: Time-averaged streamwise momentum density $\langle \overline{\rho u}_1 \rangle$ at $x_1 = 279$ as a function of x_2 (a). The models used are Smagorinsky ($\square$), Bardina ($\times$), dynamic eddy viscosity ($--$), dynamic mixed ($-\cdot$). Also the no-model (---) and filtered DNS (o) results are included. In (b), it is displayed at x_1 values 148(---), 192($--$), 235($-\cdot$) and 279($\cdots$) as a function of $x_2/\theta(x_1)$ for all four LES models.

four subgrid-models. In Figure 5.8.b we collected the resulting profiles of all subgrid-models at four locations in the second half of the streamwise domain. Considered for each model separately, the deviation between the profiles at four different streamwise locations is within 3%. So, within this accuracy, all models predict self-similarity of the averaged streamwise momentum density consistent with the DNS results in Chapter 2. Similarly as in Figure 5.8.a, the values of the slope around the centerplane are close to each other. The largest deviations again take place at the 'edges' of the mixing layer. Even when we also incorporate the no-model and filtered DNS results, the deviations between all profiles are within 4%. Hence $\langle \overline{\rho u}_1 \rangle$ does not depend sensitively on simulation details such as the subgrid-model. The self-similar behaviour of $\langle \overline{\rho u}_1 \rangle$ is evident from these simulations and at this level of accuracy.

Next, we turn to the Reynolds stress profiles that in Chapter 2 turned out to be rather sensitive regarding resolution, length of time-averaging and type of inflow perturbations. In Figure 5.9 we collect the three turbulence intensities $R_{ii}^{1/2}$ ($i = 1, 2, 3$) and the Reynolds stress R_{12} based on definition (5.17). The filtered DNS result (5.16) is also included. It should be stressed here that $\langle \bar{\rho}\tau_{ij} \rangle$ from (5.15) is not included in the LES predictions of the Reynolds stress. This term usually is not contained in either a DNS or the LES database. We consider this issue momentarily.

The difference between the profiles of all subgrid-models is smallest for the R_{12} component, followed by R_{11}. For R_{11} and R_{12}, the filtered DNS profile bends slightly down to the low-speed side, *i.e.*, the profile has its peak at $x_2 < 0$. This behaviour is not clearly observed in the LES results. The results for R_{22} vary more and the filtered DNS result is overestimated by all LES predictions. For R_{33} the filtered DNS result is underestimated by all LES predictions. Also the widths of these profiles vary. This could be improved by plotting R_{33} as a function of $x_2/\theta(x_1)$ instead of x_2, but the widths of for example the R_{22} profiles would then no longer coincide. The relatively large deviations in the peak values of the LES results for R_{33} may decrease when we remove the physical constraint of a narrow spanwise domain, *i.e.*, no longer restrict to the 'minimal mixing layer'. This is further explored in Chapter 6.

The Smagorinsky and dynamic eddy viscosity Reynolds stress tensors are close to each other except for the streamwise turbulence intensity where the peak of the dynamic eddy viscosity model prediction approaches the higher filtered DNS result. The Reynolds stress tensor of the no-model setting is almost always larger than the predictions of the other models. To a lesser degree this can also be concluded for the Bardina and dynamic mixed model results for the Reynolds stress tensor which is indicative of the amount of small scales in the LES predicted flow. The Smagorinsky results which almost always are lowest show this model's too dissipative character.
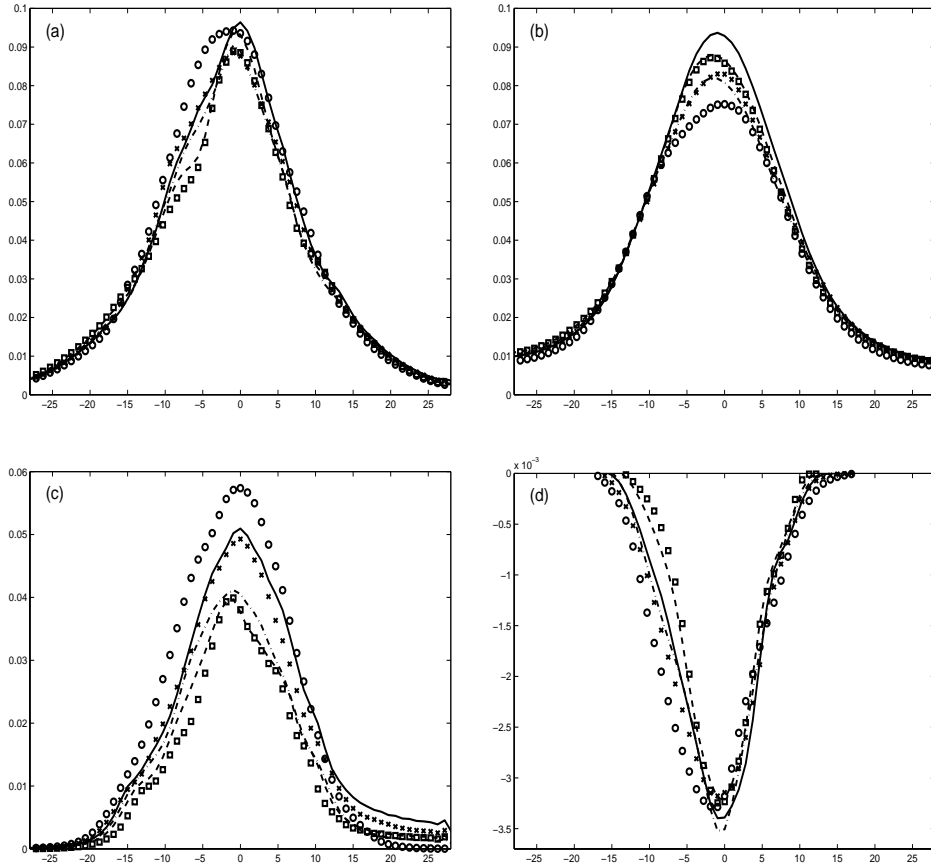
Figure 5.9: Components of the turbulence intensities $R_{ii}^{1/2}$ (i=1-3;a-c) and Reynolds stress R_{12} (d) at x_1=279 as a function of the normal coordinate x_2. The models used are Smagorinsky ($\square$), Bardina ($\times$), dynamic eddy viscosity ($--$), dynamic mixed ($-\cdot$). Also the no-model ($-$) and filtered DNS (o) results are included.

Finally we return to the issue of the term $\langle \bar{\rho}\tau_{ij} \rangle$ (see (5.18)) that should be added to the LES Reynolds stress components in order to compare them with the filtered DNS values. This term will be estimated using about forty snapshots of $\bar{\rho}\tau_{ij}$ from the DNS data. An alternative is to employ a model approximation, $\langle m_{ij} \rangle$, which is sampled during the LES. We choose the Bardina value of $\langle m_{ij} \rangle$ [104]. It turns out that the streamwise developments of $\langle \bar{\rho}\tau_{ij} \rangle$, based on several snapshots, and $\langle m_{ij} \rangle$ give about equal peak values. These should be added to the LES predictions of R_{ij}. The change in the prediction of the Reynolds stress tensor is next discussed for each component separately. The sign of $\langle \bar{\rho}\tau_{ij} \rangle$ (and $\langle m_{ij} \rangle$) is equal to the sign of R_{ij} for all components.

From one third of the domain onward, the maximum value of tensor

$\langle \bar{\rho} \tau_{ij} \rangle$ (and $\langle m_{ij} \rangle$) saturates for all components. We focus on the situation at the streamwise location used in Figure 5.9 ($x_1 = 279$). The first component suggests that the maximum filtered DNS value of R_{11} should be decreased by 8%. So, the no-model result gets even worse while the others come closer to the filtered DNS profile. Likewise, an amount of 5% should be subtracted from the peak value of R_{22}, so all model predictions get somewhat worse. For the third component, R_{33}, all LES predictions of the peak value are improved by a decrease of 12% for the filtered DNS. Finally, 12% should be added to the peak value of the filtered DNS prediction of the Reynolds stress R_{12}, which improves all models except the no-model and dynamic mixed model. It is concluded that the main findings from the Reynolds stress tensor are not influenced by the inclusion of this extra $\langle \bar{\rho} \tau_{ij} \rangle$ term.

Throughout this section we have encountered and discussed several quantities. The results for the four subgrid-models are summarized in Table 5.1. The quality of LES is determined by comparison with filtered DNS results. A subgrid-model is assessed relative to the no-model performance. The table is next discussed and compared against a similar table based on the temporal results. First we remark that the distinction in performance of the models is smaller for the present results. This can be attributed to the higher resolution. The similarity basis of the Bardina model - compared to the other subgrid-models - predicts an improvement of the modeled subgrid stress when the resolution is increased. This explains the better performance of the Bardina model for the present setting compared to [104]. The dynamic mixed model is better than the dynamic eddy viscosity model. The improvement in the LES using the dynamic models is smaller compared to the temporal study.

	Figure	S	B	D	M
vorticity in a plane	5.1	0	0	+	+
maximum vorticity	5.2	0	0	+	0
momentum thickness	5.7	−	+	−	+
R_{11}	5.9.a	0	0	0	0
R_{22}	5.9.b	+	+	+	+
R_{33}	5.9.c	−	0	−	−
R_{12}	5.9.d	−	0	−	−

Table 5.1: Summary of the results from the Smagorinsky (S), Bardina (B), dynamic eddy viscosity (D) and dynamic mixed (M) setting. The symbols −, 0 and + refer to bad, reasonable and good results, respectively.

This may be related to the narrow spanwise domain that confines the present setting and the higher resolution, which makes this LES comparison less demanding than in [104]. The better performance of the present Smagorinsky model can be attributed to the lower value for the Smagorinsky constant. This reduces the model's excessive dissipation. In the next section we consider the influence of the numerical method on LES predictions. We mainly focus on resolution effects.

5.5   Implementation sensitivity

The LES results that were shown and discussed in the previous section were based on the choices of the resolution and the inflow and initial conditions described in Section 5.3.1. In this section we vary some of these parameters to consider the sensitivity of the predictions. The main motivation behind LES involves its application in complex flows. In practice, the complexity of the mixing layer that can be considered is limited by the resolution of the numerical simulation. Thus, the main aim of this section is to determine a 'minimal' resolution that is required for a numerical simulation to still contain the typical features of a mixing layer. These features are, *e.g.*, the momentum thickness and Reynolds stress tensor.

In this section we describe results of large-eddy simulations where we take only half the number of points in each direction: $(N_1, N_2, N_3) = (150, 32, 8)$. These simulations are about a factor of ten faster. A decrease of the resolution has numerous effects. Several of these effects simultaneously involve the boundaries of the computational domain.

First we focus on numerical effects that have an origin at the outflow boundary. Based on the DNS findings at three different resolutions (see Figure 2.7.b), the momentum thickness is considered as a very stable quantity regarding changes in resolution. For the present lower LES resolution, small fluctuations are visible in the momentum thickness close to the inflow boundary. A striking improvement is observed when taking $N_1 = 180$ instead of 150. These fluctuations also are reduced when the buffer length is doubled, while the mesh size is retained. When the streamwise mesh size h_1 is too large, the damping function changes too abruptly. Hence, fluctuations are reflected and become visible, *e.g.*, near the inflow area. We remark that this phenomenon was also found for a DNS at the same resolution. When the number of streamwise points is further increased from $N_1 = 180$ to 300, hardly no difference is visible. Therefore, in the rest of this section the 'low resolution' refers to $(N_1, N_2, N_3) = (180, 32, 8)$.

When the resolution increases in all directions and also the filter width gets proportionally smaller, the filtered value should approach the unfiltered

value. However, for a low resolution a difference is clearly present, especially around the inflow boundary where the mixing layer is rather thin. At the inflow boundary, a very small number of points in x_2-direction covers the mean streamwise velocity profile. The slope of this profile changes after filtering. At the first point after the inflow boundary the filtered equations are solved. In order to retain the consistency of the system that is solved, the perturbations imposed at the inflow have been filtered over x_2 and x_3 as well.

The difference between LES results that employ filtered or unfiltered initial field and inflow perturbations is clearly visible in the dynamic coefficient. However, when the variables are not filtered at the inflow boundary, there is a strong increase in the dynamic coefficient of the dynamic mixed model. This behaviour is no longer present when filtering over x_2 and x_3. Especially, in x_2-direction the perturbation profiles are narrow and therefore it appears that the main difference can be attributed to the filtering in x_2-direction. On the other hand, the dynamic coefficient for the dynamic eddy viscosity model does not depend much on whether the perturbations are filtered or not. It is unclear why filtering the imposed inflow variables has a much larger effect for the dynamic mixed model than for the dynamic eddy viscosity model.

Finally, we discuss the effect of filtering the inflow and initial conditions on the momentum thickness. The difference between filtered and unfiltered fields becomes larger for a coarser resolution. In Figure 5.10 we have collected momentum thicknesses of LES using the dynamic eddy viscosity model that employed both filtered and unfiltered initial and inflow conditions. The LES is performed at the high resolution of Section 5.4 with $N_1 = 300$. Both LES results in Figure 5.10 display an equal growth rate. However, the 'filtered inflow' result needs a somewhat longer streamwise distance after the inflow to develop a linear growth. Also both the filtered and unfiltered DNS results are included. Filtering the DNS results only has a clear effect around the inflow boundary. We note that at the inflow boundary the results of the DNS and LES employing unfiltered conditions coincide. Also their filtered equivalents are close to each other.

Also other effects appear when a coarser grid is employed. We describe and study some characteristics. The Bardina LES becomes unstable around $t = 3000$. We recall that the feasibility of simulations of realistic mixing layers is the final goal of this study. These simulations involve a higher Reynolds number than used here and the Bardina LES may become unstable, even when a smaller mesh size is used. For all models, similarly as in the temporal study, the behaviour around the peaks of the Reynolds stress tensor profiles is no longer smooth. The Smagorinsky profile is a factor two to three lower than the one from the dynamic eddy viscosity model which in turn almost coincides with the no-model result. The peak of the R_{33} LES profile of the Bardina result is only 20% of the filtered DNS level and even 10% for the
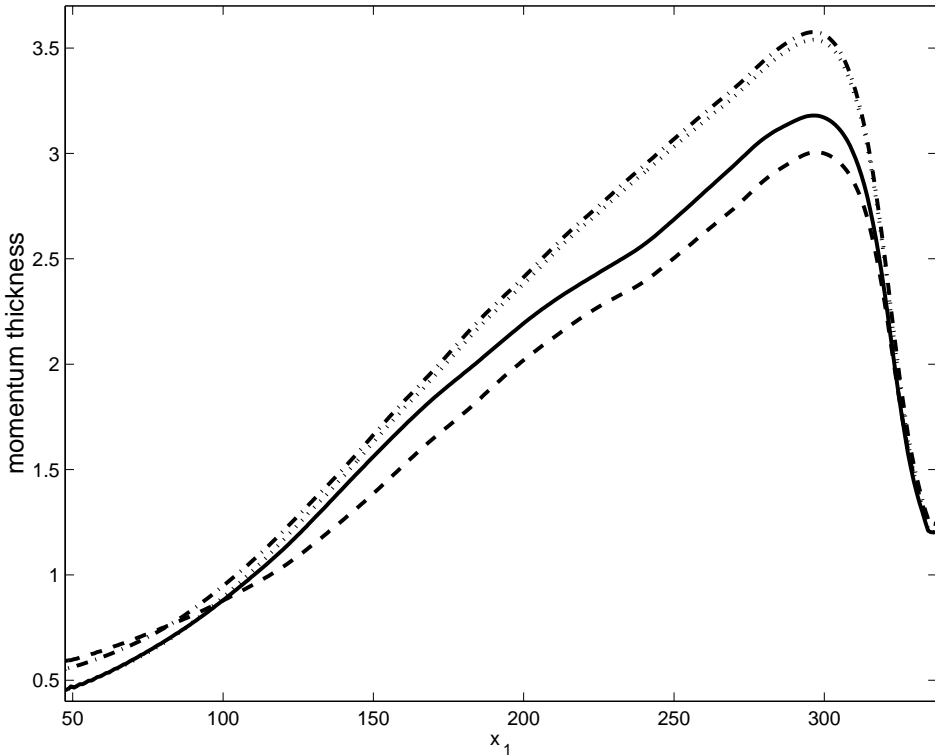
Figure 5.10: Momentum thicknesses θ as a function of x_1 and based on the fine-resolution LES results with time=765-3231. The dynamic eddy viscosity results for unfiltered (—) and filtered (−−) inflow and initial conditions and the fine-resolution filtered (−·) and unfiltered (· · ·) DNS results are plotted as a function of x_1.

other models. So, the fluctuations of the spanwise velocity are small in the coarse-grid LES. The spreading in the LES results for all components of the Reynolds stress tensor is large compared to the previous section.

We recall that the peak level of R_{33} for the high-resolution LES is lower than that of the DNS. It is observed that the peak value of R_{33} from the coarser LES is even lower. In contrast, the R_{33} results of the temporal setting with a wider domain do not display larger deviations between the LES and filtered DNS than of the other components. In the next chapter we observe that the present underprediction of spanwise turbulence intensity is indeed improved by enlarging the spanwise extent. This establishes that not only the resolution but also the 'geometric parameters', which define the simulation domain, can have a large influence on the results.

5.6   Conclusions

The main theme of this chapter was the selection of an appropriate configuration, *i.e.*, subgrid-model and resolution. In general, it can be inferred that no unambiguous distinction can be made regarding the quality of the subgrid-models studied here. On the other hand, the lower resolution simulations resulted in various simultaneous effects that also involved the inflow and outflow boundary of the domain. As a result, it is not completely clear whether the distinctions in the LES results have a numerical origin in the sense of the resolution being too low or whether they account for differences in the subgrid-models.

Several Smagorinsky predictions like the spanwise vorticity, streamwise momentum density and most components of the Reynolds stress tensor display the presence of too much dissipation, despite the low Smagorinsky constant of 0.1. However, the Smagorinsky results for the maximum spanwise vorticity and some Reynolds stress tensor components are close to those of the dynamic eddy viscosity model. Both the Bardina and no-model result contain an excessive amount of small scales. This results in an overprediction of several quantities like the spanwise vorticity and root mean square of the streamwise momentum density. The subgrid dissipation was either not present or insufficient and resulted in a larger amount of small scales. The deviations between the present filtered DNS and no-model result are larger than the other model predictions for several quantities like the spanwise vorticity and normal turbulence intensity. The incorporation of a subgrid-model generally improves the results. The Bardina model performs best for several statistical quantities like the momentum thickness and Reynolds stress tensor. However, the low-resolution LES became unstable. Previously, LES is introduced for the simulation of complex mixing layers with high Reynolds number and at low resolution. We therefore do not select the Bardina model.

The two models that remain as candidates for the feasibility study in a more realistic setting both employ the dynamic procedure. Although for some quantities the results of the dynamic mixed and eddy viscosity model can be distinguished, the overall performance of both models is about the same. Based on simulation results of the temporal mixing layer at low as well as high Reynolds numbers [104], and the fact that the dynamic eddy viscosity model is computationally much less expensive, we propose to use the dynamic eddy viscosity model in Chapter 6.

In the next chapter, large-eddy simulations are performed of more realistic mixing layers. This involves simulations in a larger stream- and spanwise domain, as well as at a higher Reynolds number. There are some reasons to assume that in particular the narrow domain constraint used up to now has been a restrictive factor in the simulations. This is primarily based on results

for the Reynolds stress tensor. We expect an increase in the level of spanwise fluctuations when the spanwise domain is enlarged. This will be one of the topics explored in the next chapter.

Chapter 6

Towards LES of realistic mixing layers

In this chapter we consider large-eddy simulations of realistic mixing layers. Compared to DNS, LES should be able to simulate flows in a larger domain and at a substantially higher Reynolds number at the same computational cost. The main topic of this chapter is to investigate this. We start with considering a wider and longer computational domain. Next the effects of a higher Reynolds number are investigated, in particular the effects on the momentum thickness, Reynolds stress tensor, dynamic coefficient and vorticity. Finally a variant of the dynamic eddy viscosity model for the spatial simulation of statistically stationary flows is tested. It employs time-averaging of the dynamic coefficient and may no longer need the presence of a homogeneous direction in space.

We also study the issues of self-similarity and three-dimensionality. The common opinion is that turbulent mixing layers display self-similar behaviour, provided the Reynolds number is high, the computational domain is large and the simulation is sampled long enough in time. For the minimal mixing layer setting employed up to now we found that the momentum thickness grows linearly in downstream direction for quite some streamwise distance. Also the deviations in the profiles of averaged streamwise velocity as a function of the normalized normal coordinate are within one percent. Finally it was found that only the streamwise turbulence intensity clearly displays signs of self-similarity in the final part of the streamwise domain. So, a key question in this chapter is whether self-similarity comes into the system more clearly when the computational domain is enlarged. In the study described in [21], a larger amount of three-dimensional structures is observed when the spanwise domain length is enlarged. So, it is interesting to consider whether more three-dimensionality comes into the simulation when the constraint of a narrow

spanwise domain is removed.

We next review some numerical results from literature on mixing layers at different Reynolds numbers and with different sizes of the computational domain. In [4] and [21] it is found that the growth rate of a temporal and spatial mixing layer increases if a larger spanwise domain is used. A larger streamwise domain hardly affects the growth rate. Also the Reynolds stress tensor was influenced by the wider domain. In the temporal mixing layer study from [104] the computational domain was also doubled in all directions, the Reynolds number was increased by a factor of ten and uniform noise instead of LST perturbations was added to the mean flow in order to provide the initial condition. The combination of these changes resulted in a reduction in growth rate of thirty percent. It is not clear to which particular item this reduction can be attributed.

The main theme of this thesis is the feasibility of numerical simulation of a realistic turbulent mixing layer. In practical applications not only the domain is large, but also the Reynolds number. This leads to more small-scale structures and hence affects the necessary resolution of the simulation. In Chapter 5 it was argued that the dynamic eddy viscosity model is well suited for the purpose of the present chapter. The main idea of this model is based on a dynamic coefficient that locally adapts to the state of the flow. In the final part of this chapter, we focus on this dynamic coefficient. In temporal simulations the dynamic coefficient is constant in homogeneous directions, *e.g.*, the streamwise and spanwise direction for the mixing layer. Up to now, we used a time-dependent dynamic coefficient. In Chapter 5 it was shown that this results in a highly fluctuating coefficient in streamwise direction. We therefore study a variant of the dynamic eddy viscosity model where the dynamic coefficient is no longer determined locally (with respect to time and space) but instead is also averaged over time.

This chapter is organized as follows. In Section 6.1 we give a specification of the simulations used in this chapter. Each time we subsequently employ a new setting, we show results that change significantly with respect to the 'previous' case, gradually building up the complexity of the simulations. Results that typically change when LES is performed on a wider and longer domain are shown in Section 6.2. Next, in Section 6.3, results are shown that change significantly when the LES is performed at a higher Reynolds number. This is followed by Section 6.4 where we focus on the behaviour of the dynamic coefficient. Based on this, the adapted subgrid-model introduced above is formulated. The results are evaluated and discussed. Finally we give the conclusions in Section 6.5. The study described in this thesis is completed with Section 6.6 in which a number of recommendations for future research are pointed out.

6.1 Specification of the large-eddy simulations

In this section we describe the choices that were made concerning all simulations that are discussed in this chapter. The simulations are performed using spanwise symmetry. As a first step in exploring the effect of the constraints introduced before, we increase the extension of the spanwise domain. Before, we had $L_3 = \lambda_F$ and here we take $L_3 = 5 \lambda_F$. Further studies with other spanwise lengths should be done in order to investigate the specific influence of taking $L_3 = 5 \lambda_F$ instead of, *e.g.*, four or six times the fundamental wavelength.

Up to now, we only used spanwise perturbation modes with spanwise wavelengths equal to λ_F. For the extended spanwise domain, also modes with larger spanwise wavelengths should be included in order to stimulate the spanwise interaction of structures. Four extra $3D$ modes are employed with spanwise wavelengths equal to $5/3 \lambda_F$ and $5 \lambda_F$ respectively. Following [104], we select globally the same wavelengths for the streamwise modes. The corresponding streamwise wavelengths are taken as $2 \lambda_F$ and $4 \lambda_F$. So, the streamwise wavelengths all coincide with those of the three $2D$ modes: the fundamental with wavelength λ_F, first subharmonic with λ_{S1} and the second subharmonic with λ_{S2}. This choice is based on the idea that these multiple wavelengths stimulate subsequent pairings of the two-dimensional rollers. As a result, also the temporal period of all perturbations is a multiple of T_F. The resulting thirteen modes have relative amplitudes 0.03 and 0.091 for the three $2D$ modes and ten $3D$ modes respectively. All relative amplitudes together add up to one and the absolute amplitude ϵ is taken as 0.2 (see Section 2.2.1).

The specifications of the LESs that we study in this chapter are given in Table 6.1. For convenience we introduce the following notation:

S : small domain and Reynolds number (see Chapter 5)

W : wider domain

WL : wider and longer domain

WLR : wider and longer domain as well as a higher Reynolds number

WC_m : wider domain and time-averaged C_d

From top to bottom, each next situation involves the removal of one constraint with respect to the former case. The grid spacings in all three directions and for all settings are between 0.8 and 1.0. The filter width equals twice the grid size in all three directions for all situations. New modes were derived from linear stability theory for WLR which employs a ten times higher Reynolds number. Accordingly, also the spanwise domain length and spanwise grid size change slightly. The buffer length for the longer streamwise domain is taken equal to $4 \lambda_F$. This corresponds to the recommendation that the buffer length

setting	N_1	N_2	N_3	L_1	L_2	L_3	Re
S	300	64	16	290	60	$16.07 = \lambda_F$	200
$W(C_m)$	300	128	80	290	120	$80.33 = 5\ \lambda_F$	200
WL	640	128	80	515	120	$80.33 = 5\ \lambda_F$	200
WLR	640	128	80	515	120	$76.35 = 5\ \lambda_F$	2000

Table 6.1: Specifications of resolution, domain dimensions and Reynolds numbers for settings S, W, WC_m, WL and WLR.

X_{e1}	X_{e2}	X_{e3}	X_{e4}	X_{e5}	X_{e6}
52	126	201	275	350	425

Table 6.2: Streamwise locations at which the time history of several flow variables has been recorded.

should be approximately 10% of the streamwise extent [105].

In the previous chapter, the LES started from a turbulent DNS field which was filtered in order to avoid inconsistencies. Throughout the entire LES, also the inflow perturbations were filtered for the same reason. In the present chapter, the initial condition of the LES is the laminar solution to the boundary layer equations. This also allows to study whether and how turbulence arises in the LES. The initial and inflow fields used for the LES are no longer filtered. The inflow location x_i, at which the streamwise computational domain starts, is taken equal to ten times the value used up to now. For the results, this only implies another initial (laminar) mixing layer width in the outflow buffer area. As already discussed at the end of the previous chapter, we solely employ the dynamic eddy viscosity model in the remainder of this thesis. Finally we mention that the Reynolds stress tensor in this chapter refers to $R_{ij} = \langle \overline{\rho u}_i\ \overline{\rho u}_j / \bar{\rho} \rangle - \langle \overline{\rho u}_i \rangle \langle \overline{\rho u}_j \rangle / \langle \bar{\rho} \rangle$ according to eq. (5.17).

In order to be able to compare the results for all settings mentioned above, we employ the coordinate $X_1 = x_1 - x_i$ where x_i refers to the inflow location. For the two long streamwise domain settings, the time histories of the basic filtered flow variables and for example the dynamic coefficient C_d have been recorded at six centerline locations. For convenience, in the rest of this chapter these equidistant locations are denoted by $X_{e1}, \ldots, X_{e6}$ and are specified in Table 6.2. Note that X_{e5} and X_{e6} are only relevant in the longer domain. For a quantity in the turbulent regime it turned out to make not much difference which of the four locations X_{e3} to X_{e6} is taken. In the next section we describe and discuss some results that change significantly when the LES is performed on a wider (and longer) domain compared to the minimal mixing layer used up to now.

6.2 Wider domain

Similarly as in the minimal channel study in [45], the computational domain up to now has been very restricted in spanwise direction. The domain extent for both homogeneous directions in the minimal channel is taken equal to only a single fundamental wavelength. Translated to the present spatial setting, the equivalent would be to perform a simulation on the narrow computational domain used up to now. Here we show results of cases W and WL which involve a wider (and longer) domain than that of the S setting.

We start with the WL case. In Figure 6.1 a sequence is shown of $\overline{\rho u}_1$ time signals for all six evaluation locations X_{e1} to X_{e6}. These locations cover the whole streamwise region. The LES is started from a laminar mixing layer. As illustrated with the dashed line, one can clearly distinguish at which time the inflow perturbation reaches each downstream location. The upper plot shows the situation in the laminar regime. The signal is approximately periodic with period 85 which corresponds to the LST mode with largest period $4\,T_F$. The four times smaller mode with period $T_F = 21$ is hardly visible, similarly as found for the LES results in case S. The next two locations display regular behaviour in time which is alternated with a more complex signal.

Beyond the second half of the domain, *i.e.*, downstream of X_{e4}, the signal is no longer regular in time while its statistics are about independent of the streamwise coordinate X_1 : the irregular fluctuating signals all have about the same mean and standard deviation. This is clear from the lower three plots of
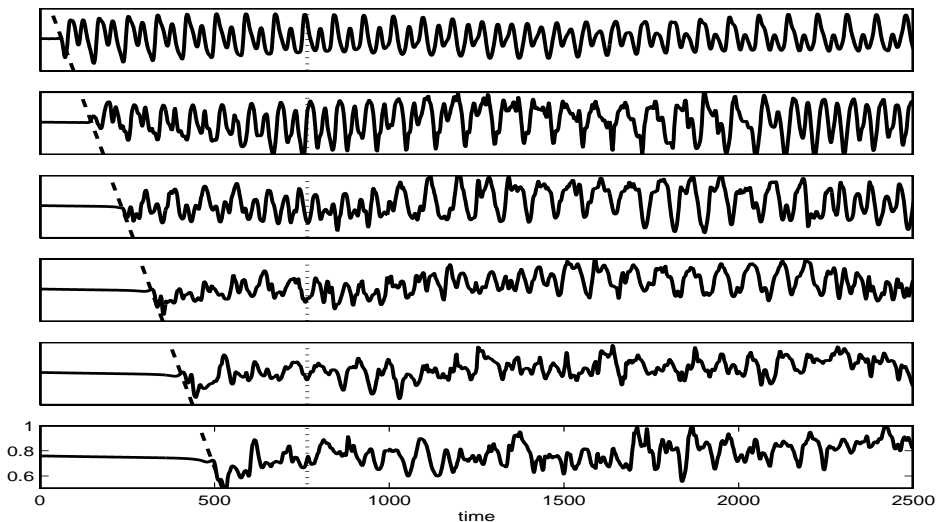

Figure 6.1: Centerline $\overline{\rho u}_1$ as a function of time at streamwise locations $X_{e1} = 52, \ldots, X_{e6} = 425$ (in top-down order) for setting WL.

Figure 6.1. We have put a dotted line at time $t = 765$ at which the statistical sampling starts. The inflow signal has traversed the whole streamwise domain by then.

In order to consider these time history signals in more detail, we compute the spectrum at the two streamwise locations, *i.e.*, X_{e1} and X_{e6}. The results are displayed in Figure 6.2. The spectrum is based on the time interval $[765, 1191]$ which covers 20 T_F. It is plotted against the 'normalized' period T/T_F to consider the spectral contributions with respect to fluctuation period T. The periods of the modes that are perturbed at the inflow boundary are indicated in the figure by T_F, $T_{S1}(= 2 \ T_F)$ and $T_{S2}(= 4 \ T_F)$ respectively. These correspond to the fundamental, the first and second subharmonic modes. The periods of all other modes that are perturbed at the inflow boundary coincide with one of these.

The dominant mode at X_{e1} is the fundamental mode. Both subharmonic modes are important and become dominant when moving downstream to respectively X_{e2} and X_{e3}. According to linear stability theory, the spatial and temporal behaviour in the laminar and transitional region is related by means of the convective velocity [78]. This gives an indication that the first pairing takes place before X_{e2} and the second pairing before X_{e3}. Also, we note that the second subharmonic is the dominant mode for the signals of X_{e3} and all its downstream locations. So, the inflow perturbations turn out to be very persistent. This is a well-known property of mixing layers as already mentioned
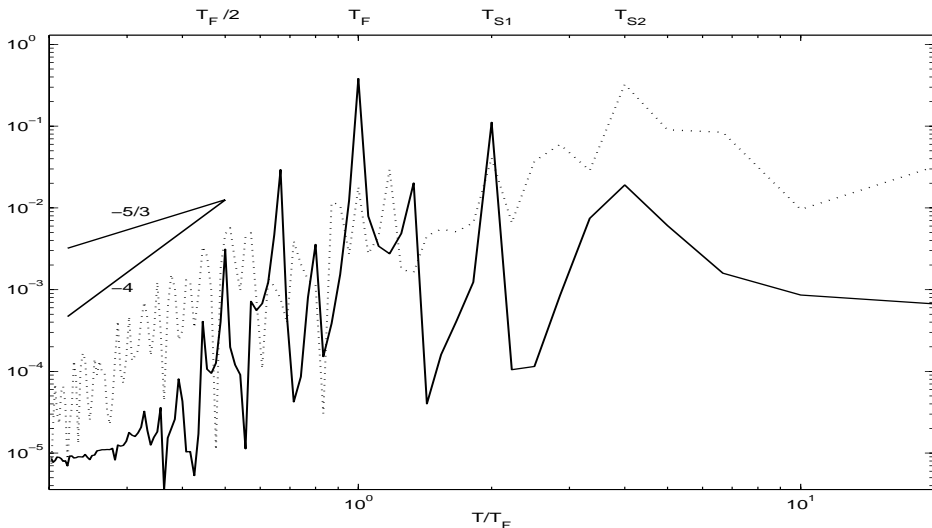

Figure 6.2: Temporal spectrum of the centerline $\overline{\rho u}_1$ signal at X_{e1} (—) and X_{e6} ($\cdots$) as a function of the period of the mode normalized with T_F and based on the signal from $t = 765$ until 1191 for setting WL.

in Chapter 3.

The behaviour of the spectrum tail has some preference for modes with periods 2/3 T_F and 1/2 T_F for X_{e1} while the X_{e6} signal globally has a substantially higher contribution at low T/T_F which displays that much more small scales are present. The tail of the spectrum on the left side of the figure still contains fluctuations which may be due to the fact that the time signal is collected exactly ten times per fundamental period. According to turbulence theories the spatial spectrum of high-Reynolds number homogeneous turbulence may contain an inertial range with slope -5/3. Some studies suggest that this is also valid for the temporal spectrum [34]. We come back to this in the next section. The slope in the tail of the present spectrum behaves as k_t^{-4} (see straight line). For comparison, we also included a line with a -5/3 slope. Finally we remark that the spectrum tail of the X_{e5} signal behaves approximately the same as for X_{e6}.

Next we show some differences between the narrow and wide domain simulations. We first focus on the time development of the instantaneous dynamic coefficient. The dynamic coefficient is only averaged over the homogeneous spanwise direction. It fluctuates as a function of time and the streamwise coordinate. For case W, the spanwise averaging is done over a larger domain. We expect a reduction of the fluctuations for the wider domain LES. Indeed, the standard deviation based on the C_d time signal of all available X_e stations for the W setting is 15 to 45% smaller than for case S. So, the spanwise extension corresponds to a smoother dynamic coefficient. As a result, the C_d signal of S is clipped about five times more for the two downstream locations (X_{e2} and X_{e3}) compared to case W.

As already mentioned in the beginning of this chapter, in the mixing layer study described in [21] a larger amount of three-dimensional structures was observed when the spanwise domain was enlarged. The narrow and wide domain findings regarding the amount of three-dimensional flow patterns are shown in Figure 6.3 for S and W. The streamwise vorticity is suitable to study the three-dimensionality of the flow. Both centerplanes are plotted at equal scales such that the spanwise extent can directly be compared. The LES is started from a laminar mixing layer field independent of x_3 and with zero spanwise velocity. So, initially the streamwise vorticity equals zero. It is clear from the figure that the gradients are higher for W. The extremes in the positive and negative values are approximately a factor two larger for W than for S. So, this supports the idea that more three-dimensionality is present in the mixing layer simulation in the wider domain.

We subsequently show some results that are based on statistical sampling. This is done for the cases S, W and WL that all concern an LES with a low
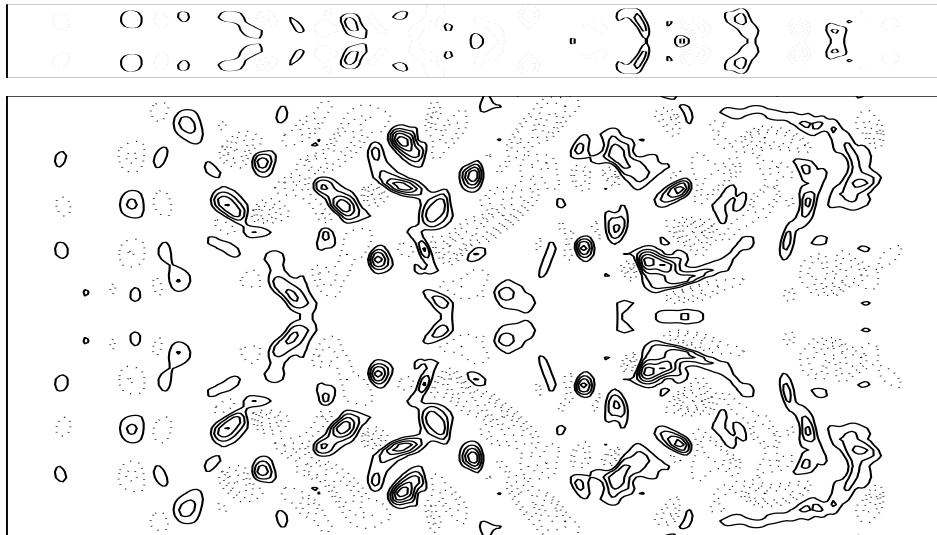
Figure 6.3: Streamwise vorticity at t=3231 for S (upper) and W (lower) in the centerplane $x_2 = 0$. The X_1 is in horizontal direction and the contour levels display negative (——) and positive ($\cdots$) values for $\pm(0.03, 0.06, \ldots, 0.21)$. The domain is duplicated in the spanwise direction in order to give a better visual impression of the flow topology.

Reynolds number. The normalized momentum thickness results are shown in Figure 6.4 and display a larger growth rate for the wider domain LESs in agreement with numerical studies reported in [4] and [21]. The longer domain result of WL displays a long linear growth with the same growth rate as W. The normalized growth rate, α_n, of W and WL equals 0.028 and is approximately 45% larger than the growth rate of S and 35% larger than the DNS value. It is just outside the growth rate interval based on experimental data mentioned in Chapter 3: $[0.014, 0.025]$. However, this interval only takes into account so-called unforced experiments [29]. A slightly higher momentum thickness growth rate (0.029) arises, among others, in the mixing layer experiments of [44]. In the figure, we have included two straight lines with slopes that correspond to growth rates from two experiments [44, 67]. Concluding, both growth rates found for the different LES settings have equivalents in physical experiments. The relatively high value for the growth rate of the wide-box LES suggests a closer connection to the experiment in [44]. A higher value for the growth rate of a wider mixing layer is also found in the numerical studies from [4] and [21]. In [4] it was conjectured that the more highly three-dimensional structures in the larger domain are responsible for the difference in the similarity states (the presence of these structures is less dominant for the
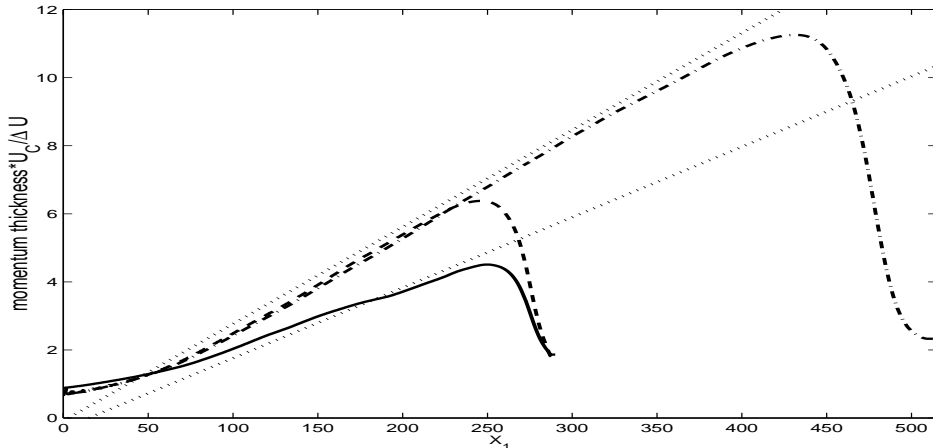
Figure 6.4: Normalized momentum thickness, $\theta\, U_c/\Delta U$, as a function of X_1 for S (—), W (—$-$) and WL (—$\cdot$). The straight lines ($\cdots$) indicate the growth rates of the experiments from [44] (slope 0.029) and [67] (slope 0.021).

smaller domain). Furthermore, in [21] it was found that more helical pairings were present in the wider domain simulation. This appears to correspond to our findings here (see Figure 6.3).

In [10] it appeared that it is particularly important to employ spanwise averaging when considering the development of mixing layers from experiments with different initial and boundary conditions. In this experimental study, it is proposed that some of the discrepancies in the past regarding growth rates and approach to self-similarity may have been caused by the lack of spanwise averaging in experimental studies. Flow visualisation studies have shown that, for mixing layers originating from laminar boundary layers, there is an additional presence of organized streamwise vorticity [51]. The streamwise vorticity structure was found to have a significant effect on the mixing layer mean and turbulence properties [9, 70]. Measurements in the mixing layer originating from turbulent boundary layers have indicated that such large-scale spanwise variations do not occur in this case. The growth rate of the mixing layer based on laminar boundary layers was found to be 20% higher than that based on turbulent boundary layers [9]. Also in [17] the growth rate of the turbulent boundary layer case was smaller than that of the mixing layer originating from a laminar boundary layer. In [10] it was suggested that the layer properties ought to be spanwise averaged in order to adequately study the streamwise evolution of the mixing layer. We again establish the combination of a larger growth rate with the presence of a higher level of streamwise vorticity.

Next we consider the Reynolds stress profiles at a streamwise location in the turbulent regime. In Figure 6.5 we collect all four components from S
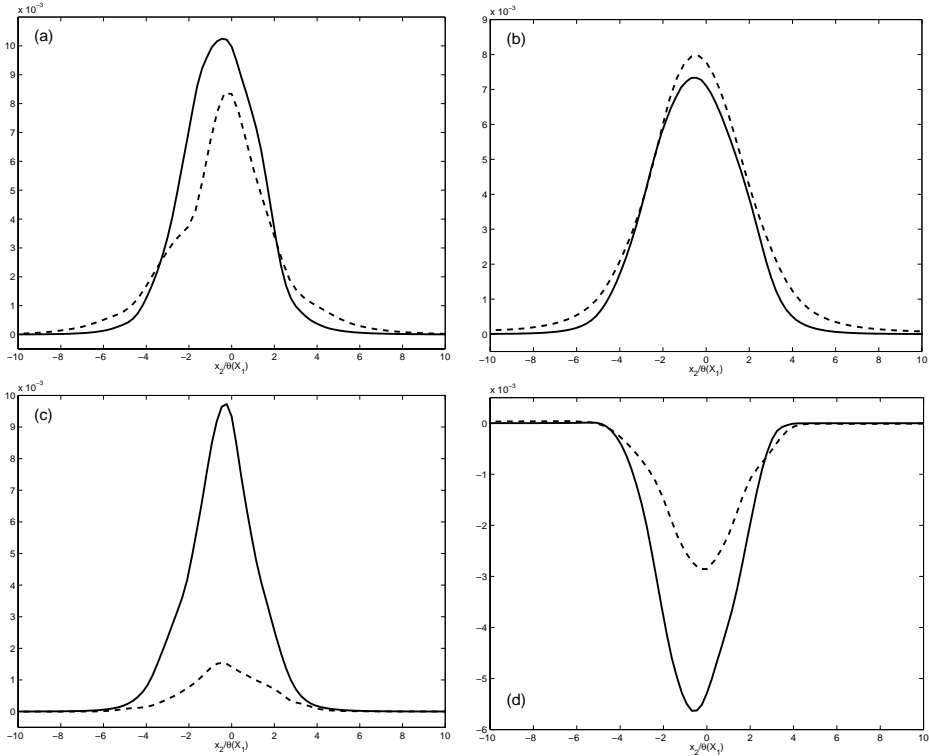
Figure 6.5: Reynolds stress tensor at X_1=225 as a function of the normal coordinate normalized with the momentum thickness for settings W (—) and S $(--)$ for R_{ii} (i=1-3;a-c) and R_{12} (d).

and W. The results of WL are not included since it approximately coincides with the result for W. The R_{33} component is a factor six larger for W than for S. So, taking a wider spanwise domain and extra $3D$ modes strongly affects the fluctuations in spanwise velocity. This is supported by the extra three-dimensional behaviour that comes into the wider mixing layer as shown in Figure 6.3. Also the difference between the R_{12} results is large. Finally we recall from Figures 2.2.b and c that the total amplitude as well as the contribution from the $3D$ modes can make a large difference for the downstream transition process. The self-similarity of the Reynolds stress profiles will be considered further on in Section 6.4.

Finally the findings from this section are compared with two other computational studies on the influence of the domain size. In ref. [21] a spatial incompressible mixing layer LES was performed in a domain comparable to S (with $(L_1, L_2, L_3) = (280, 56, 28)$) and an LES with a two times wider box.

These domains turned out to be too short to reach self-similarity, similar to the present findings from Chapters 3 and 5. The results show that the profiles of the variance of the velocity fluctuations become lower and higher for respectively R_{22} and R_{33} in the wider box. This corresponds to the present findings. The results for R_{12} are not mentioned in [21]. It was also found that the mixing layer growth rate is higher for the LES at the wider domain.

In the study reported in [4], the temporal incompressible mixing layer calculation described in [77] was extended by examining the effect of domain size and initial conditions. LES was used with the Lagrangian dynamic eddy viscosity model from [62]. Simulations were performed with initial conditions consisting of random noise as well as due to boundary layer turbulence. The domain width equals 31 times the initial momentum thickness, which corresponds to the width of S. In both cases, an increase of the streamwise and spanwise directions resulted in a larger growth rate and a higher peak of the spanwise velocity variance. The differences in the peaks of R_{33} were found to be an indicator of more highly three-dimensional flow patterns in the large-domain calculations. The use of a smaller domain forced the spanwise rollers to be two-dimensional during the late stages of the evolution. This resulted in a regular, well-ordered flow structure. These findings, a larger growth rate, a higher peak of the spanwise velocity variance and the presence of more three-dimensional structures for the wider box correspond with the present results. Next we change to a more complex setting where the Reynolds number is increased relative to WL.

6.3 Higher Reynolds number

In this section we discuss the results obtained for case WLR. This involves LES at a Reynolds number that is ten times higher than in the other settings discussed up to now. The main issue of this section is to consider the changes at higher Reynolds number. We focus on the presence of smaller scales and more positive spanwise vorticity. Moreover, we consider the effect on the dynamic coefficient and the resulting eddy viscosity.

We start with spanwise vorticity snapshots of both long domain simulations. The results are shown in Figure 6.6 for cases WL and WLR. From the results near the inflow boundary it is clear that the spanwise domain equals five fundamental wavelengths. Somewhat further downstream, we also observe modes with the other, longer spanwise wavelengths, which are imposed at the inflow boundary. These appear to result in a pairing of spanwise structures. Moreover, it is clear that the flow for WLR contains more small-scale behaviour which can be attributed to the higher Reynolds number. Case WL contains more patches where the spanwise vorticity is almost zero. In particu-
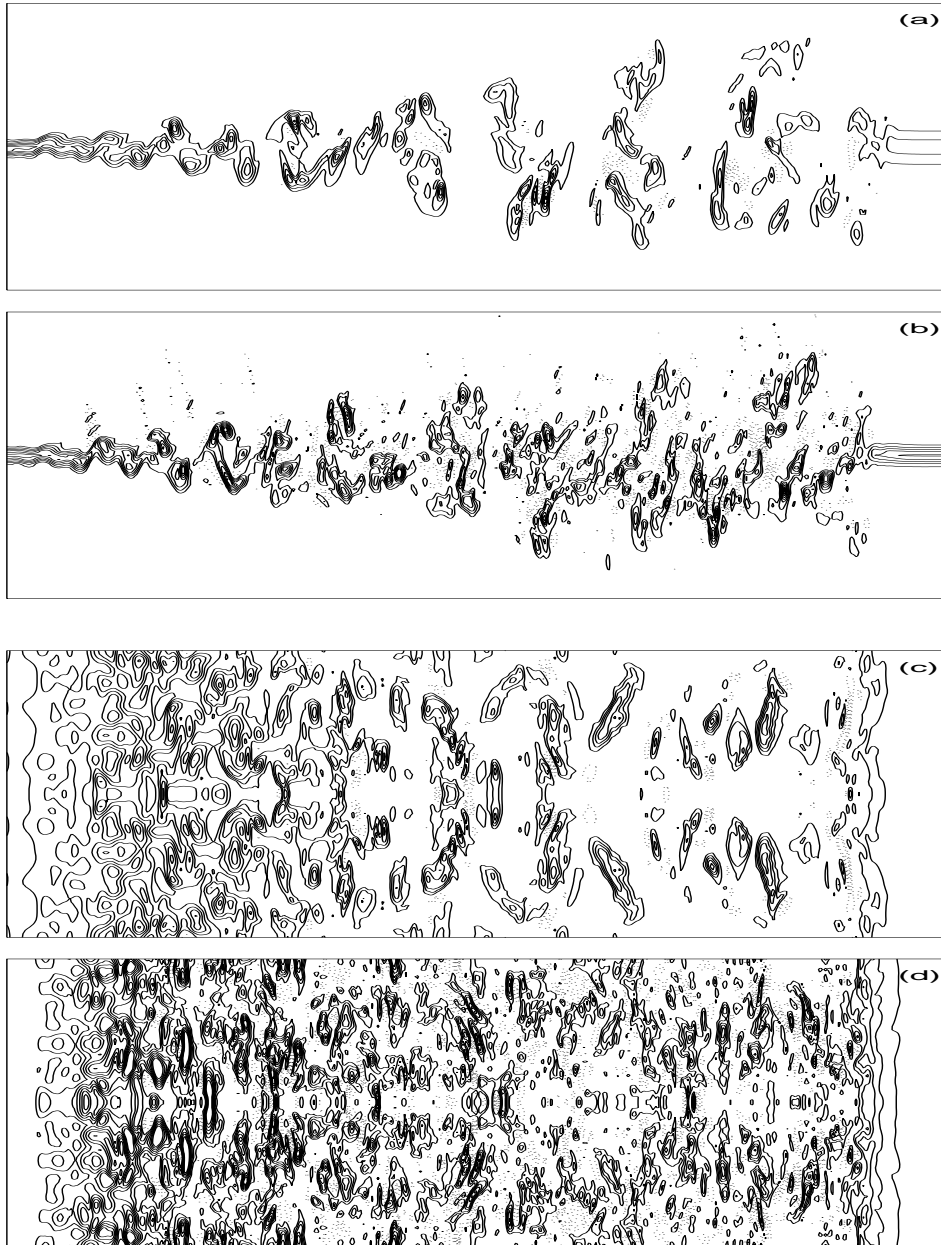
Figure 6.6: Pairs of spanwise vorticity at t=765 for WL and WLR in the plane $x_3 = -L_3/8$ with $X_1 \in [0, 515]$, $x_2 \in [-32, 32]$ (a,b) and the centerplane (c,d). The X_1 is in horizontal direction and the contour levels display negative (—) and positive ($\cdots$) values for $\pm(0.03, 0.06, \ldots, 0.21)$. Here, the domain is duplicated in the spanwise direction in order to give a better visual impression of the flow topology.

lar the centerplane results display that the small scale behaviour starts further downstream for WL.

Next we discuss the presence of positive spanwise vorticity. Positive spanwise vorticity comes into the WL system further downstream than in the higher Reynolds number simulation. As already argued in Chapter 5, the presence of positive spanwise vorticity is related to the transition to turbulence. This transition takes place further upstream at the higher Reynolds number. For comparison, the positive and negative contributions to the spanwise vorticity are integrated over x_3 and the part of the x_2-domain where $\langle \overline{\rho u}_1 \rangle$ deviates more than two percent from both free-stream values. On average, the level of positive spanwise vorticity is a factor of three higher in the high Reynolds number case, whereas the difference between both negative spanwise vorticity contributions is small.

For each of the two cases separately the amount and level of small scale structures are quite constant in the second part of the domain. For case WL, structures pair in spanwise direction and only two (symmetric) large-scale structures are present beyond $X_1 = 325$ (see Figure 6.6.c). Similarly as in the temporal high Reynolds number simulation [104], the turbulent regime in the centerplane of WLR approaches a situation of homogeneous turbulence (see Figure 6.6.d respectively Figure 16 in ref. [104]). So, the higher Reynolds number simulation comes closer to realistic turbulence. Finally we mention that the higher Reynolds number result contains some low level patches of vorticity on the upper free-stream side of the mixing layer. These are probably a result of the relatively low resolution. Their influence on the centerline
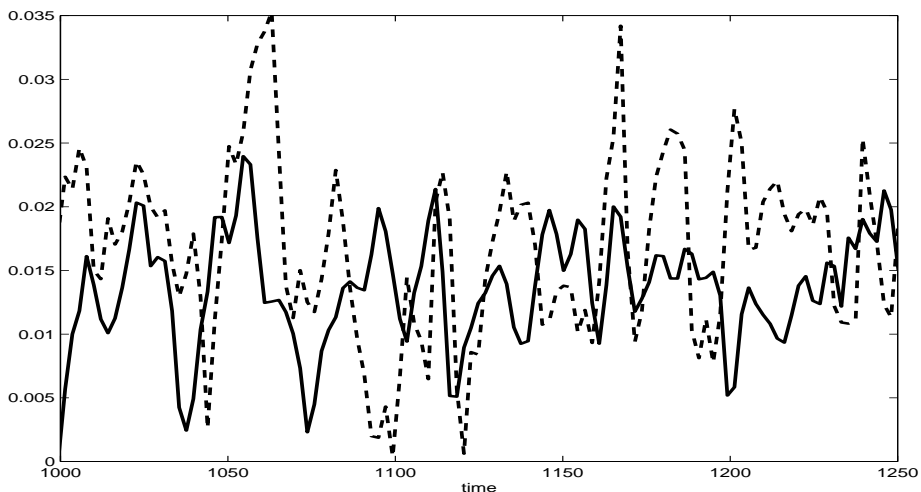

Figure 6.7: Dynamic coefficient C_d at X_{e5} as a function of time for WL (—) and WLR (− −).

behaviour is assumed to be small.

We have discussed the presence of smaller scales and more positive span-wise vorticity at higher Reynolds number. We continue with the dynamic coefficient. In Figure 6.7 part of its time history at X_{e5} is shown for systems WL and WLR. Both signals fluctuate in time and do not display a regular behaviour. For all six evaluation locations X_e the level of the time-averaged C_d is $20 - 35\%$ higher for WLR. Also the standard deviation of the WLR signal is $10 - 40\%$ higher than for WL. The larger Reynolds number in the WLR case results in a lower (absolute) viscous flux because it contains a $1/Re$ term. The increase due to the strain rate is smaller than the factor ten increase of the Reynolds number. The total effect is a viscous flux which is lower by a factor two to three.

Although the averaged dynamic coefficient is different for cases WL and WLR, the resulting effect on other quantities can still be small. We collected the corresponding LES eddy viscosity and (constant) viscous flux contributions. In Figure 6.8, the $\langle \nu_t \rangle_{x_3}$ profile is plotted as a function of x_2 at $X_1 = 321$ with $\nu_t = \bar{\rho} C_d \Delta^2 |S_{ij}(\tilde{\mathbf{u}})|$. For the WL setting it is almost everywhere below the corresponding molecular viscosity of $1/Re$. Together, these form the basis for part of the flux: $\partial_j \big((1/Re + \nu_t) S_{ij} \big)$. The $\langle \nu_t \rangle_{x_3}$ profile for WLR is of the same order of magnitude as for WL while the viscous contribution is a factor of ten lower.
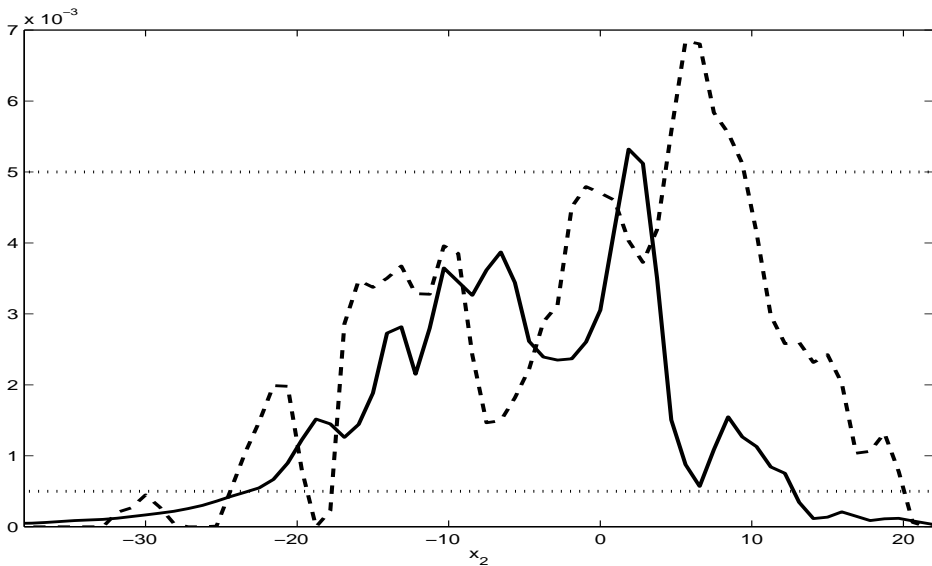

Figure 6.8: Spanwise averaged eddy viscosity $\nu_t = \bar{\rho} C_d \Delta^2 |S_{ij}(\tilde{\mathbf{u}})|$ at $X_1 = 321$ and $t = 3231$ as a function of x_2 for WL (——) and WLR (— —). The constant viscous contribution of $1/Re$ is also included for both cases ($\cdots$).

Before describing results based on time-averaging, we focus on the temporal spectrum. In Figure 6.2 some centerline streamwise momentum results of WL were collected. The result at the downstream location X_{e6} is next compared to the high-Reynolds number spectrum. In Figure 6.9 the temporal spectrum at X_6 is plotted for WL and WLR. The slope of the inertial range is much closer to the theoretical value of $-5/3$ for WLR. So, as conjectured in the previous section, a higher Reynolds number contributes to a range with a slope closer to -5/3.

Finally we discuss some statistical results. From empirical findings in literature [11], we know that a mixing layer growth rate only depends on the convective Mach number M_c, free-stream density ratio $s = \rho_2/\rho_1$ and free-stream velocity ratio $r = U_2/U_1$. As a result, the normalized momentum thickness growth rate, α_n (see Chapter 3), is independent of the Reynolds number. In our simulations we found that the momentum thicknesses for WL and WLR globally coincide. The growth is faster for WLR behind the inflow boundary, but both values of the growth rate approach each other in the second half of the domain. The normalized growth rate of WLR is slightly lower and equals 0.027. So, although for example the snapshots of spanwise vorticity are rather different for WL and WLR (according to Figure 6.6), the
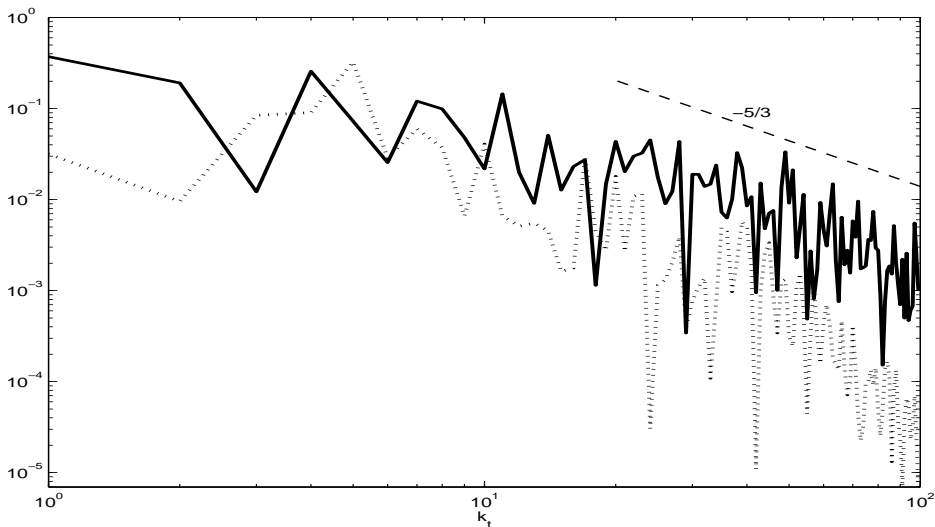

Figure 6.9: Temporal spectrum of the centerline $\overline{\rho u}_1$ signal at X_{e6} as a function of the mode frequency k_t for cases $WL(\cdots)$ and WLR (—). The results are based on the signal from $t = 765$ until 1191. Also a straight line with slope $-5/3$ is included ($--$).

momentum thicknesses develop approximately the same. Also the Reynolds stress tensor profile should be independent of the Reynolds number, as long as it is considered with respect to the normalized coordinate $x_2/\theta(X_1)$ [41, 77]. The Reynolds stress tensors for WL and WLR only show some differences around the peak levels.

Summarizing, we recall the quantities that change significantly when the Reynolds number is increased by a factor ten. The spanwise vorticity displays more small scales for the WLR case. Moreover, positive vorticity is present from a more upstream location than in WL. The dynamic coefficient in the turbulent regime has a larger mean value and standard deviation for WLR. Besides, we also observed a somewhat larger value for the eddy viscosity $\langle \nu_t \rangle_{x_3}$. From the results based on statistical averaging, the momentum thickness does not change when the Reynolds number is increased. The components of the Reynolds stress tensor also do not change much. More results of WL and WLR are given in the next section where we focus on statistics of the dynamic coefficient.

6.4   Adapted dynamic model

In this section, we formulate a variant of the dynamic eddy viscosity model. First we mention how some other studies overcome the artificial mathematical prescriptions to assure the stability of the dynamic eddy viscosity model. The LES study in [39] introduces the so-called dynamic localization model. The method employs an integral equation whose solution yields the model coefficient as a function of position and time. It can be applied to general inhomogeneous flows and does not suffer from the artificial mathematical prescriptions of the original formulation described in [37]. We also mention the study from [62] which combines the statistical and local approaches by accumulating the required averages over flow path lines. This Lagrangian way of tracking involves a time integration and linear interpolation in space. This so-called Lagrangian dynamic eddy viscosity model can also be used for the simulation of inhomogeneous flows in complex geometries.

In Chapter 5 it was found that the dynamic eddy viscosity model is suitable for LES while the Smagorinsky model produces too much dissipation. The dynamic coefficient is highly fluctuating in time and space. For the present study, we consider an alternative formulation where the coefficient is averaged over time, which is a homogeneous coordinate for the present application. This idea is supported by the streamwise development of the time-averaged dynamic coefficient $\langle C_d \rangle_t$. As we will see further on, its centerplane level is almost constant over a long streamwise distance. The *a priori* result of time-averaging the instantaneous dynamic coefficient globally gives the same

result as the corresponding *a posteriori* value where the dynamic coefficient during the LES is based on its own time-average. In the previous sections, we discussed the feasibility study for a numerical simulation of the turbulent mixing layer. This new variant of the dynamic eddy viscosity model may no longer need the presence of a homogeneous direction in space. As a result, it is suitable for LES of complex settings. We first consider the time-averaged C_d from the dynamic formulation used up to now. Then we continue with the new subgrid-model formulation.

In Figure 6.10 we collected the centerplane time-averaged value of the dynamic coefficient C_d from the dynamic eddy viscosity model. It is based on the time interval $[765, 3231]$ and plotted as a function of the streamwise coordinate. We have given the results for all four settings used up to now. Since transition starts at a lower value of X_1 for WLR, $\langle C_d \rangle_t$ also increases from zero at an earlier stage. The WLR value remains higher than WL similarly as for the instantaneous result in Figure 6.7. From one third of the domain, $\langle C_d \rangle_t$ only slowly varies with x_1. The $\langle C_d \rangle_t$ from the narrow domain case S starts growing further downstream and does not reach an approximately constant value. So, the wider box and extra modes are crucial to reach a steady level of the time-averaged dynamic coefficient. Finally we remark the resemblance in the results of W and WL. Both have approximately a constant level which
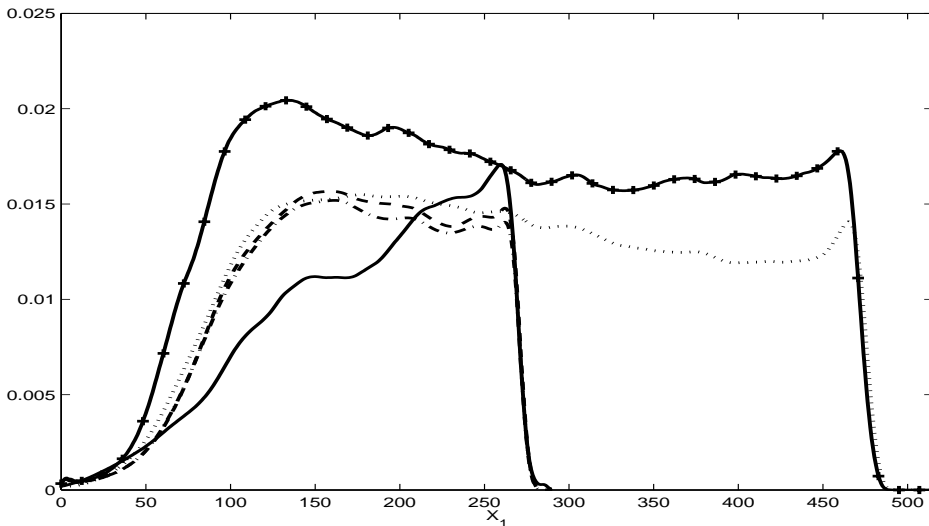

Figure 6.10: Time-averaged centerplane dynamic coefficient, $\langle C_d \rangle_t$, as a function of X_1 for S (—), W (−−), WL ($\cdots$) and WLR (+) and the value of C_m for WC_m at t=3231 (−·).

corresponds to a Smagorinsky constant of $C_S = 0.12$. The length of the flow domain does not affect the time-averaged dynamic coefficient, provided it is sufficiently long. The WLR value for $\langle C_d \rangle_t$ is somewhat larger and approaches a C_S equal to approximately 0.13. This value was also found for the average dynamic coefficient of the dynamic eddy viscosity model LES of the temporal mixing layer at the same (high) Reynolds number [104].

We continue with the formulation of the new subgrid-model introduced above. The new setting, referred to as WC_m, comprises case W with an adaptation for the dynamic coefficient. In first instance, the dynamic coefficient C_d in the dynamic eddy viscosity model is replaced by a mean coefficient C_m which is defined as:

$$C_m(x_1, x_2, t) = \frac{1}{t} \int_0^t C_d(x_1, x_2, t')dt' \quad (t > 0), \tag{6.1}$$

where C_d equals the dynamic coefficient for the dynamic eddy viscosity model (see equation (5.13)):

$$C_d(x_1, x_2, t) = \frac{\langle M_{ij} L_{ij} \rangle_{x_3}}{\langle M_{ij} M_{ij} \rangle_{x_3}}. \tag{6.2}$$

Based on the $\langle C_d \rangle_t$ results from Figure 6.10, we expect that C_m approaches a constant (x_1, x_2)-dependent profile for increasing time. As a result, the spanwise averaging may no longer be necessary. This opens possibilities for complex flow configurations that do not contain a homogeneous spatial direction.

When the coefficient defined in (6.1) is used for a simulation that starts from a laminar field, the simulation may become unstable due to initial large transients in C_d. This problem is overcome by introducing a maximum level for C_d. Thus, we take:

$$C_m(x_1, x_2, t) = \frac{1}{t} \int_0^t \min\{C_d(x_1, x_2, t'), 1.0\}dt'.$$

The upper boundary of 1.0 is an order of magnitude higher than the C_d value in Figure 6.7. This adaptation is only necessary during the initial part of the LES. Furthermore, C_d is still clipped as well. The new model is about 30% cheaper than the original dynamic eddy viscosity model due to the fact that is only updated each time step. The computational overhead of the new model can even be improved by decreasing the frequency of updating C_d since its profile converges after some time. It is noted that an even better alternative for the dynamic coefficient may be the separate time-averaging of the nominator and denominator in formula (6.2). This alternative is closer to the temporal equivalent from [104] where both N and D are separately averaged over the two homogeneous directions x_1 and x_3. Besides, it probably no longer has the

problem of extremely high C_d values because the (time-averaged) denominator may have less chance to be very small.

In Figure 6.10 we have also included the centerline value of C_m throughout the streamwise domain. It is very close to the time-averaged C_d from W. The deviation could partly be due to the fact that time-sampling of W is started at $t = 765$. As a result, the contribution just after initiation is not taken into account while it is in WC_m. We next focus on the dynamic coefficient in the turbulent regime of W and WC_m and its effect on the turbulent stress tensor.

The x_2-profiles of the modeled $\langle \bar{\rho}\tau_{12} \rangle$ as well as C_m (from WC_m), the instantaneous C_d and time-averaged $\langle C_d \rangle_t$ (from W) are collected in Figure 6.11. It is clear that the instantaneous C_d from case W is fluctuating. Its time-average, $\langle C_d \rangle_t$, approximately coincides with C_m in the centerline region. We again recognize the $C_S = 0.12$ level already mentioned for the time-averaged centerline coefficient in Figure 6.10. Outside this region, C_m may become larger, but the resulting streamwise subgrid flux remains very small there anyway. So, the relatively high value of the dynamic coefficient, which is due to the fact that the denominator of C_d is small in the outer mixing layer region, does hardly affect the resulting flux. We also mention that the centerplane
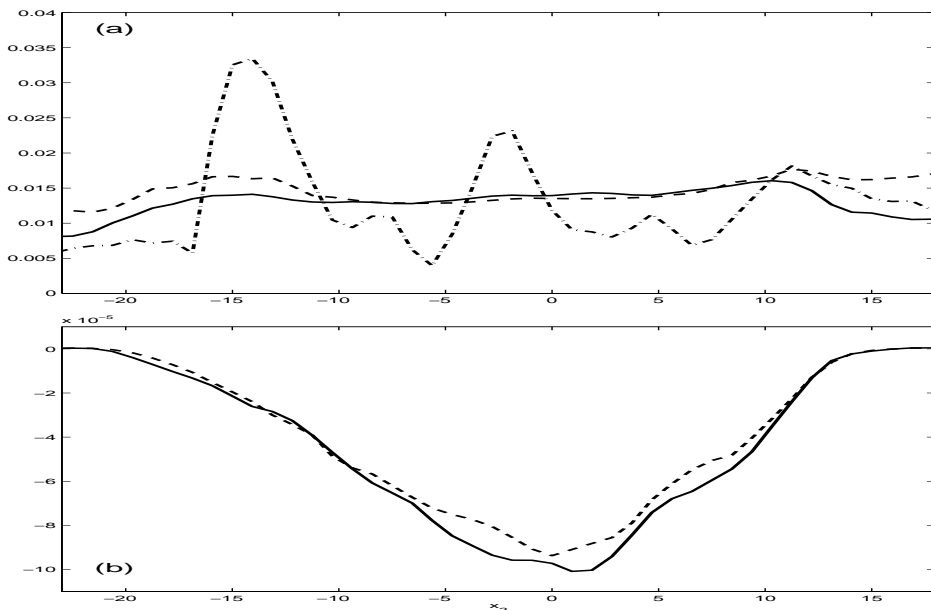

Figure 6.11: Averaged profiles for $W(—)$ and $WC_m(--)$ at $X_1 = 225$ as a function of x_2. The dynamic coefficient C_m from WC_m is shown together with an instantaneous C_d (t $= 3231; -\cdot$) and $\langle C_d \rangle_t$ from W in (a). The modeled $\langle \bar{\rho}\tau_{12} \rangle$ is displayed in (b).

subgrid flux from W and WL is of the same order of magnitude as the viscous flux (see Figure 6.8). Finally, although the instantaneous streamwise subgrid flux clearly differs, the difference between $\langle \bar{\rho}\tau_{12} \rangle$ profiles of W and WC_m is small (less than 10%).

Next we discuss the effect of C_m on some statistical quantities. The momentum thickness hardly shows any change compared to that of setting W. The deviation between the result of W and WC_m is within two percent. We continue with a plot of the streamwise development of peak values of the Reynolds stress tensor for all cases introduced here. From the results shown in Figure 6.12, it is clear that the Reynolds stress tensor components for W and WC_m are approximately equal. The difference in the second half of the streamwise domain is below five percent for all components. Similarly as in Figure 6.10 also the WL result is close to the other low Reynolds number cases. The narrow-domain results of S are not included. Similarly as the DNS results from Figure 3.4, the results of S hardly display the constant peak level in streamwise direction which is required for self-similarity.

Except for R_{33}, the higher Reynolds number in WLR results in a stronger increase of the Reynolds stress tensor peak values close after the inflow boundary. The high Reynolds number result approaches that of the others between $X_1 = 150$ and 200. Whether further downstream either the WL or the WLR Reynolds stress peak value is higher depends on the component. In particular this difference is largest in the second half of the streamwise domain for R_{33}. The width of the profiles for WL and WLR approximately corresponds. However, throughout the second half of the domain, the peak values of R_{33} differ by about 20% and 10% or less for the other components. We recall that a large difference is also found in the spanwise behaviour of the spanwise vorticity for WL and WLR in Figure 6.6.

Finally we note that the high Reynolds number results do not clearly show a better behaviour regarding self-similarity. The streamwise turbulence intensity R_{11} required the least streamwise distance to become approximately self-similar, followed by the normal turbulence intensity R_{22}. The peak value of the first component R_{11} only changes with about 5% throughout the second half of the domain. The development of R_{33} does not display signs of self-similarity and the streamwise variations in R_{12} are rather large as well. We note the striking decrease of R_{33} just behind the inflow boundary. This again stresses the sensitivity of this component with respect to the inflow condition. The wide box results clearly show signs of self-similarity, which is not the case for setting S. So, the spanwise extent should be large enough in order to approach self-similar behaviour of the Reynolds stress tensor at all, and the cumbersome results for R_{33} and R_{12} in this respect may require further
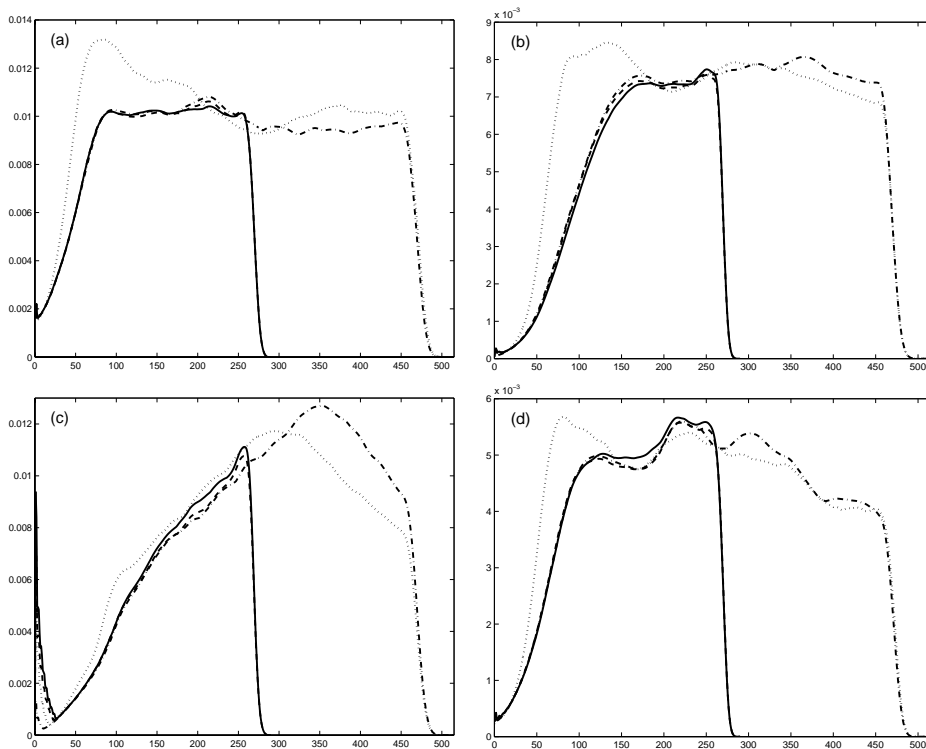
Figure 6.12: Reynolds stress tensor peak values as a function of the streamwise coordinate for settings W (—), WC_m (– –), WL (– ·), and WLR (· · ·) for R_{ii} (i=1-3;a-c) and $-R_{12}$(d).

variations in the size of the domain. This is also necessary to reach a more or less constant level of the averaged dynamic coefficient (see Figure 6.10).

Concluding, we have observed that the highly fluctuating dynamic coefficient of W mainly appears to be relevant for the instantaneous behaviour of the simulation. The time-averaged equivalent of WC_m results in about the same statistical behaviour. The CPU time can be lowered even more by decreasing the frequency of updating the time-averaged coefficient. Together with its suitability for flows that no longer contain any homogeneous direction, it is worth to further explore the possibilities of this subgrid-model.

6.5 Conclusions

The main topic of this chapter was an investigation of the suitability of LES for more realistic mixing layers, in particular in a larger domain and at a higher Reynolds number using the dynamic eddy viscosity model. In the previous chapters, we employed the setting of the 'minimal mixing layer',

where the spanwise extent was equal to a single fundamental wavelength. This preparatory study has been very useful to consider some features which are typical for the mixing layer and for turbulent flow. From the results of the present chapter we found that the crucial step towards a realistic mixing layer includes the increase of the spanwise computational domain. The main change implied by the wider domain and the corresponding extra inflow perturbations is the enhanced three-dimensionality of the turbulence, which results in an increase in momentum thickness growth rate.

Similarly as in other studies, the present findings show the presence of more three-dimensional structures in a wider computational box. This was concluded from the higher extremal values of the streamwise vorticity, from the more complex structures in the centerplane spanwise vorticity and from the substantially larger spanwise turbulence intensity. Further studies with other spanwise domain lengths should be performed in order to investigate the influence more thoroughly.

The spanwise turbulence intensity R_{33} did not show any self-similar behaviour for the short and long streamwise domains. All other Reynolds stress tensor components displayed some self-similarity for settings that involved a wider box. The results did not change much when the streamwise domain was extended. The results based on a ten times larger Reynolds number did not show signs of a better self-similarity. So, we can conclude that the major contribution towards an LES that contains self-similar behaviour comes from the increase in the spanwise domain extent.

Next to the main issue, the feasibility study of the mixing layer, this chapter was also devoted to the introduction of a new subgrid-model. Most settings described in this chapter employed the dynamic eddy viscosity model. Based on the approximate independence of the time-averaged dynamic coefficient of the streamwise coordinate, the dynamic coefficient C_d was replaced by its time average in the new subgrid-model. The advantage of this adapted model is the fact that it may be applied to flows that no longer contain a homogeneous direction. The new model only has a minor effect on statistical results like the momentum thickness and Reynolds stress tensor as well as the time-averaged turbulent stress tensor. It is some thirty percent cheaper than the original dynamic eddy viscosity model due to the fact that the dynamic coefficient is only updated each time step. This can even be improved by decreasing the frequency of updating C_d. It can be concluded that it is worth to further explore the possibilities of this model. Finally, a number of recommendations for future research are pointed out in the next section.

6.6 Recommendations for future research

Since DNS cannot be performed for most practically relevant flows, the development of LES methods for complex flows is an important issue. As a first step, we have performed LES for a high Reynolds number mixing layer at low convective Mach number in a large computational domain. A next step in this research could be the performance of LES at higher convective Mach numbers. The growth rate reduction that already has been observed for the temporal mixing layer and in several physical experiments of the mixing layer can then also be studied for the spatial setting. Furthermore it would be interesting to find out whether self-similarity is reached to the same extent. In particular this might help to understand why, in contrast to the other components of the Reynolds stress tensor, the spanwise turbulence intensity has not shown signs of self-similarity in the simulations described here.

The underlying idea of this thesis involved a feasibility study of the spatial mixing layer. We one by one recall all constraints introduced to enable a numerical simulation: the domain extent, Reynolds number and resolution. It was found that the extent of the short streamwise domain is long enough to display self-similarity in the momentum thickness and streamwise and normal turbulence intensities. The case with the longer streamwise domain can be regarded as a verification for the behaviour of these statistical quantities. The spanwise extent as well as the inclusion of the extra inflow perturbations that could be taken into account played a major role in Chapter 6. The confined mixing layer on the single spanwise wavelength domain displayed results that were dominated by a lack of spanwise development. As a result, the level of the spanwise velocity fluctuations was too low. It is necessary to further verify the effect of the spanwise extent of the computational domain.

As a final step in the effort to reach a numerical simulation of the laboratory mixing layer, the Reynolds number was increased. Mainly some instantaneous properties were affected by this change. At the second half of the domain, a minor effect was present in the Reynolds stress tensor, except for the third component where the influence was larger. Another increase in the Reynolds number should be made to verify whether the influence of the present Reynolds number already is of minor importance. Then it can be interpreted as a zero molecular viscosity situation.

The development of numerical research in turbulence for the past decade has - together with the increase in computational effort - resulted in a shift of temporal settings to spatial settings. Several characteristic features of temporal mixing layers were also found for spatial mixing layers. The introduction of the dynamic procedure has substantially improved the performance of LES. As a result, LES has become a tool to answer many of the still open questions in turbulence. Simultaneously, several new questions come up. Most of

them deal with more realistic turbulent mixing layers and other shear flows, that arise in for example combustion and settings with complicated geometries. Thus the subject of turbulence will keep us busy for at least some extra decades.

Appendix A

Evaluation details

The aim of this appendix is to define basic elements from which all terms in the turbulence kinetic energy equation can be built. These terms should be computed during the DNS. Therefore we prefer a conveniently arranged implementation. We first recall the turbulence kinetic energy equation (see (3.3)):

$$\partial_j(\bar{\rho} k \, \tilde{u}_j) = -\overline{\rho u_i'' u_j''} \, \partial_j \tilde{u}_i - 1/2 \, \partial_j \overline{\rho u_i'' u_i'' u_j''} + \partial_j \overline{u_i'' \sigma_{ij}} - \partial_j \overline{p u_j''}$$
$$+ \overline{p \, \partial_j u_j''} - \overline{\sigma_{ij} \, \partial_j u_i''}, \qquad (A.1)$$

In order to have a clear and simple implementation of the evaluation we keep the number and complexity of the basic elements small. The following eight groups of quantities are computed in order to evaluate all other terms of the turbulence kinetic energy equation (A.1):

$$A_1 = (\bar{\rho}, \overline{\rho u_1}, \overline{\rho u_2}, \bar{p})$$
$$A_2 = (\overline{\rho u_1 u_1}, \overline{\rho u_2 u_2}, \overline{\rho u_3 u_3}, \overline{\rho u_1 u_2})$$
$$A_3 = (\overline{p u_1}, \overline{p u_2})$$
$$A_4 = \overline{p \partial_j u_j}$$
$$A_5 = (\overline{\sigma_{11}}, \overline{\sigma_{22}}, \overline{\sigma_{12}})$$
$$A_6 = \overline{\sigma_{ij} \partial_j u_i}$$
$$A_7 = (\overline{u_i \sigma_{i1}}, \overline{u_i \sigma_{i2}})$$
$$A_8 = (\overline{\rho u_i u_i u_1}, \overline{\rho u_i u_i u_2}).$$

Because of the assumption of spanwise symmetry, several quantities equal zero by definition and thus are not taken into account. For example,

$$\tilde{u}_3 = \sigma_{13} = \overline{\rho u_1 u_3} = \overline{\rho u_3 u_3 u_3} \equiv 0.$$

The terms in (A.1) can be constructed from the quantities $A_1 - A_8$ using the Reynolds conditions [64]. These conditions state that

$$\overline{af + bg} = a\overline{f} + b\overline{g}$$
$$\overline{\overline{f}g} = \overline{f}\,\overline{g}$$
$$\overline{\partial_t f} = \partial_t \overline{f}$$
$$\overline{\partial_j f} = \partial_j \overline{f},$$

for arbitrary, smooth functions $f(\mathbf{x}, t)$ and $g(\mathbf{x}, t)$ and arbitrary constants a and b as can readily be verified. The relation $\overline{\overline{f}} = \overline{f}$, used often, can easily be derived from these conditions.

Finally we note that when A_6 is computed in a straightforward way, nine terms need to be taken into account. The expression can be reduced when employing some specific properties of the strain rate tensor (see (2.5)):

$$\overline{\sigma_{ij}\partial_j u_i} = \overline{S_{ij}\,\partial_j u_i}/Re$$
$$= 1/2\,\overline{S_{ij}^2}/Re$$
$$= \overline{(S_{11}^2 + S_{22}^2 + S_{11}S_{22} + S_{12}^2 + S_{13}^2 + S_{23}^2)}/Re.$$

Here we used the symmetry of the strain rate tensor and the fact that its trace equals zero. In this appendix we have focused on evaluation details regarding the computation of the terms in the kinetic energy equation during the DNS. The elements $A_1 - A_8$ form basic blocks from which all terms of the turbulence kinetic energy equation can be evaluated in a simple way.

Bibliography

[1] *Agard Advisory Report 345*, A selection of Test Cases for the validation of Large-Eddy Simulations of Turbulent Flows, April 1998.

[2] ALAM M. & SANDHAM N.D., Direct numerical simulation of 'short' laminar separation bubbles with turbulent reattachment, *J. Fluid Mech.*, 403, pp. 223-250, 2000.

[3] ANSARI A., Self-similarity and mixing characteristics of turbulent mixing layers starting from laminar initial conditions, *Phys. Fluids*, 9(6), 1997.

[4] BALARAS E., PIOMELLI U. & WALLACE J.M., Large-eddy simulation of turbulent mixing layers, *Advances in Turbulence VIII,* pp. 535-538, Kluwer Academic Publishers, 2000.

[5] BARDINA J., FERZIGER J.H. & REYNOLDS W.C., Improved turbulence models based on LES of homogeneous incompressible turbulent flows. Department of Mechanical Engineering, *Report No. TF-19*, Stanford, 1984.

[6] BARRE S., QUINE C. & DUSSAUGE J.P., Compressibility effects on the structure of supersonic mixing layers: Experimental Results, *J. Fluid Mech.*, 259, pp. 47-78, 1994.

[7] BATCHELOR G.K., *The theory of Homogeneous Turbulence*, Cambridge Unversity Press, Cambridge, 1953.

[8] BATCHELOR G.K., *An introduction to fluid dynamics*, Cambridge University Press, Cambridge, 1967.

[9] BELL J.H. & MEHTA R.D., Development of a Two-Stream Mixing Layer from Tripped and Untripped Boundary Layers, *AIAA J.*, 12, pp. 2034-2042, 1990.

[10] BELL J.H., PLESNIAK M.W. & MEHTA R.D., Spanwise averaging of plane mixing layer properties, *AIAA J.*, 30, pp. 835-837, 1992.

[11] BIRCH S.F. & EGGERS J.M., A critical review of the experimental data for developed free shear layers, *NASA SP-321*, pp. 11-40, 1972.

[12] BLAISDELL G.A., MANSOUR N.N. & REYNOLDS W.C., Numerical simulation of compressible homogeneous turbulence, Department of Mechanical Engineering, *Report No. TF-19*, Stanford, 1991.

[13] BOERSMA B.J., BRETHOUWER G. & NIEUWSTADT F.T.M., A numerical investigation on the effect of the inflow conditions on the self-similar region of a round jet, *Phys. Fluids*, 10(4), pp. 899-909, 1998.

[14] BOGDANOFF D.W., Compressibility effects on the growth and structure of homogeneous turbulent shear flow, *J. Fluid Mech.*, 256, pp. 443-485, 1983.

[15] BOUSSINESQ J., Essai sur la Théorie des eaux Courantes, *Mém. Preés. par div. savant á l'Acad. sci.*, 23(1), pp. 1-680, 1887.

[16] BRADSHAW P., The effect of initial conditions on the development of a free shear layer, *J. Fluid Mech.*, 26, pp. 225-236, 1966.

[17] BROWAND F.K. & LATIGO B.O., Growth of the two-dimensional mixing layer from a turbulent and nonturbulent boundary layer, *Phys. Fluids,* 22(6), pp. 1011-1019, 1979.

[18] BROWN G.L. & ROSHKO A., On density effects and large scale structure in turbulent mixing layers, *J. Fluid Mech.*, 64, pp. 775-816, 1974.

[19] CHANDRSUDA C., MEHTA R.D., WEIR A.D. & BRADSHAW P., Effect of free-stream turbulence on large sturcture in turbulent mixing layers, *J. Fluid Mech.*, 85, pp. 693-704, 1978.

[20] COLONIUS T., LELE S.K. & MOIN P., Sound generation in a mixing layer, *J. Fluid Mech.*, 330, pp. 375-409, 1997.

[21] COMTE P., SILVESTRINI J.H. & BÉGOU P., Streamwise vortices in Large-Eddy simulations of mixing layers, *Eur. J. Mech. B/Fluids*, 17(4), pp. 615-637, 1998.

[22] DE BRUIN I.C.C., WASISTHO B., GEURTS B.J. & KUERTEN J.G.M., Simulation of spatially developing turbulent shear flows, *Symposium on Comp. and Exp. Methods in Mechanical and Thermal Eng., Ghent, Belgium,* 1998.

[23] DE BRUIN I.C.C., WASISTHO B., GEURTS B.J., KUERTEN J.G.M. & ZANDBERGEN P.J., Simulation of subsonic spatially developing turbulent shear flows, *Lecture Notes in Physics,* 515, pp. 147-152, Springer, Berlin, 1998.

[24] DE BRUIN I.C.C., GEURTS B.J. & KUERTEN J.G.M., Statistical Analysis of the Turbulent Mixing Layer, *Proceedings of the 3rd workshop on DNS and LES*, Cambridge, 1999.

[25] DE BRUIN I.C.C., GEURTS B.J., KUERTEN J.G.M. & DRIESEN C.H., Robustness of flow phenomena in a spatially developing turbulent mixing layer, *Proceedings 2nd AFOSR conference on DNS & LES,* New Jersey, 1999.

[26] DE BRUIN I.C.C., GEURTS B.J. & KUERTEN J.G.M., Direct Numerical Simulation of the Spatially Developing Turbulent Mixing Layer, *Proceedings Turbulence and Shear Flow Phenomena 1,* Santa Barbara, 1999.

[27] DIMOTAKIS P.E. & BROWN G.L., The mixing layer at high Reynolds numer: large-structure dynamics and entrainment, *J. Fluid Mech.*, 78, pp. 535-560, 1976.

[28] DIMOTAKIS P.E., Two-dimensional shear-layer entrainment, *AIAA J.,* 24, pp. 1791-1796, 1986.

[29] DIMOTAKIS P.E., Turbulent free shear layer mixing and combustion, *Progress in Astronautics and Aeronautics,* 137, pp. 265-340, 1991.

[30] FAVRE A. (editor), *The Mechanics of Turbulence*, Gordon & Breach, New York, 1964.

[31] FAVRE A., Equations des gaz turbulents compressibles, *Journal de Mécanique,* 4, pp. 361-421, 1965.

[32] FERZIGER J.H., Large eddy simulation, *Simulation and modeling of turbulent flows*, Eds. T.B. Gatski *e.a.*, Oxford university press, 1996.

[33] FREUND J.B., LELE S.K. & MOIN P., Compressibility effects in a turbulent annular mixing layer. Part 1. Turbulence and growth rate, *J. Fluid Mech.*, 421, pp. 229-267, 2000.

[34] FRISCH U., *Turbulence*, Cambridge University Press, Cambridge, 1995.

[35] GEORGE W.K., The nature of Turbulence, *Forum on Turbulent Flows*, ASME, FED, 94, eds. W.M. Bower, M.J. Morris & Samimy M., Book Number H00599, 1990.

[36] GEURTS B.J., DE BRUIN I.C.C. & SARKAR S., Rapid and slow contributions to the turbulent stress tensor and their inverse modelling in a turbulent mixing layer, *Advances in Turbulence VIII,* pp. 539-542, Kluwer Academic Publishers, 2000.

[37] GERMANO M., PIOMELLI U., MOIN P. & CABOT W.H., A dynamic subgrid-scale eddy viscosity model, *Phys. Fluids A*, 3, pp. 1760-1765, 1991.

[38] GERMANO M., Turbulence: the filtering approach, *J. Fluid Mech.*, 238, pp. 325-336, 1992.

[39] GHOSAL S., LUND T.S., MOIN P. & AKSELVOLL K., A dynamic localization model for large-eddy simulation of turbulent flows, *J. Fluid Mech.*, 286, pp. 229-255, 1995.

[40] GHOSAL S. & ROGERS M.M., A numerical study of self-similarity in a turbulent plane wake using large-eddy simulation, *Phys. Fluids*, 9(6), pp. 1729-1739, 1997.

[41] GOEBEL S.G. & DUTTON J.C., Experimental Study of Compressible Turbulent Mixing Layers, *AIAA J.*, 29(4), pp. 538-546, 1991.

[42] HORIUTI K., Rotational transformation and geometrical correlation of SGS models, *Modern Simulation Strategies for turbulent flows,* Ed. B.J. Geurts, Edwards Publ., pp. 123-140, 2001.

[43] HOWARD R.J.A., Direct Numerical Simulation and modeling of turbulent channel flows subjected to complex distortions, *Ph.D. Dissertation*, Queen Mary and Westfield College, London, 1999.

[44] HUANG L.S. & HO C.M., Small scale transition in a plane mixing layer, *J. Fluid Mech.*, 210, pp. 475-500, 1990.

[45] JIMÉNEZ J. & MOIN P., The minimal flow unit in near-wall turbulence, *J. Fluid Mech.*, 225, pp. 213-240, 1991.

[46] JIMÉNEZ J. & MOSER R.D., Large-Eddy Simulations: Where Are We and What Can We Expect?, *AIAA J.*, 38(4), pp. 605-612, 2000.

[47] JONES W.P. & LAUNDER B.E., The prediction of laminarization with a two-equation model of turbulence, *Int. Journal of Heat and Mass Transfer,* 15, pp. 301-304, 1972.

[48] KNIGHT D.D., Numerical Simulation of Compressible Turbulent Flows Using the Reynolds-Averaged Navier-Stokes Equations, Lecture series

held at the von Kármán Institute for Fluid Dynamics in Rhode-Saint-Genèse, *Agard Report*, 819, 1997.

[49] KOLMOGOROV A.N., The local structure of turbulence in incompressible viscous fluid for very large Reynolds numbers. *Dokl. Akad. Nauk. SSSR*, 30, 301-305. Reprinted in 1991, *Proc. R. Soc. Lond. A*, 434, pp. 9-13, 1941.

[50] KUERTEN J.G.M., GEURTS B.J., VREMAN A.W. & GERMANO M., Dynamic inverse modeling and its testing in large-eddy simulations of the mixing layer, *Phys. Fluids*, 11(12), pp. 3778-3785, 1999.

[51] LASHERAS J.S., CHOI H. & MAXWORTHY T., On the origin and evoluation of streamwise vortical structures in a plane, free shear layer, *J. Fluid Mech.*, 172, pp. 231-258, 1986.

[52] LAUNDER B.E. & SHARMA B.I., Application of the Energy Dissipation Model of Turbulence to the Calculation of Flow Near a Spinning Disc, *Letters in Heat and Mass Transfer*, 1(2), pp. 131-138, 1974.

[53] LELE S.K., Compressibility effects on turbulence, *Ann. Rev. Fluid Mech.*, 26, pp. 211-254, 1994.

[54] LESIEUR M., *Turbulence in Fluids,* 3rd edition, Kluwer Academic Publishers, Dordrecht, 1997.

[55] LI N., BALARAS E. & PIOMELLI U., Inflow conditions for large-eddy simulations of mixing layers, *Phys. Fluids*, 12(4), pp. 935-938, 2000.

[56] LILLY D.K., A proposed modification of the Germano subgrid-scale closure method. *Phys. Fluids A*, 4, pp. 633-635, 1992.

[57] LIU S., MENEVEAU C. & KATZ J., On the properties of similarity subgrid-scale models as deduced from measurements in a turbulent jet, *J. Fluid Mech.*, 275, pp. 83-119, 1994.

[58] LIU Z. & LIU C., Fourth order finite difference and multigrid methods for modelling instabilities in flat plate boundary layers, *Computers and Fluids,* 23, pp. 955-982, 1994.

[59] MANSOUR N.N., KIM J. & MOIN P., Reynolds-stress and dissipation-rate budgets in a turbulent channel flow, *J. Fluid Mech.*, 194, pp. 15-44, 1988.

[60] MEHTA R.D., Effect of velocity ratios on plane mixing layer development: Influence of the splitter plate wake, *Exp. Fluids,* 10, pp. 194-204, 1991.

[61] MEHTA R.D. & WESTPHAL R.V., Near-field turbulence properties of single- and two-stream plane mixing layers, *Exp. Fluids,* 4, pp. 257-266, 1986.

[62] MENEVEAU C., LUND T.S. & CABOT W.H., A lagrangian dynamic subgrid-scale model of turbulence, *J. FLuid Mech.*, 319, pp. 353-385, 1996.

[63] MOIN P. & KIM J., Tackling Turbulence with Supercomputers, *Scientific American*, 276(1), pp. 62-68, 1997.

[64] MONIN A.S. & YAGLOM A.M., *Statistical Fluid Mechanics*, Mechanics of Turbulence Volume 1, MIT Press, Cambridge, 1977.

[65] MOSER R.D. & ROGERS M.M., The three-dimensional evolution of a plane mixing layer: pairing and transition to turbulence, *J. Fluid Mech.*, 247, pp. 275-320, 1993.

[66] MOSER R.D., ROGERS M.M. & EWING D.W., Self-similarity of time-evolving plane wakes, *J. Fluid Mech.*, 367, pp. 255-289, 1998.

[67] OSTER D. & WYGNANSKI I., The forced mixing layer between parallel streams, *J. Fluid Mech.,* 123, pp. 91-130, 1982.

[68] PAPAMOSCHOU D. & ROSHKO A., The compressible turbulent shear layer: an experimental study, *J. Fluid Mech.*, 197, pp. 453-477, 1988.

[69] PIOMELLI U., ZANG T.A., SPEZIALE C.G. & HUSSAINI M.Y. On the large-eddy simulation of transitional wall-bounded flows, *Phys. Fluids A*, 2, pp. 257-265, 1990.

[70] PLESNIAK M.W., MEHTA R.D. & JOHNSTON J., Curved two-stream turbulent mixing layers: three-dimensional structure and streamwise evolution, *J. Fluid Mech.*, 270, pp. 1-50, 1994.

[71] POGGIE J. & SMITS A.J., Large-Scale Coherent Turbulence Structures in a compressible Mixing Layer Flow, *AIAA P.*, 96, pp. 1-11, 1996.

[72] POINSOT T.J. & LELE S.K., Boundary conditions for direct simulations of compressible viscous flows, *J. of Comp. Phys.*, 101, pp. 104-129, 1992.

[73] RAGAB S.A. & WU J.L., Linear instabilities in two-dimensional compressible mixing layers, *Phys. Fluids*, 1, pp. 957-966, 1989.

[74] RAGAB S.A. & SHEEN S., The nonlinear development of supersonic instability waves in a mixing layer, *Phys. Fluids A*, 4 (3), pp. 553-566, 1992.

[75] REYNOLDS O., An experimental investigation of the circumstances which determine whether the motion of water shall be direct and sinuous, and the law of resistance in parallel channels, *Phil. Trans. Roy. Soc.*, pp. 51-105, 1883.

[76] RODI W. & MANSOUR N.N., Low Reynolds number $k - \epsilon$ modeling with the aid of direct simulation data, *J. Fluid Mech.*, 250, pp. 509-529, 1993.

[77] ROGERS M.M. & MOSER R.D., Direct simulation of a self-similar turbulent mixing layer, *Phys. Fluids*, 6(2), pp. 903-923, 1994.

[78] SANDHAM N.D. & REYNOLDS W.C., A numerical investigation of the compressible mixing layer, *Report TF-45*, Stanford University, California, 1989.

[79] SANDHAM N.D. & REYNOLDS W.C., Three-dimensional simulations of large eddies in the compressible mixing layer, *J. Fluid Mech.*, 224, pp. 133-158, 1991.

[80] SANDHAM N. & KLEISER L., The late stages of transition to turbulence in channel flow, *J. Fluid Mech.,* 245, pp. 319-348, 1992.

[81] SARKAR S., ERLEBACHER G., HUSSAINI M. & KREISS H., The analysis and modeling of dilatational terms in compressible turbulence, *J. Fluid Mech.*, 227, pp. 473-493, 1991.

[82] SHAO L., SARKAR S. & PANTANO C., On the relationship between the mean flow and subgrid stresses in LES of turbulent shear flows, *Phys. Fluids*, 11(5), pp. 1129-1248, 1999.

[83] SMAGORINSKY J., General circulation experiments with the primitive equations, *Mon. Weather Rev.*, 91, pp. 99-164, 1963.

[84] SMITS A.S., Picture of the Week (internet) pages, Princeton University.

[85] SPEZIALE C.G., SARKAR S. & GATSKI T.B., Modeling the pressure-strain correlation of turbulence: An invariant dynamical systems approach, *J. Fluid Mech.*, 227, pp. 245-272, 1991.

[86] SPEZIALE C.G., Analytical methods for the development of Reynolds-stress closures in turbulence, *Ann. Rev. Fluid Mech.*, 23, pp. 107-157, 1991.

[87] SLESSOR M.D., BOND C.L. & DIMOTAKIS P.E., Turbulent shear-layer mixing at high Reynolds numbers: effects of inflow conditions, *J. Fluid Mech.*, 376, pp. 115-138, 1998.

[88] SONDERGAARD R., MANSOUR N.N. & CANTWELL B.J., The effect of initial conditions on the development of temporally evolving planar three dimensional incompressible wakes, *Application of Direct and Large Eddy Simulation to Transition and Turbulence*, AGARD Conference Proceedings 551, pp. 26.1-26.12, 1994.

[89] SPALART P.R., Direct simulation of a turbulent boundary layer up to $R_\theta = 1410$, *J. Fluid Mech.*, 187, pp. 61-98, 1988.

[90] STEWARTSON K., *The theory of laminar boundary layers in compressible fluids*, Oxford Mathematical Monographs, 1964.

[91] STREETT C.L. & MACARAEG M.G., Spectral multi-domain for large-scale fluid dynamic simulations, *Appl. Numer. Math.,* 6, pp. 123-139, 1989.

[92] STRENG M., BROEZE J., KUERTEN H. & GEURTS B., De (on)berekenbaarheid van turbulentie, *Nederlands tijdschrift voor Natuurkunde*, 62, pp. 23-26, 1996.

[93] TAVOULARIS S. & CORRSIN S., Experiments in nearly homogenous turbulent shear flow with a uniform mean temperature gradient. Part 1, *J. Fluid Mech.*, 104, pp. 311-347, 1981.

[94] TENNEKES H. & LUMLEY J.L., *A first course in turbulence*, The MIT Press, Cambridge, 1974.

[95] TOWNSEND A.A., *Structure of Turbulent Shear Flow*, Cambridge University Press, Cambridge, England, pp. 188-230, 1976.

[96] VAN DYKE M., *An album of fluid motion,* The Parabolic Press, Stanford, California, 1982.

[97] VREMAN A.W., GEURTS B.J. & KUERTEN J.G.M., Subgrid-modelling in LES of compressible flow, *Direct and Large-Eddy Simulation I,* Eds. P.R. Voke, L. Kleiser & J.P Chollet, pp. 133-144, 1994.

[98] VREMAN B., GEURTS B. & KUERTEN H., On the formulation of the dynamic mixed subgrid-scale model, *Phys. Fluids*, 6, pp. 4057-4059, 1994.

[99] VREMAN B., GEURTS B. & KUERTEN H., A priori test of Large Eddy Simulation of the compressible mixing layer, *J. Eng. Math.,* 29, pp. 299-327, 1995.

[100] VREMAN B., GEURTS B. & KUERTEN H., Subgrid-modelling in LES of compressible flow, *Applied Scientific Research*, 54, pp. 191-203, 1995.

[101] VREMAN A.W., Direct and Large-Eddy Simulation of the Compressible Turbulent Mixing Layer, *Ph.D. Dissertation*, University of Twente, The Netherlands, 1995.

[102] VREMAN A.W., GEURTS B.J. & KUERTEN J.G.M., Comparison of numerical schemes in Large Eddy Simulation of the temporal mixing layer, *Int. J. Num. Meth. Fluids,* 22, pp. 297-311, 1996.

[103] VREMAN A.W., SANDHAM N.D. & LUO K.H., Compressible mixing layer growth rate and turbulence characteristics, *J. Fluid Mech.*, 320, pp. 235-258, 1996.

[104] VREMAN A.W., GEURTS B.J. & KUERTEN J.G.M., Large-Eddy Simulation of the turbulent mixing layer, *J. Fluid Mech.*, 339, pp. 357-390, 1997.

[105] WASISTHO B., GEURTS B.J. & KUERTEN J.G.M., Simulation techniques for spatially evolving instabilities in compressible flow over a flat plate, *Computers and Fluids,* 26, pp. 713-739, 1997.

[106] WASISTHO B., DE BRUIN I.C.C., GEURTS B.J. & KUERTEN J.G.M., Direct numerical simulation of subsonic spatially developing shear flows, *Advances in Turbulence VII,* pp. 175-178, Kluwer Academic Publishers, 1998.

[107] WILCOX D.C., *Turbulence Modeling for CFD*, DCW Industries, California, 1994.

[108] WYGNANSKI I. & FIEDLER H., The two-dimensional mixing region, *J. Fluid Mech.*, 41, pp. 327-361, 1970.

[109] ZANG Y., STREET R.L. & KOSEFF J.R., A dynamic mixed subgrid-scale model and its application to turbulent recirculating flows, *Phys. Fluids A*, 5, pp. 3186-3196, 1993.

[110] ZEMAN O., Similarity in supersonic mixing layers, *AIAA J.,* 30(5), pp. 1277-1283, 1992.

Acknowledgements

Summary

The main focus of this thesis is the numerical simulation of the three-dimensional turbulent mixing layer. Direct numerical simulations (DNS) of the spatial mixing layer have been conducted to explore the stages towards a fully developed turbulent flow. In this way, a database of a subsonic turbulent mixing layer has been generated from which several physical properties can be extracted. Numerical robustness of the DNS is studied by performing simulations at different resolutions and at different sizes of the computational domain. The results originating from two different inflow conditions with perturbations from either linear stability theory (LST) or of a random nature, exhibited a similar growth rate in the turbulent regime and compare favorably with data from physical experiments. Helical pairing occurred in both cases. Several model assumptions of typical Reynolds-averaged Navier-Stokes (RaNS) approaches were confronted with statistical DNS predictions and turned out to be quite inaccurate. It appeared that even after relatively long time-averaging, higher order moments like the Reynolds stress tensor appeared to display only modest convergence.

Large-eddy simulations (LES) have been conducted in the same computational domain using several subgrid-models. The results have been compared with filtered DNS data. The dynamic eddy viscosity model was employed for the extension towards a realistic configuration, consisting of a large computational domain and a high Reynolds number. A larger growth rate as well as a higher degree of three-dimensionality was found when the domain was enlarged in the spanwise direction. The streamwise development of some Reynolds stress tensor components showed signs of self-similarity. This became particularly clear when the streamwise domain was enlarged as well. In addition, more small-scale features were observed when the latter case was repeated at a ten times higher Reynolds number.

In the standard formulation of dynamic subgrid-models, the dynamic coefficient fluctuates both in time and space. It appeared that the centerline value of the time-averaged coefficient remained approximately constant in the turbulent regime. This triggered the introduction of a subgrid-model which employs a time-averaged coefficient instead. Statistical results of this model agree with previous findings. The computational costs decrease since the new model does not need a frequent update of the coefficient. Because of the time-averaging, this model may no longer need the presence of a homogeneous direction in space, which makes it also suitable for many other flows.

Samenvatting

In dit proefschrift staat de numerieke simulatie van de driedimensionale turbulente menglaag centraal. Om de stadia naar volledig ontwikkelde turbulentie te bestuderen, zijn directe numerieke simulaties (DNS) van de 'ruimtelijke' menglaag uitgevoerd. Dit resulteerde in een database waaruit meerdere fysische eigenschappen van een subsone turbulente menglaag kunnen worden geëxtraheerd. De numerieke robuustheid van de DNS is vastgesteld door simulaties bij verschillende resoluties en met verschillende groottes van het rekendomein uit te voeren. De resultaten van verschillende instroomcondities met verstoringen uit lineaire stabiliteitstheorie (LST) of juist met een random karakter, resulteerden in dezelfde groeifactor in het turbulente gebied en komen goed overeen met experimentele resultaten. Spiraalvormige paring kwam in beide gevallen voor. Verscheidene modelaannames van typische Reynolds-gemiddelde Navier-Stokes benaderingen zijn met de statistische DNS-voorspellingen vergeleken en bleken erg onnauwkeurig. Zelfs na relatief lange tijdsmiddeling convergeerden hogere orde momenten, zoals de Reynolds spanningstensor, slechts langzaam.

Large-eddy simulaties zijn uitgevoerd in hetzelfde rekendomein met behulp van diverse subgridmodellen. De resultaten zijn vergeleken met gefilterde DNS-resultaten. Voor de uitbreiding naar een realistische configuratie, dat wil zeggen in een groter rekendomein en met een hoger Reynoldsgetal, is het dynamische eddy-viscositeits model gebruikt. De domeinvergroting in de dwarsrichting resulteerde zowel in een grotere groeifactor als in een hogere mate van driedimensionaliteit. De ontwikkeling van sommige componenten van de Reynolds spanningstensor in de stroomrichting vertoonde tekenen van gelijkvormigheid. Dit werd vooral duidelijk bij domeinvergroting in de stroomrichting. Bij herhaling van de simulatie met een tien keer zo groot Reynoldsgetal ontstonden bovendien meer kleinschalige structuren.

In de standaardformulering van dynamische subgridmodellen fluctueert de dynamische coëfficiënt als functie van tijd en plaats. Op de middellijn bleek de waarde van de tijdsgemiddelde coëfficiënt bij benadering constant te zijn in het turbulente gebied. Dit gaf aanleiding tot de introductie van een subgridmodel dat als alternatief een tijdsgemiddelde coëfficiënt gebruikt. Statistische resultaten van dit model komen overeen met eerdere bevindingen. De rekentijd neemt af, omdat de coëfficiënt in het nieuwe model minder vaak berekend wordt. Door de middeling over de tijd, kan dit model ook gebruikt worden als er een homogene ruimtelijke richting is, zodat het ook geschikt is voor veel andere stromingen.

Curriculum Vitae

The author of this thesis was born on the 3rd of April 1972 in Hengelo. She finished her secondary education at the 'Twickel College' Hengelo in 1990. That summer she left for Sweden as an exchange student and graduated at an 'artistic high school' in Västerås.

In September 1991 she started to study Applied Mathematics at the University of Twente. One year later she also began as a violin student at the Conservatory of Music in Enschede. During the final phase of the study in mathematics, a practical training of five months was performed at the Royal Institute of Technology in Stockholm, Sweden. Under supervision of Ass. Prof. G. Kreiss, the numerical simulation of dendritic solidification was examined. This research was carried out with a grant from the Swedish Institute in Stockholm. Back in the Netherlands she started her Master's project, under supervision of Prof. P.J. Zandbergen. This involved the numerical simulation of solitary waves using approximation series. She received her Master's degree in September 1996.

Meanwhile, she was offered a PhD position in the same research group. The research concerned numerical simulation of a spatial mixing layer and resulted in this thesis. Interesting features of the work have been presented at international conferences in the United States, France, Great Britain and Belgium. She enlarged her teaching skills by giving courses on numerics, physics and analysis. In the mean time she graduated from the conservatory and received her degree of 'performing musician'.

Since March 2001 she is working at the Wireless Multimedia Research unit of Ericsson Eurolab Netherlands B.V. in Enschede.